Università degli Studi di Padova

Dipartimento di Scienze Chimiche

Via Marzolo 1 - 35131 Padova

CORSO DI LAUREA MAGISTRALE IN CHIMICA

Tesi di Laurea Magistrale

Synthesis of polyoxometalates and conjugation with peptides for cancer cell targeting

Relatore: Prof. M. Carraro

Controrelatore: Prof. M. Ruzzi

LAUREANDO: MATTIA FRIGO

Summary

Acknowledgements

Many were the brilliant people I met during my various months of work for my thesis. Here I will mention a few, particularly worthy of note, individuals who I will never be able to thank enough.

First of all, I would like to express my gratitude to my supervisor, Prof. Carraro, for giving me the opportunity of taking part in his research work and becoming a part of his team. I would also like to express my gratitude for all the help he provided: for enlightening me about even the smallest doubts, always being there to assist me at any time, and for making sure I assimilated the most about every single new aspect of my project. Secondly, I would like to thank my co-examiner Prof. Ruzzi for his advice, and for letting me re-discover my project from a totally different perspective.

Another important mention goes to the whole "Nano and molecular catalysis" team, especially PhD Haihong for being a wonderful companion during the countless inorganic syntheses performed under the same fume hood, as well as Prof. Ruzza and his research team. Another special mention goes to Nicola for his major work on the peptides in this thesis, as well as all the help and company provided during the countless coupling reactions and characterizations. I would finally like to express my sincere thanks to Claudia for being my light in the dark world of peptides. Last but not least, I would also like to express my gratitude to all the technical and support staff, especially Ileana Menegazzo, Giulio Purgato, Renato Schiesari and Samuel Pressi who contributed through several explanations and clarifications at making my knowledge go beyond my own limits. A final thanks also goes to Monica Montopoli and her team for performing the cytotoxicity tests on the hybrids in this work.

Abstract

Polyoxometalates are a class of inorganic compounds characterized by the presence of metallic centers (M), like Mo, W and V, and of other eventual heteroatoms (X) which are surrounded by a specific number of oxygen atoms, and then packed together in a discrete structure. They are well known for their applications in catalysis and material science, and they have recently sparked the interest of the scientific community thanks to their promising biological applications as antibacterial, antiantiviral, antimicrobial, antineurodegenerative and anticancer agents. Their ability to interfere with cellular, bacterial, and viral redox processes and to interact with essential biological macromolecules also highlights their major drawback, which is the lack of selectivity. This thesis focuses on the synthesis of new organic-inorganic polyoxometalate hybrids for specifically targeting cancerous cells and reducing their toxicity toward normal cells. The first part of this work consists in the synthesis of well-known inorganic precursors, in particular bis-substituted tris(NH_2) Mn-Anderson-Evans polyoxomolybdates, as well as new compounds such as bis-substituted tris-pentaerythritol Lindqvist polyoxovanadates. The second part of this work is the coupling reactions between the inorganic polyoxometalates (in their activated form with N-hydroxysuccinimide) and biological molecules. A first coupling reaction was performed with an amino acid, L-phenylalanine, in order to optimize the synthetic procedure for the prepared peptides: bombesin and RGD derivatives (in particular Demobesin-1 and c(RGDfK)), whose receptors have proven to be overexpressed on cancerous cells. The introduction of spacers (-EEEEβAla- and -Ttds-) between the polyoxometalate and the bombesin derivative was also evaluated and studied in order to minimize undesired interactions/folding between the two domains and make the peptide more bioavailable. The final products were completely characterized through

FT-IR, ESI-MS(-), ^{1}H and ^{51}V NMR (for vanadium compounds), CD, UV-Vis and elemental analysis. Additionally, 2D ^{1}H NMR (COSY, TOCSY and ROESY) were applied to assess composition and secondary structure of the peptide derivatives.

Abbreviations

ACN	Acetonitrile
Ala (A)	Alanine
CD	Circular Dichroism
COSY	Correlation Spectroscopy
DB (Demobesin-1)	H-Phe-Gln-Trp-Ala-Val-Gly-His-Leu-NH-Et
DCC	N, N’-Dicyclohexylcarbodiimide
DIPEA	N, N’-Diisopropylethylamine
DMF	N, N’-Dimethylformamide
DMSO	Dimethyl sulfoxide
D-Phe (f)	D-phenylalanine
ESI-MS(-)	Electrospray ionization mass spectrometry
FT-IR	Fourier-transform infrared spectroscopy
Gln (Q)	Glutamine
Glu (E)	Glutamic Acid
Gly (G)	Glycine
His (H)	Histidine
Leu (L)	Leucine
NHS	N-Hydroxysuccinimide
NMR	Nuclear Magnetic resonance spectroscopy
POM	Polyoxometalate
ROESY	Rotating-frame overhauser spectroscopy
TBA	Tetrabutylammonium
TFE	2,2,2-Trifluoroethanol

TOCSY	Total correlated spectroscopy
TRIS	Tris (hydroxyl-methyl)aminoethane
Trp (W)	Tryptophan
Ttds	Trioxatridecan-succinamic acid
Val (V)	Valine

Introduction

1.1 General introduction

Polyoxometalates (POMs) are a very important class of inorganic compounds which date back to 1826 when the first derivatives were successfully produced[1]. The phosphomolybdate of formula $[PMo_{12}O_{40}]^{3-}$, in particular, was reported by Jöns Jacob Berzelius, a Swedish chemist who is considered one of the founders of modern chemistry.[2] In the early 1930s, Keggin solved the structure of the anion $[PW_{12}O_{40}]^{3-}$ [3] but the turning point came when spectroscopic techniques were used for characterization, and since then, countless structures have been synthesized and characterized. Today POMs constitute a wide class of polynuclear metal-oxygen clusters with potential applications in many fields ranging from catalysis [4], molecular electronics to drugs with potential antitumor, antiviral, antibacterial and anti-Alzheimer's diseases activity. [5] The unprecedented properties and the structural possibilities of these compounds have attracted the attention of a large number of chemists for decades. According to Katsoulis' compilation, in 1996 there were more than 700 communications (publications and patents) in the family of POMs.[6]

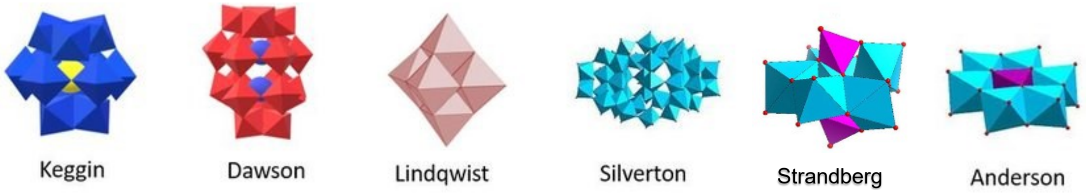

Figure 1. Sketches of classical polyoxometalates (POMs) structures in polyhedral illustrations.

They are characterized by various metallic centers, M, surrounded by oxygen atoms, although some derivatives with S[7], F[8], Br[9], and other p-block elements are known. The general formula of the base unit is MO_n, where n indicates the coordination number of M, and is usually equal to 6, even though it may also be 4, 5 or 7 as well. Over the past decades, various standardized methods have been developed with the aim of replacing the metal atoms by other metal atoms, modifying the structure, anion size, anion charge and many other features, considering also that polyoxometalates are capable of coordinating a great variety of hetero atoms, up to 75% of elements in the periodic table at well-defined geometric sites in the lattice. POMs can be therefore classified in two categories:

- Isopolyanions (IPAs) - $[M_mO_y]^{p-}$

- Heteropolyanions (HPAs) - $[X_zM_mO_y]^{q-}$

The X elements are also called primary, central or heteroatoms, and in general, any element can participate as X has no strict physical requirements for this position. Their presence results in an increased stability of the framework and often leads to a greater structural diversity as we will discuss in the next paragraphs.[10] On the other hand, M are the secondary, peripheral or addenda atoms and only some M elements are typically found in such compounds. Together with oxygen, they are the fundamental structural building blocks which compose POMs (MO_n and generally MO_6 units). The structures in which more than one M-type atom is present in the framework are called *mixed-addenda* clusters. The MO_6 octahedra units are, then, packed to form countless shapes and are joint via edge, corner and/or face- sharing, with a higher stability for structures in which the distance between the two M centers is maximized.[11]

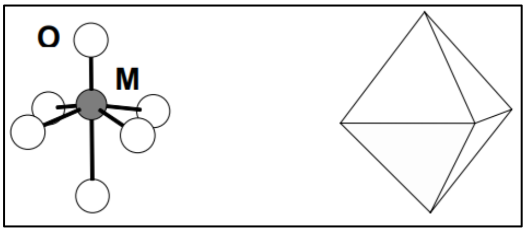

Figure 2. Ball-and-stick and polyhedral representations of the fundamental unit MO_6.

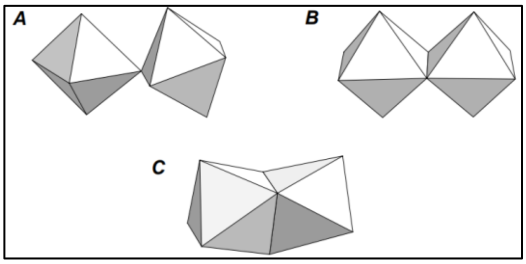

Figure 3. The polyhedral models represent the three possible unions between two MO_6 octahedral units: corner-sharing (A), edge-sharing (B) and face-sharing (C). Each corner represents an oxygen position.

Many M elements are known to form six-fold, octahedral coordination compounds with oxygen, but not so many can take part in a packed polynuclear metal-oxide aggregate. The two main reasons are the following:

- The structure of polyanions is governed by the electronic properties and ionic radius of metal centers, therefore only selected values of charge/radius ratio provide sufficient stability to the octahedral metal-oxide network to be successfully observed in POMs. These are mainly early transition metals but in fact there could theoretically be other ions, also from the p-block, which might be considered good candidates for the M position. However, this is not the only factor which matters!
- An additional parameter to consider is the ability of M to form metal-oxygen π bonds. It was observed that in octahedral MO_6 blocks, the metallic center is not in the very middle of the polyhedron, but somewhat displaced from the geometrical center towards one of the corners, more precisely the corner that does not share the atom with another octahedron, and the oxygen at this

position usually forms a double bond with the metal. This explains why POMs have discrete molecular arrays rather than an extended crystal lattice.

The main features of POMs are their redox properties. The metals in the M position are present in their highest oxidation state in all POMs typically in d^0 or d^1 electronic configuration and the bonds with O^{2-} ligands produce ionic structures. They can be compared to extended metal oxides but with the advantage of being soluble as discrete systems. The donation from the ligands to the metal center is low, so metals (depending on their physical nature) are willing to accept external electrons to fill up their valence shell. Reduced POMs might still be able to undergo further reductions since they can accept multiple electrons, this explains why they are often referred-to as "electron reservoirs".[12] Their tendency makes POMs are strong oxidizing agents, and the empty d-type orbitals can reversibly accept numerous electrons with no major change in their geometry. The electrons injected into the polyoxometalates on the reduction are usually delocalized over the MO_6 octahedra in the lattice and the degree of the delocalization depends strongly on the configuration of the M-O-M linkage, as well as the structural and chemical equivalency of the M sites.[13] M. T. Pope research focused on POM redox properties for decades, and he reported that anion charge has the largest influence upon redox potentials and an increase by one charge unit varies the redox potential by about 180 mV[14]. Finally, the isostructural molybdates have potentials that are approximately 400 mV more positive than the tungstate counterparts, and a similar trend is observed for the reduction of V.

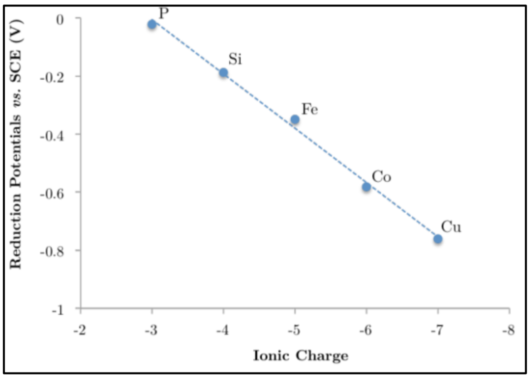

Figure 4. One-electron reduction potentials against the ionic charge, depending on the central heteroatom X.

As they are negatively charged, polyoxometalates may have different counter-cations, and therefore it is possible to tweak the solubility properties according to the chemical nature of the cations. In most of the cases they are isolated as alkali metal salts, being easier to crystallize. In case the cation is H^+, POMs are highly soluble in water, where they display super-acidity. In many cases, indeed, their pKa is close to 1, sometimes even lower than 0, implying that all their protons can be released in water. It is important to mention that not all the oxygen sites are identically basic or acidic because of the different position in the framework, the different kind of bonding, and the nature of M.[15] By changing the countercation with a quaternary salt such as N or P or a surfactant, it is also possible to make polyoxometalates soluble in an organic environment and become lipophilic.

1.2 Application of POMs

The field of polyoxometalates, despite being a mature field which has been studied for decades, continues to attract significant attention and the number of publications and patents continues to grow. [16] The two main fields for the study of POM are medical applications and catalysis. In the last century approximately 80% of patents and literature were focused on catalytic activity, but in the last decades the pharmaceutical field has grown in importance.

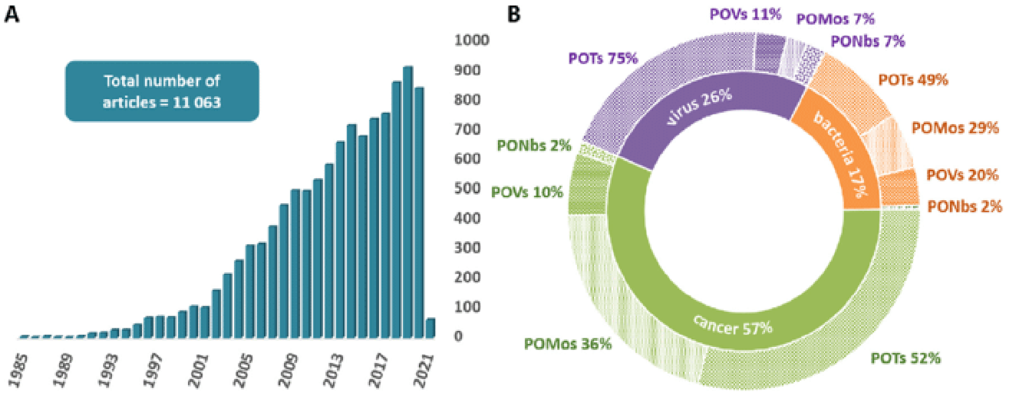

Figure 5. Graphs showing the total number of articles related to POMs by year and their role in pharmaceutical applications. Data on Nb, V, Mo, W POMs are herein collected.

Regarding the medical applications, other than anticancer, antibacterial, and antiviral activities, POMs were found to be insulin mimetic agents, inhibitors of several enzymes, as well as efficient against amyloid beta-peptides aggregation (known to be associated with Alzheimer's disease). Generally speaking, the research with POMs is primarily focused on cancer with 57% of the studies on this topic, followed by 26% on antiviral studies, and 17% on antibacterial research.[17] Over the years, indeed, POMs were reported to have beneficial properties against cancer[18,19] as well as against viruses such as herpes simplex virus (HSV), human immunodeficiency virus (HIV), influenza, and severe acute respiratory syndrome (SARS), and drug-resistant bacteria such as methicillin-resistant Staphylococcus aureus (MRSA) and vancomycin-resistant Staphylococcus aureus (VRSA).[20] Some recent studies have even demonstrated that POMs can prevent SARS CoV-2 from entering cells by blocking TMPRSS2, which SARS-CoV-2 uses for spike glycoprotein priming, and they may also engage with ACE2 and the spike glycoprotein to disrupt their binding by blocking the active sites.[21]

The catalytic applications of POMs are very broad, and are mainly due to their redox properties, which allow these compounds to be used as catalysts for oxidation of organic compounds. [22,23]

Other applications include the preparation of corrosion resistant coatings (owing to their electron acceptors behavior and low toxicity compared to other industrially used metals), additives in sol-gel inorganic matrices (to provide optical properties, adhesion, hardness and abrasion resistance)[24], nucleating agents for microelectronic integrated circuit-devices[25], dyes/pigments/inks (thanks to the stable precipitates with cationic dyes), and finally membrane sensors that exploit the high ionic conductivity of POMs. The most common uses of these membranes are in selective electrodes, in gas detection apparatuses, in solid-state electrochromic devices, and in liquid and solid electrolytic cells. There have also been minor studies for the usage of POMs as protein precipitation agents, plastic waste recycling agents, and analytical purposes for spectroscopic elemental determinations thanks to their ability to interact with other metal ions (Si, P, Al, Ge and many others).[16] A recent frontier is the use of transition metal substituted POM complexes (with Ru, Co and other transition metal ions) for applications in energy conversion, being suitable for the photo-sensitized water splitting with the final aim to produce clean H_2 fuel.

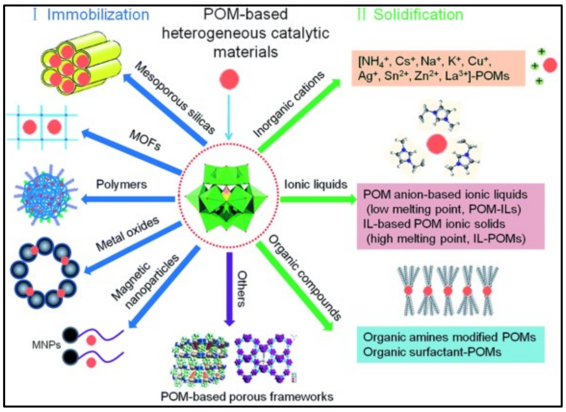

Figure 6. Recent advances in polyoxometalate-based heterogeneous catalytic materials for liquid-phase organic transformations.

1.3 POMs in this thesis: Mn-Anderson–Evans POM

Anderson-Evans polyoxoanions are composed of six edge-sharing $Mo^{VI}O_6$ or $W^{VI}O_6$ octahedra (in this thesis we will only consider the molybdenum ones) surrounding a central, edge sharing heteroatom with octahedral geometry XO_6, leading to a planar arrangement and a D_{3d} symmetry.[26] The oxygen atoms which are found in the structure display three different coordination models: six triple-bridged oxygen atoms (μ_3-O) connect two addenda atoms to the heteroatom X, six double-bridged oxygen atoms (μ_2-O) connect two addenda atoms, and two terminal oxygen atoms (O_t) are connected to each of the six addenda atoms. The formula of Anderson-Evans POMs can be written as $[H_y(XO_6)M_6O_{18}]^{n-}$ where y=O-6, n=2-8 and two structures can be found: the non-protonated A-type with central heteroatoms in high oxidation states with general formula $[X^{n+}M_6O_{24}]^{(12-n)-}$ and the protonated B-type with heteroatoms in lower oxidation states $[X^{n+}(OH)_6M_6O_{18}]^{(6-n)-}$. The average dimensions of the Anderson–Evans anion measures approximately 8.6 × 8.6 × 2.7 Å. All first-row transition metals except for Sc, Ti and V have been reported in literature to act as heteroatoms in the XMo_6 structure, and out of the heavier transition metals, only noble metals have been seen. Some post transition metals, and metalloids have also been encountered in the XMo_6 system, however there are many theoretically possible heteroatoms which are practically missing.

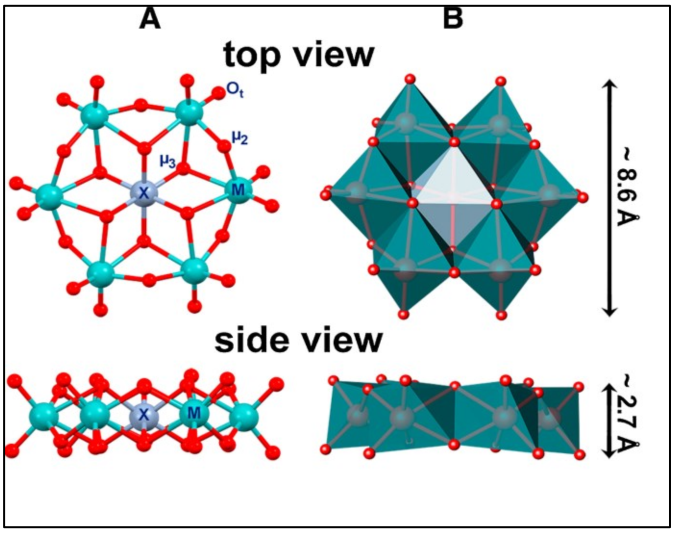

Figure 7. Ball-and-stick model of the Mn-Anderson Evans POM from different sides. It is possible to notice the different kinds of oxygen atoms attached to each metal center.

Type	***Chemical Formula***	***Metal M***	***Possible heteroatoms***
A	$[X^{n+}M_6O_{24}]^{(12-n)-}$	Mo^{VI}	I^{VII}, Te^{VI}
		W^{VI}	Ir^{IV}, Mn^{IV}, Sb^{V}, Te^{VI}
B	$\mathbf{[X^{n+}(OH)_6M_6O_{18}]^{(6-n)-}}$	$\mathbf{Mo^{VI}}$	Al^{III}, Co^{III}, Cr^{III}, Cu^{II}, Fe^{II}, Mn^{II}, $\mathbf{Mn^{III}}$, Ni^{II}, Rh^{III}, Zn^{II}

		W^{VI}	Mn^{II}, Ni^{II}

Table 1. Table showing the type of Anderson-Evans polyoxometalates, and their chemical composition. Note that the classification is not rigorous as there are cases of other metal centers such as Pt and Pd which can produce structures with various degrees of protonation, which make it difficult to classify them. In ***bold****: chemical composition of the polyoxometalate in this work.*

The Anderson-Evans structures exhibit physical and chemical properties which are highly versatile but depend strongly on the heteroatom, counter-cation, and functionalization. A property which is applicable to the majority of the compounds is the ligand-to-metal charge-transfer transition ($p_{\pi}(O_t) \rightarrow d_{\pi^*}Mo$) which shows intense UV absorption bands at approximately 210 nm with a shoulder at 240 nm and can be characterized by more bands depending on the presence of any further absorbing elements/units.[27] The Anderson-Evans POMs are also hydrolytically stable, enabling applications in biology[28], and different studies have also investigated their thermal stability and other properties such as magnetic behavior and luminescence, which depends on the above mentioned factors.[29,30]

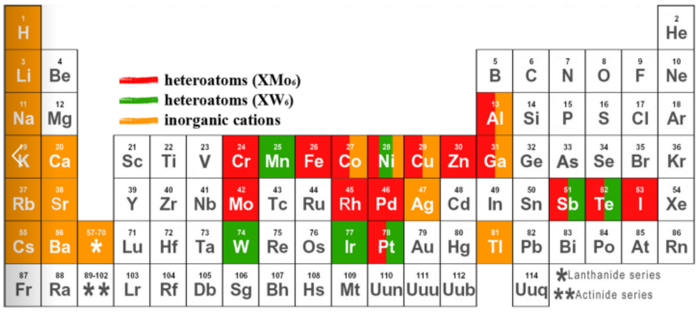

Figure 8. Periodic table showing the heteroatoms in the XMo_6 and XW_6 systems and the different cations successfully applied.

Once they have been synthesized, Mn-Anderson Evans polyoxometalates can undergo functionalization, which can follow two different directions[31]:

- "Extended" structures, involving organic molecules non-covalently attached to the POM which form a sort of hybrid network where the POM clusters act as building units to form a high-dimensional solid-state material.

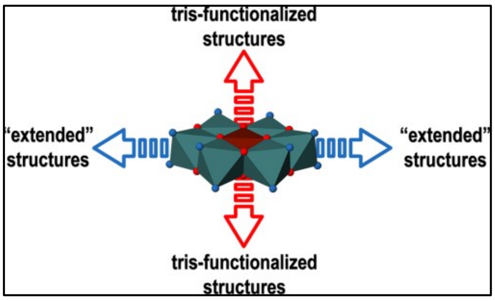

Figure 9. Illustration of where the majority of the reported "extended" and covalently attached hybrid structures connect to the Anderson–Evans POM framework.

- The six protons present in the B-type Anderson POM can be replaced with organic ligands, leading to the formation of hybrid organic–inorganic Anderson POMs. The organic ligands are usually tri-podal alcohols ($(HOCH_2)_3C$-R (R = -NH_2, -OH, -CH_2OH…, called "Tris" when R=NH_2) that can easily replace three protons on each side, forming double-sided symmetric hybrid organic–inorganic Anderson POMs. The tris-ligands can be synthesized first and then be grafted onto the POM (pre-functionalization) or tris-ligands can further be modified by organic reactions after attachment onto the POM (post-functionalization). The ligands can connect to two μ_3-O atoms and one μ_2-O atom (single or bis χ-isomer), or three μ_3-O atoms (δ-isomer). Due to the rather high symmetry of the inorganic Anderson–Evans POM and the presence of protonated μ_3-O atoms on both sides of the planar structure, functionalization with tris-ligands naturally results in double-sided products but single-sided isomers can be synthesized too. All known tris-functionalized systems are in the XMo_6 system with most of the reported structures containing either Mn^{III} or Cr^{III} heteroatoms.

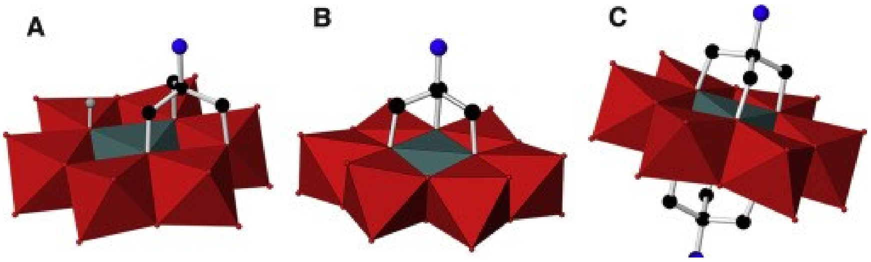

Figure 10. Ball-and-stick representation of single-sided χ-isomer (A), single-sided δ-isomer (B) and double-sided δ-isomer (C).

The general procedure for synthesis of tris functionalized POMs involves a one-pot reaction in which the tetrabutylammonium salt of the octamolybdate, a salt of the templating heteroatom, and the organic ligand are heated under reflux in organic solvent. The procedure to obtain the single-sided functionalization of the Anderson POM usually involves a two-step aqueous reaction, first the synthesis of the inorganic Anderson unit, followed by the attachment of the organic ligand by heating POM and the ligand together under reflux. A key factor for the single-sided functionalization appears to be the aqueous solvent, therefore a hydrothermal route can also be used to prepare these derivatives. [32]

1.4 POMs in this thesis: Lindqvist Vanadate

The hexametalate Lindqvist ion $\{M_6^{m+}O_{19}\}^{(6m-38)-}$ is composed by a super-octahedron of condensed $\{MO_6\}$ fragments and it is one of the classic structures in polyoxometalate chemistry.[33] It has been successfully synthesized for Mo, W, Nb, and Ta, and although the naked vanadium clusters are not known, the all-vanadium(V) form has been stabilized by capping with organometallic fragments.[34] It has been argued that the hypothetical $[V_6O_{19}]^{8-}$ polyoxoanion should be structurally unstable due to its high negative charge delocalized over the small molecule volume[35] , therefore $\{V_6O_{19}\}$ fragments exist only as part of polyoxovanadates of larger nuclearity such as $[V^V_{10}O_{28}]^{6-}$ which have been successfully isolated due to their lower molecular charge density. The only way to isolate the elusive $\{V_6O_{19}\}$ topology is, thus, by using the stabilizing effect of tris-alkoxo units which make the framework stable enough to exist both in solution and solid state, as the overall negative charge of the cluster is reduced. Depending on the overall working conditions and the vanadium precursor, a different number of μ_2-O ligands can be efficiently substituted by the terminal oxo groups of the tris-alkoxide [35], leading to bis-, tris-, and tetra-trisalkoxide functionalized hexavanadates $\{V_6O_{19-3x-y}\{(OCH_2)_3CR\}_x\}$ where x=2,3 and 4 have been isolated and characterized. It is exactly this form (in particular with x=2), which will be used as one of the precursors in this thesis. Monofunctionalized trisalkoxide Lindqvist-type hexametalates of the type $\{V_3Mo_3O_{16}\{(OCH_2)_3CR\}\}$ with R = $-Me$, $-CH_2OH$ and $-NH_2$ ligands have been recently prepared by using microwave assisted synthesis.[36]

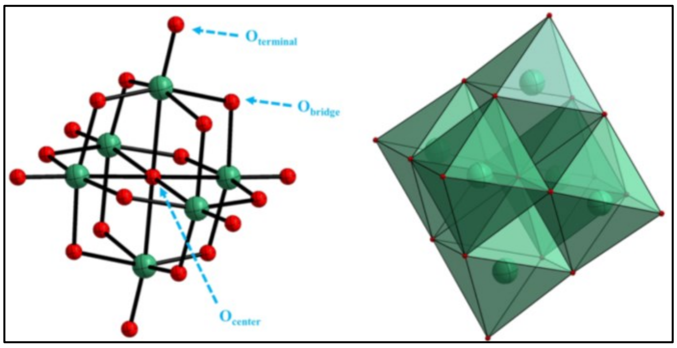

Figure 11. Ball-and-stick model (left) and the polyhedral model (right) of the Lindqvist-type hexavanadate. Green spheres are V atoms, whereas red spheres are O atoms.

The oxygens in these structures can be divided in three groups: the central oxygen, which is six-bridged (μ_6-O), 12 double-bridged oxygen atoms (μ_2-O), and 6 terminal oxygen atoms (t-O), one for each of the six addenda atoms.

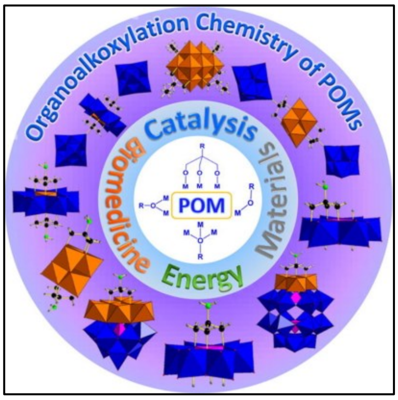

Figure 12. Scheme summarizing the most common applications of functionalized polyoxometalates

The usage of a tris reagent to introduce organic moieties to a polyoxometalate has been successfully tested also on Lindqvist-type vanadates and Dawson polyoxometalates.[37] Monofunctionalized trisalkoxide Lindqvist-type hexametalates of the type $\{V_3Mo_3O_{16}\{(OCH_2)_3CR\}\}$ with R = –Me, $–CH_2OH$ and $–NH_2$ ligands have also been prepared, but through a different synthetic route which involves microwaves.[35] A general drawback of the functional Lindqvist POVs is the low yield during their production, usually below 10 % based on vanadium. If the tris ligand has to be prepared in a multi-step synthesis and is then used in excess for the POV functionalization, the low yields have an even more negative impact.[38]

Once the polyoxometalate is functionalized with tris ligands, it is possible to use traditional organic chemistry reactions to post functionalize the metalate without any further modification to the metal–oxygen framework, even if only few organic post-functionalization reactions of tris-ligand functionalized Lindqvist-type vanadates were reported so far. Since their anionic nature limits both solubility and reactivity in organic media, the substituted Mn-Anderson-Evans and Lindqvist POMs are usually synthesized with large organic countercations such as tetraalkylammonium cations. On the other hand, their chemistry in aqueous media is hard-to-predict due to the coexistence of dynamic equilibria in solution which are influenced by pH and temperature.

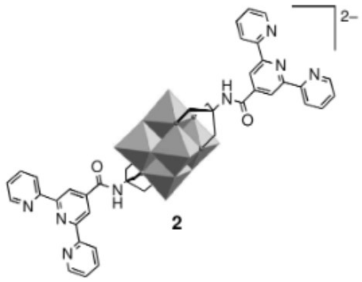

2

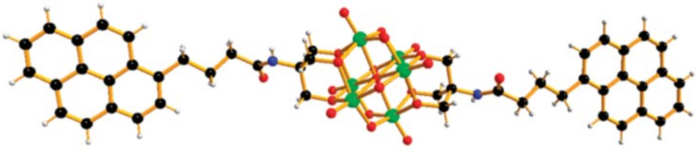

Figure 13. Two examples of Lindqvist-type vanadate hybrids which were successfully synthesized in 2011. The POM on the left is functionalized with terpyridine, and the one above is functionalized with pyrene.

2.0 What is cancer?

The POM synthesized in this thesis are intended to be used as drugs against several types of cancer. Before discussing their potential activity in this context, a short introduction on the origin of cancer is herein presented.

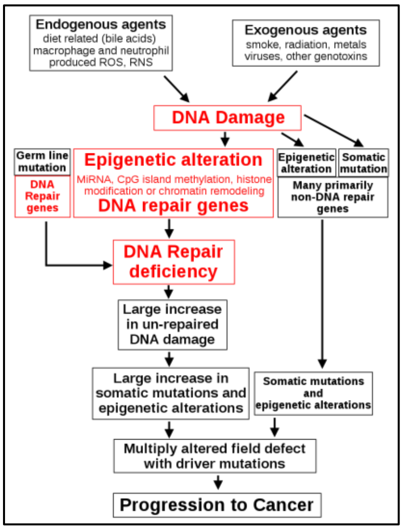

Figure 14. Scheme showing how cancer develops and progresses to more advanced phases.

Cancer is a disease in which the cells of the body divide and reproduce abnormally. These cells are capable of penetrating and destroying healthy body tissues.[39] In 2015, approximately 90.5 million people worldwide experienced cancer[40] and in 2019 annual cases of cancer grew up by 23.6 million people. Cancer is the second leading cause of death in the world and was responsible for an assessed 10 million deaths in 2019[41]. Globally, about 1 in 6 deaths is due to cancer. The most common types of cancer in males are lung cancer, prostate cancer, colorectal cancer, and stomach cancer. In females, the most common types are breast cancer, colorectal cancer, lung cancer, and cervical cancer.[42]

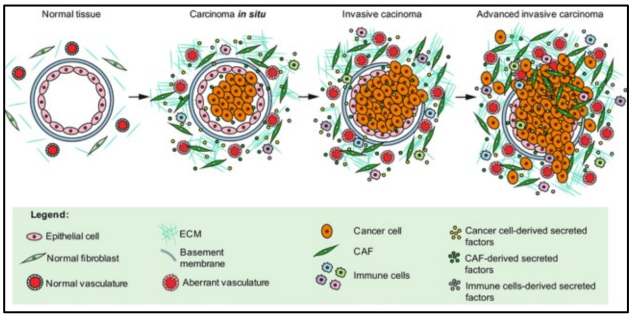

Figure 15. Visual depiction of a normal body tissue and the different phases of cancer development.

Cancer is fundamentally a disease of tissue growth regulation. For a normal cell to transform into a cancer cell, the genes that regulate cell growth and differentiation must be altered. Replication of the data contained within the DNA of living cells can probabilistically result in some errors (mutations). A complex error correction and prevention machinery safeguards the cell against cancer. If a significant error occurs, the damaged cell can self-destruct through programmed cell death, termed apoptosis. If the error control processes fail, then the mutations survives and is passed along to daughter cells.[43] Malignant transformation can occur through the

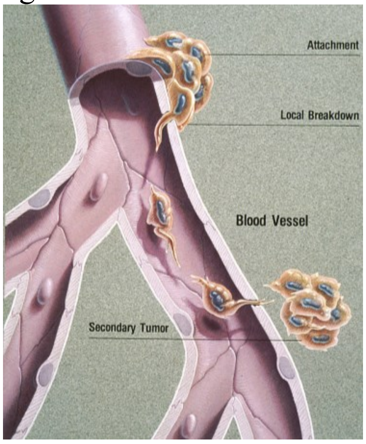

Figure 16. Image showing how metastasis of cancerous cells occurs through the blood flow.

formation of novel-features genes that promote cell growth and reproduction, inappropriate over-expression of normal growth and reproduction genes, or under-expression or disabling of tumor suppressor genes.[44] Cancer cells gradually lead to invasion (direct extension and penetration by cancer cells into neighboring tissues) and eventually to metastasis, which is the spread of cancer cells through the circulatory system or the lymphatic system to more distant locations.

2.1 Anti-cancer therapy – an overview

Chemotherapy is one of the most important methods of treatment and control of cancer. However, it is not always well received by patients due to its many side effects. Other therapies include radiation therapy, surgery, and the most innovative and promising targeted therapy. Chemotherapy can be used with both a curative intent and a palliative one and the principle is to use non-specific intracellular poisons to inhibit mitosis or induce DNA damage.[45] In this way, the cells are damaged or stressed, and the process leads to cell death if apoptosis is initiated. The overall effectiveness ranges from being curative for some cancers, such as some leukemias, to being ineffective, such as in some brain tumors[46], to being needless in others, like most non-melanoma skin cancers. Many of the side effects of chemotherapy can be traced to damage to normal cells (cytotoxicity) that divide rapidly and are thus sensitive to anti-mitotic drugs, especially cells in the bone marrow, digestive tract and hair follicles. The well-known cisplatin antitumor drug is used to treat a broad number of cancers (testicular cancer, ovarian cancer, cervical cancer, breast cancer, bladder cancer, head and neck cancer, esophageal cancer, lung cancer, mesothelioma, brain tumors and neuroblastoma) is known to have very severe side effects.

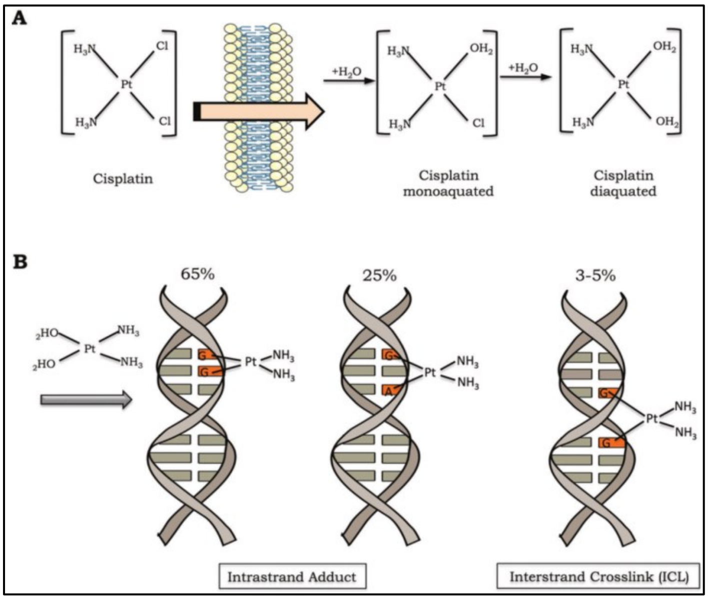

Figure 17. Activation process of cisplatin (A) and its antitumor mechanism, which can be explained by the formation of covalent bonds with DNA. (B) The major DNA lesions are intrastrand DNA adducts and interstrand crosslinks (ICLs).

Proteins and monoclonal antibodies (mAbs) are also used in cancer treatment; however, they are limited by poor delivery to tumors because of their large size and dose-limiting toxicity to the liver and bone marrow.[47] In addition, there are numerous adverse effects of mAbs that are related to their specific targets or mechanism of action. These target-specific adverse effects range from infections, autoimmune disease, contribution to tumor progression, and organ-specific adverse events such as cardiotoxicity.[48] They are also expensive, difficult to synthesize and modify.

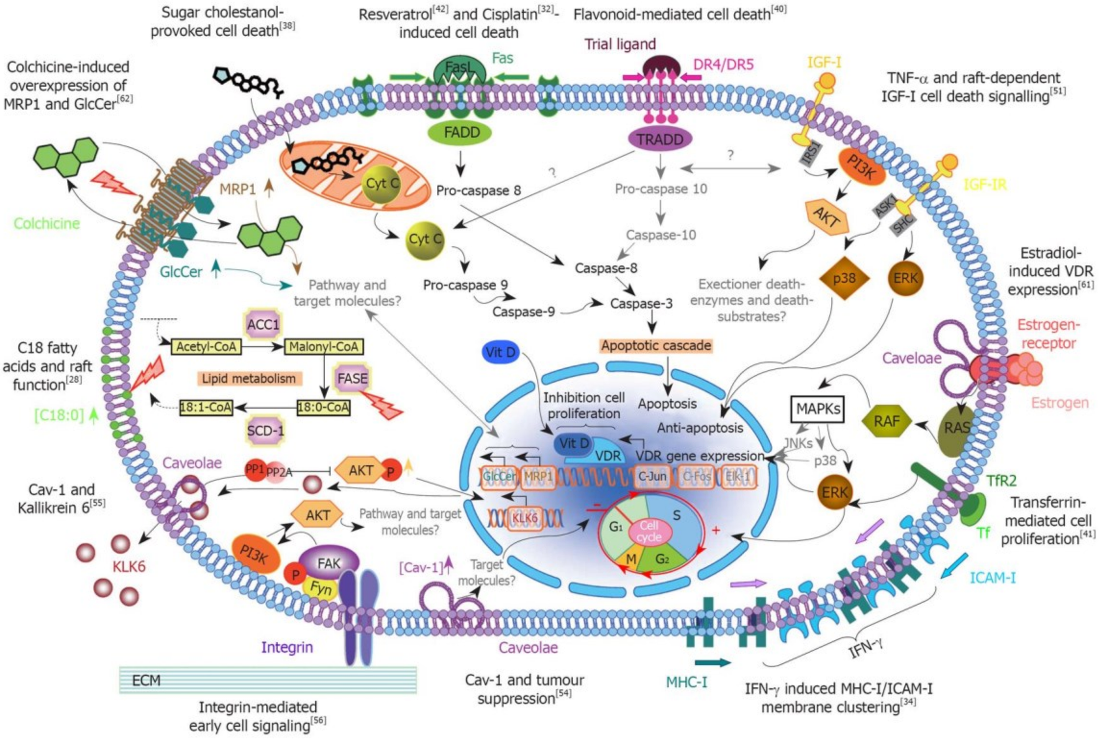

Figure 18. Scheme outlining the various membrane microdomain-mediated intracellular signaling pathways in colorectal cancer. The text and connector arrows as shown in black are confirmed observations, whereas the gray denotes postulated signaling pathways and/or unknown molecular targets. Scientists are constantly attempting to find targets contained only in cancer cells to provide a selective and efficient therapy without any side effects on heathy cells.

Two kinds of therapy seem more promising in the next future. The first is hormonal therapy, which involves the manipulation of the endocrine system through administration of specific hormones, particularly steroid hormones, or drugs which inhibit the production or activity of such hormones (hormone antagonists). Changing the levels or activity of certain

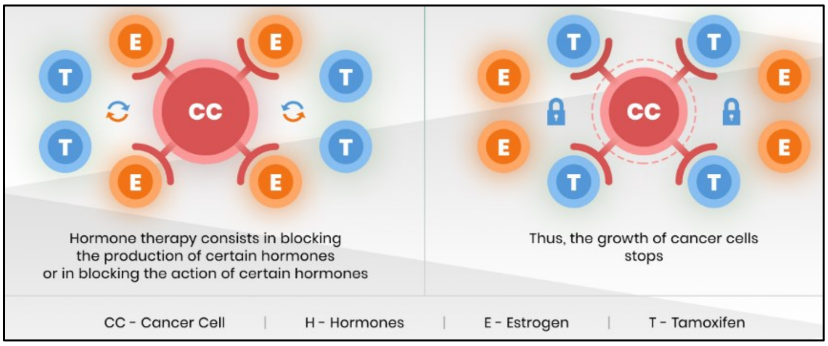

Hormone therapy consists in blocking the production of certain hormones or in blocking the action of certain hormones

Thus, the growth of cancer cells stops

CC - Cancer Cell | H - Hormones | E - Estrogen | T - Tamoxifen

Figure 19. Scheme which shows the mechanism of hormonal therapy.

hormones, indeed, can cause certain cancers to cease growing, or even undergo cell death. This route is not exempt from side effects which could potentially affect the whole body and healthy tissues/organs as well.[49]

The second option, which will be further studied and analyzed in this thesis, is targeted therapy, which blocks the growth of cancer cells by interfering with specific targeted molecules needed for carcinogenesis and tumor growth, rather than by simply interfering with all rapidly dividing cells. It is also called TDDS (targeted drug delivery system) and presents various advantages such as the reduction in the frequency of the dosages taken by the patient, having a more uniform effect of the drug, reduction of drug side-effects, and reduced fluctuation in circulating drug levels.

2.2 POM hybrids as targeted drug delivery systems for cancer therapy.

In the field of pharmaceutical science POMs have shown versatile biological activities and have sparked the interests in the scientific community[50] and many research teams have already produced some POMs with appealing anti-tumor capabilities.[51,52]

It has already been proven how POMs are able to penetrate cancer cells as they were found inside the cytoplasmic space. The exact mechanism is still unknown; however, it seems some kind of endocytosis is the most likely explanation.

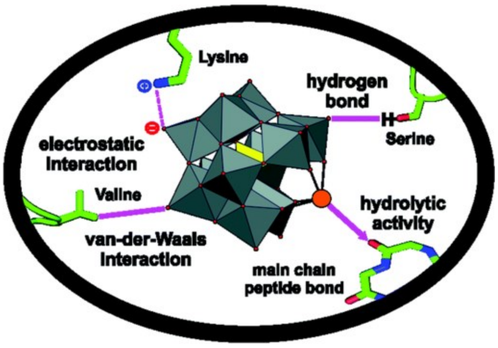

Figure 20. Example of common interactions of an inorganic POM with a protein.

The anticancer mechanism hasn't been fully understood yet[17], and various studies for different POM hybrids and mechanisms will be discussed in the next sections; however, the scientific community seems to agree that their curative properties have something to do with the redox potential, and the tendency of the central metal ion to accept electrons from the cellular environment. The higher the redox potential, the more cytotoxic the POM is, even if such a statement cannot be generalized since there are other factors which play an important role like composition, charge and structure of the POM. For example, an indicative order of structure type for inhibiting human epithelial carcinoma cells (KB cells) was as of 2004: $[NiV_{13}O_{38}]^{7-} > [Mo_7O_{24}]^{6-}$ > Anderson structure >> Keggin structure >> Dawson structure. Moreover, the nature of the metallic centers in the polyoxometalates also greatly influences their antitumor activity: the inhibition order for a KB cell is V > Mo

>> W. On the other hand, the nature of the counter cation and the heteroatom in the polyoxometalates exerted a relatively small influence on the inhibitory effect against the KB cell. This is clearly an indicative comparison but helps to prove why there has been an increasing interest especially for V and Mo POMs.[53]

Other mechanisms that have been proposed consider the interaction with positively charged proteins and enzymes, the competition with negatively charged substrates, the inhibition of the ATP production and angiogenesis, or the induction of apoptosis.[53]

Although POMs have appealing anti-tumor properties, the low biocompatibility and selectivity have hindered the development of POM-based medicines with practical applications. A possible solution to these drawbacks might the be upgrade to bio-conjugated systems in order to create a targeted drug delivery system (TDDS) composed of three components: a drug carrier, chemotherapeutic agents (in our case the POM) and a targeting ligand (small bioactive molecules, amino acids and peptides). The success of a TDDS depends on its selective binding to malignant cells, which relies on the binding affinity of the targeting ligand towards a specific target receptor. For a receptor to be considered as a target for drug delivery, it should be overexpressed on malignant rather than healthy cells, or even better, it should be specific only of malignant cells, and therefore not be present on normal healthy cells.[47] The discovery that tumor cells overexpress peptide-receptors on their surfaces has initiated a new era in the development of peptide analogues designed to target tumorous cells and during the last two decades, there has been a huge growth in the research of peptides for both diagnostic and therapeutic applications.[54]

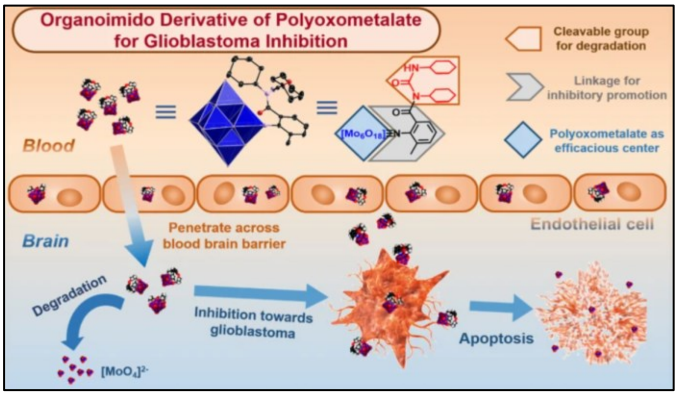

Figure 21. Schematic representation of the overall process of a POM hybrid (POM-AMB-acy) for glioblastoma inhibition. To prevent the side effects, this agent is endowed with degradability by introducing a cleavable functional group into its structure.

It is important to note that the low reaction yields and the high number of steps needed to synthesize POM hybrids make it very difficult for researchers to make progress in this field. As a matter of fact, only few examples of covalent bonding between POMs and amino acids or peptides were reported.[55]

2.2.1 Promising therapeutic effects of polyoxovanadate hybrids

Among the possible inorganic precursors, there has been an increasing interest for polyoxovanadates, which have already shown unique bioactivity like ATPases inhibitors, insulino-mimetics, anticancer and anti-inflammatory agents. Interests in the interaction of vanadate oxoanions with biological system increased since it has been demonstrated to have a variety of physiological effects acting either as a phosphate analogue in the monomeric form ($H_2VO_4^-$) [56], or as oligomeric vanadate species which interact with many biomolecules, triggering for example enzymes inhibition or activation. Data from the past two decades show spermicidal and anti-HIV activity of vanadium compounds[57] and the use of these compounds for treatment of diabetes[58] as well as the prevention of animal cancer.[59] Among the vanadate oligomers, decavanadate anion $[H_3V_{10}O_{28}]^{3-}$ has been referred of biochemical importance and it is considered the major protein-bound species with strong inhibitory effects on various enzymes, compared to other vanadate compounds[60]. Inhibitions of several adenosine triphosphatases (ATPases) such as P-type ATPases by V_{10} suggest that the interactions with these enzymes are favored by the existence of an ATP binding site. Na^+/K^+-ATPase (sodium pump) and plasma membrane Ca^{2+}-ATPase (PMCA) pump belong to the P-type ATPase family which use energy in the form of ATP to transport ions against their electrochemical gradient across the membrane. The former is a cell membrane located enzyme that establishes and maintains the high internal concentration of K^+ and low internal Na^+ concentrations, essential for normal cellular activities. The latter, PMCA, is a tuner of cytosolic calcium concentration in excitable cells, whereas it is the only system responsible for extrusion of Ca^{2+} outside non-excitable cells. The influence of V_{10} in the form of $(NH_4)_6V_{10}O_{28}\cdot 5H_2O$ on the two enzymes was very determining. The results showed that increasing concentrations of V_{10} induced inhibition of enzymatic activity in a concentration-dependent manner, with up to 80% of inhibition at a concentration of 1×10^{-5} mol/L[61] being potentially useful for various medical

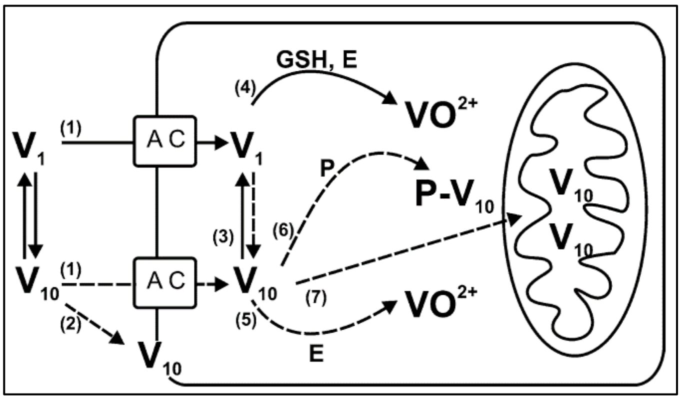

Figure 22. Proposed scheme of the cellular targets of decavanadate. The major targets are represented by the binding of V_{10} to target proteins to prevent their reduction (6) and accumulation in the mitochondria where they might interfere with the electron transport chain (7) and cause apoptosis.

conditions (cardiac diseases, thyroid issues...). In 2021 further studies about V_{10} verified its therapeutic effects on three invasive cancer cell lines: U87 (glioblastoma), IGR39 (melanoma) and MDA-MB-231(triple negative breast cancer). [62] In this case the inorganic compound was $Mg(H_2O)_6(C_4N_2H_7)_4V_{10}O_{28}\cdot 4H_2O$, which was proven to be stable in biological systems and toxic only in high quantities (>5 mg/kg). The half maximal inhibitory concentration (IC_{50}) for the glioblastoma and triple negative breast cancer cells was 2μM, and for the melanoma cells 3μM after a 72 h incubation period. The glioblastoma cells were proven to be more sensitive to the decavanadate compound than temozolomide, a widely used for conventional chemotherapy and for which glioblastoma cells often develop resistance. The results even suggested that the decavanadate anion is not responsible of the >5 mg/kg toxic effect on the kidney, but instead the cation is, therefore the introduction of organic cations into the POM framework can change its surface, charge, polarity, and redox properties, leading to a completely new compound with reduced toxicity and increased cell penetration ability.

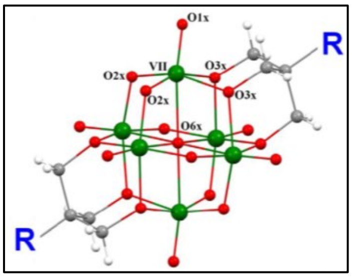

Figure 23. Labeling scheme and structure of the functionalized V_6 -POM.

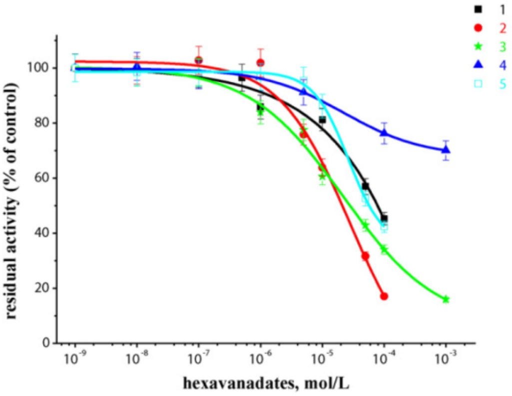

Figure 24. The influence of various concentrations of hexavanadates 1–5 on the activity of commercially available, purified porcine cerebral cortex Na^+/K^+-ATPase.

In 2016 some promising results about functionalized hexavanadates were published as well.[63] It was shown that various functionalized V_6 POMs such as $[V_6\text{-}CH_3][TBA]_2$ (1), $[V_6\text{-}NO_2][TBA]_2$ (2), $[V_6\text{-}OH][TBA]_2$ (3) and $[V_6\text{-}OH][Na]_2$ (4) inhibited Na^+/K^+-ATPase activity up to 30% at maximal investigated concentration 1×10^{-3} M. The inhibitory effect followed an order of 2>3>1>4 with the most powerful inhibitor being $[V_6\text{-}NO_2][TBA]_2$ however, its inhibition effect was 10 times less powerful compared to previous studies on the V_{10} compounds.[64] This might be due to the size of the inhibitor compared to the size of the enzyme pocket and the possibility establish different types of non-covalent interactions with amino acids of the enzyme. A qualitative observation of the electrostatic potential indicated that $[V_6\text{–}NO_2][TBA]_2$ and in a less extent $[V_6\text{–}OH][TBA]_2$ presents additional negative regions. The observations from the ab initio calculations that $[V_6\text{–}NO_2][TBA]_2$ had the most nucleophilic sites on the oxygen atoms shared between two vanadium atoms; and this could explain the good inhibitory effect. Further studies are needed.

The next step was clearly to optimize the biocompatibility and selectivity of these compounds by creating hybrids with amino acids or peptides. In 2019, a cooperation with various universities in China lead to a new synthetic route of V_6 hybrids.[50] The starting POM was the $[Bu_4N]_2[V_6O_{13}\{(OCH_2)_3CCH_2OOCCH_2CH_2COOH\}_2]$ which is the carboxyl-derivative of the Lindqvist-type hexavanadate. By amidation of this compound two new hexavanadate derivatives incorporating different amino acid esters, β-alanine ethyl ester and L-alanine methyl ester, were obtained. All the three compounds (precursor and two hybrids) showed inhibition activities against cell proliferation for Human laryngeal carcinoma epithelial (Hep-2), Rhabdomyoma (RD) and Breast adenocarcinoma (MCF-7) cell lines, and the two hybrids exhibited even better activities than 5-fluorouracil. The organic-substituted POMs were over 4 times more efficient than the fully inorganic precursor, with inhibitory activities >50% compared to V_6-POM and 5- fluorouracil. One year after, in 2020 a novel hexavanadate-based derivative covalently modified with glycine ethyl ester was synthesized and exhibited stronger inhibitory activity on human hepatocellular carcinoma tumor.[65] The inhibitory activity at 50 µM of the inorganic POM alone was only 48% compared to the 82% of the POM-glycine hybrid. Also, the 5-fluorouracil drug

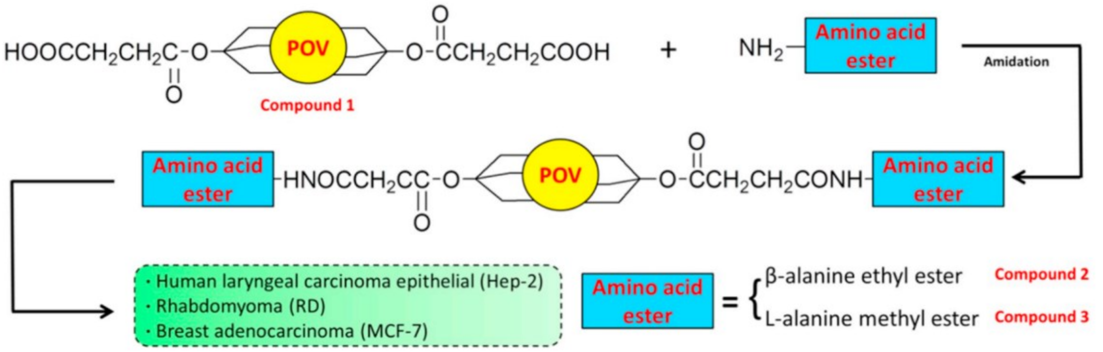

Figure 25. Synthetic pathway developed[50] to functionalize the V_6 POM with the two amino acids L-alanine and β-alanine in their methyl ester form.

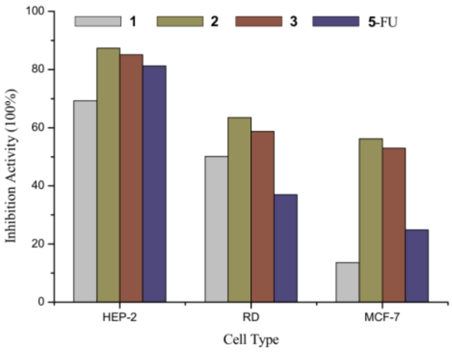

Figure 26. Inhibition activities against cell proliferation for the POM alone, the hybrid with β-alanine ethyl ester and L-alanine methyl ester and 5-fluorouracil, a commercial drug.

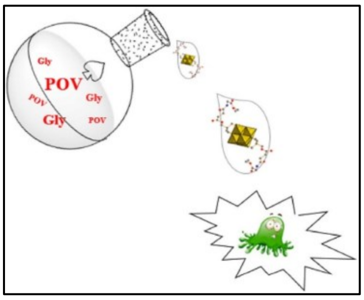

Figure 27. Simplified scheme about the usage of the V_6 hybrid for therapeutic purposes.

scored significantly worse than the hybrid and was able to inhibit only 50% of the hepatocellular carcinoma cells. These results confirmed once again the great potential of the organic functionalized hexavanadates derivatives as antitumor drugs and have illuminated the importance of further studies with other hybrids in this research field.

2.2.2 Promising therapeutic effects of polyoxomolybdate hybrids

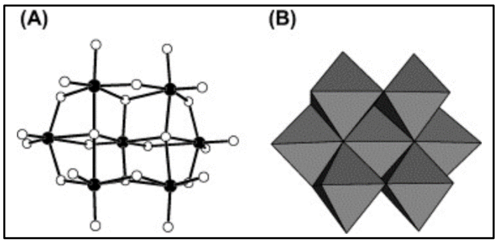

Figure 28. Structure of polyoxomolybdate; $[Mo_7O_{24}]^{6-}$. (A) The Mo atoms are represented as full black circles, and the white empty ones are oxygen atoms. (B) Octahedral model of polyoxomolybdate.

Polyoxomolybdates have also shown interesting effects. In 1988 $[NH_3Pr^i]_6[Mo_7O_{24}]$ was found to exhibit anti-tumor activity against human breast cancer, sarcoma and adenocarcinoma in vivo thanks to its oxidant power. [66] Further studies also confirmed the efficacy of the same polyoxomolybdate for the treatment of human pancreatic cancer, gastric cancer, colon cancer and lung cancer.[67] Toshiro Yamase, academic researcher from Tokyo Institute of Technology and one of the principal scientists in the field of POMs and their applications noticed that the $Mo^VO_5(OH)$ site in $[Mo_7O_{23}(OH)]^{6-}$ showed a significantly higher toxicity in comparison to the d^0 configured $Mo^{VI}O_6$ site in $[Mo_7O_{24}]^{6-}$ and his proposed mechanism was that the polyoxomolybdate would have been reduced in the tumor cells by flavin mononucleotide (FMN), an electron carrier responsible for the electron transport from NADH to coenzyme Q.[13,67]This process is coupled with ATP generation and therefore the proposed redox-cycle mechanism is based on the inhibition of ATP formation which leads to cellular death. More in detail, the $[Mo_7O_{24}]^{6-}$ interacts with flavin mononucleotide (FMN) to yield a 1:1 complex which makes the redox potential 0,1 V more positive than FMN. The antitumor activity can be explained by the repeated redox cycles of $[Mo_7O_{24}]^{6-}$ in tumor cells, which would inhibit the ATP generation coupled with the electron transfer from NADH to coenzyme Q in/on the mitochondria.

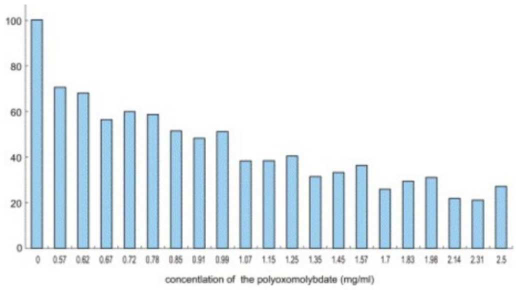

Figure 29. Effects of $[Mo_7O_{24}]^{6-}$ at a concentration of 0-2,5 mg/mL for 24 hours.

$[Mo_7O_{24}]^{6-} + e^- + H^+ \rightarrow [Mo_7O_{23}(OH)]^{6-}$

The newly generated reduced species synergically contributes to the process of apoptosis given its high toxicity which has been proved to be 10 times higher than the same oxidized species[68]. Due to the enhanced metabolism, polyoxomolybdate would preferentially be taken into tumor cells and the high molecular weight would result in a longer stay inside the cellular membrane. As a proof that the active species is Mo^{V}, it was attempted to photo-reduce $[NH_3Pr^{i}]_6[Mo_7O_{24}]\cdot 3H_2O$ to $[Me_3NH]_6[H_2Mo^{V}_{12}O_{28}(OH)_{12}(Mo^{VI}O_3)_4]\cdot 2H_2O$ and test its effects on cancerous cells in vitro and on mice through intratumoral injections, and the results found strong cytotoxicity and antitumor effects. Anderson structural polyoxometalates and V-shaped heptamolybdates have also been recognized to exhibit antitumor activities at non-cytotoxic doses in vivo.

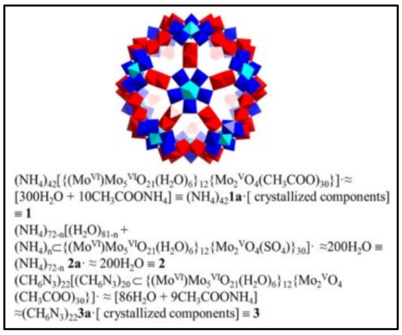

$(NH_4)_{42}[\{(Mo^{VI})Mo_5^{VI}O_{21}(H_2O)_6\}_{12}\{Mo_2^{V}O_4(CH_3COO)_{30}\}]\cdot\approx [300H_2O + 10CH_3COONH_4] \equiv (NH_4)_{42}\mathbf{1a}\cdot$[crystallized components] $\equiv \mathbf{1}$

$(NH_4)_{72\text{-}n}[(H_2O)_{81\text{-}n} + (NH_4)_n\subset\{(Mo^{VI})Mo_5^{VI}O_{21}(H_2O)_6\}_{12}\{Mo_2^{V}O_4(SO_4)\}_{30}]\cdot \approx 200H_2O \equiv (NH_4)_{72\text{-}n}\,\mathbf{2a}\cdot \approx 200H_2O \equiv \mathbf{2}$

$(CH_6N_3)_{22}[(CH_6N_3)_{20}\subset\{(Mo^{VI})Mo_5^{VI}O_{21}(H_2O)_6\}_{12}\{Mo_2^{V}O_4(CH_3COO)_{30}\}]\cdot \approx [86H_2O + 9CH_3COONH_4] \approx (CH_6N_3)_{22}\mathbf{3a}\cdot$[crystallized components] $\equiv \mathbf{3}$

Figure 30. Depiction of the structure and formula of the POM nanoparticles.

A Chinese research team has also investigated the application of POM nanoparticles with the aim of blocking angiogenesis, the formation of new vessels from pre-existing endothelium[69], and therefore stopping cancer from receiving nutrients. Mo POM nanoparticles have instantly provided good stability at physiological conditions, smaller size, fewer harmful effects, good water solubility, simple synthesis procedures. An example of formula is: $(CH_6N_3)_{22}[(CH_6N_3)_{20}\subset\{(Mo^{VI})Mo_5^{VI}O_{21}(H_2O)_6\}_{12}\{Mo_2^{V}O_4(CH_3COO)_{30}\}]\cdot\approx[86\ H_2O + CH_3COON\ H_4]$ The results showed an increase of reactive oxygen species (ROS) levels (a marker of mitochondrial dysfunction and apoptosis) and effects on mitochondrial membrane potential dissipation, which resulted in inhibited proliferation of cancerous cells.[70]

A first attempt to chemically modify a polyoxometalate by introducing a biologic ligand was the synthesis of a series of heteropolyoxomolybdate-bisphosphonate hybrids containing $Mo^{VI}O_6$ octahedra, zoledronate (the most potent commercially available bisphosphonate, used as a medication for various bone diseases linked to cancer), and in two cases, Mn as a heterometal in the form of $Mo_4Zol_2Mn(II)$. The hybrid was tested in vitro against a human non-small cell lung cancer cell line NCI-H460, MCF-7 breast cancer, and SK-ES-1 sarcoma cells. The compounds had IC_{50}

values of ~ 4–5 μM and were, six times more active than zoledronate itself (IC_{50} = 28 μM).[71]

Mn Anderson Evans polyoxometalates have also sparked particular interest for their suitability to be covalently modified with biological ligands. A first example was the successful attempt to bind cholic acid, dehydrocholic acid and adipic acid to the POM. The POM-cholic acid hybrid was used to treat the two cancer cell lines and exhibited substantially greater growth inhibition effect on both in comparison with POM-Tris (IC_{50} hybrid: 55.9 μM compared to 291.7 μM of POM-Tris). More importantly, the hybrid selectively inhibited the growth of cancerous cells with no effects on healthy cells, identifying the synergic effect of both the POM and activation of the receptor triggered upon binding to cholic acid moiety. [72] One more publication successfully performed the coupling reaction between the POM and tocopherol succinate The cytotoxicity studies on various cancer cell lines showed that the presence of tocopherol succinate could change and modulate the potency of the final hybrid, and like in the previous study, the results showed more cytotoxicity for the hybrid, compared to the inorganic POM, with no significant cytotoxicity on normal cells (The IC50 of the hybrid was 167.3 mg/mL compared to 321.7 mg/mL of the POM alone).[73]

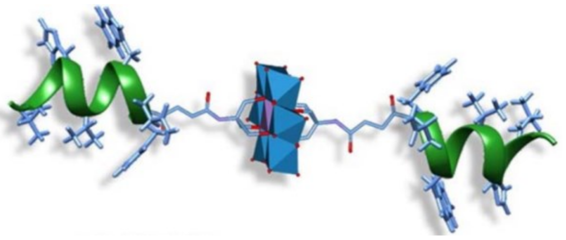

Figure 31. The hybrid[74] between the Anderson-Evans polyoxomolybdate and Demobesin-1.

In 2017, Anderson-Evans POM [$MnMo_6O_{18}$] was bis functionalized with a Bombesin antagonist peptide (Demobesin-1)[74]. The idea behind the functionalization with a bombesin peptide lies in the overexpressed receptor subtypes (BB_1 to BB_4) which characterize the gastrin releasing peptide receptor (GRP-R) in a large number of cancers including pancreas, prostate, gastrointestinal, breast, and small cell lung cancers. Bombesin shares the same C-terminal amino acid sequence of the gastrin-releasing peptide GRP (Trp-Ala-Val-Gly-His-Leu-Met-NH2), therefore shows binding affinity and specificity to the BB_2, BB_3, and

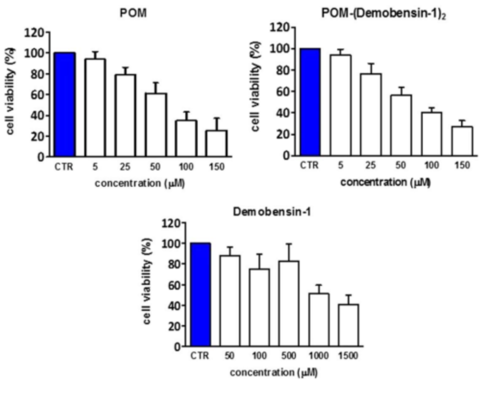

Figure 32. Results of the MTT test on HeLa cells (with a moderate GRP-receptor overexpression) after 48 h incubation. Demobesin-1 alone, POM alone, and the hybrid were tested.

BB$_4$ subtype receptors. To enhance the targeting effect, a study from 1999[75] suggested the usage of the antagonist peptide rather than the agonist, therefore the bombesin has gone through chemical modifications to obtain H-D-Phe-Gln-Trp-Ala-Val-Gly-His-Leu-NHEt. The final results of the study showed the inability of the peptide to target the receptor, possibly because of the influence of the POM on the conformation of the peptide. Regarding polyoxomolybdate POMs another recent study from 2020 seems to confirm the increasing interest and promising features of POM hybrids.[76] In this case biotin was used. Biotin in an essential coenzyme for five mitochondrial carboxylases and it has a critical role in the biotinylation of histones, which can affect cell proliferation, gene silencing, DNA repair pathways, and cell apoptosis.[77] It was already suggested that a Pt(IV)-biotin hybrid could provide enhanced cancer cellular uptake and reverse cis-platin resistance by improving the bioavailability of the drug conjugate, along with better selectivity.[78] Considering that cancer cells such as MCF-7 and HepG2 for their rapid cell growth have high levels of biotin receptors on the surface[79] it was attempted to create a hybrid between the polyoxomolybdate and biotin (Biotin-POM-Biotin Conjugate (BP57)). The cell survival percentage at a concentration of 400µg/mL was of only 20% for the hybrid, compared to over 60% of the pristine POM and it showed a lower normal-cell toxicity[76], therefore the synergistic effect of the inorganic part (POM) and organic (biotin) was confirmed.

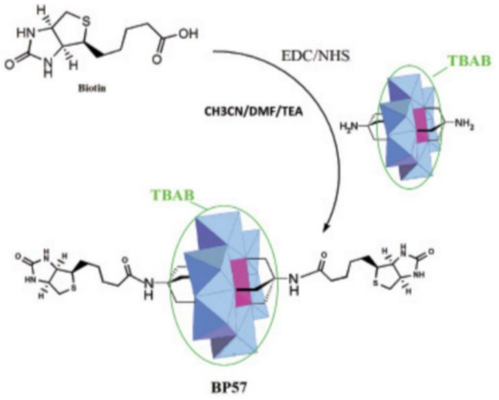

Figure 33: Biotin and Mn-Anderson Evans POM hybrid. TBAB is the countercation tetrabutylammonium bromide.

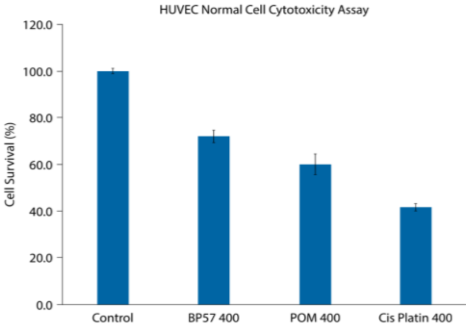

Figure 34. Comparison between the biocompatibility of the biotin hybrid, POM alone and cis-platin (the most known antitumor drug).

3.0 An overview on the most promising peptides.

In contrast to macromolecules, such as proteins, peptides have the advantage of being flexible messenger molecules with high affinity and specificity for their targets, are potentially active at nanomolar concentrations and are generally easy to synthesize with standard procedures. Small peptides also have biodistribution profiles characterized by high uptake in the target and rapid clearance from the blood, in contrast to macromolecules. In addition, peptides have increased capillary permeability, allowing more efficient penetration into target tissues than macromolecules. Naturally occurring peptides show high affinity for their receptors, which may be of different subtypes. The introduction of conformational constraints and/or unnatural amino acids, combined with molecular modelling and combinatorial screening to validate their effects, may be useful to further increase the affinity towards the specific subtype receptors expressed on tumor cells.[80] The ability to target a specific receptor subtype may be useful to avoid damaging healthy cells. However, considering the natural variability of the receptors, targeting more than one receptor subtype would greatly enhance the chance of actually stopping the tumor.[81] Another crucial consideration is about the in vivo stability of the peptides in plasma, considering the risk of degradation by endogenous peptidases and proteases. This limitation can be overcome with many approaches such as the synthesis of N- and C-terminally blocked peptides, cyclic peptides, and peptides containing unnatural or D-ammino acid residues. Between the peptide and the diagnostic/therapeutic part of the molecule a spacer can be introduced. The spacer may be a hydrocarbon chain, which increases the lipophilicity, or polyamino acid sequences, or even polyethylene glycol (PEG), which increases hydrophilicity. The linker also influences the excretion and clearance kinetics and consequently the background activity as well as toxicity.[82]

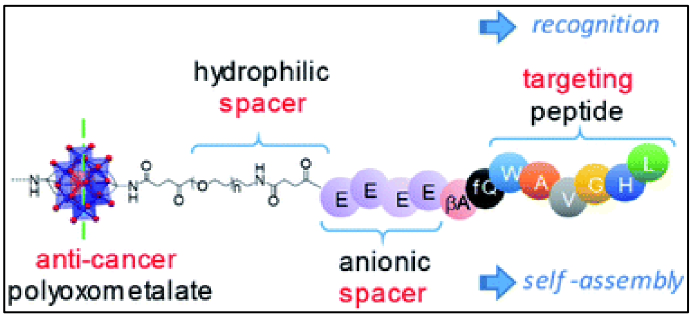

Figure 35. Example of structure of a POM hybrid with the inorganic polyoxometalate on the left, then the spacer, and finally the peptide.

In the previous chapters we mentioned some of the most recent research results; however, it is important to note that this is a vast topic since the peptide-receptors which are overexpressed in tumors are many and in constant discovery. Here are only few examples: somatostatin, cholecystokinin, neurotensin, neuropeptide Y, substance

Figure 36. Representation of the mechanism of an agonist compared to an antagonist in a generic receptor.

P, α-melanocyte-stimulating hormones, vasoactive intestinal peptides, bombesin and RGD. In this work, we will be focusing on the last two, which have only recently sparked interest. The usage of RGD or bombesin to prepare hybrid polyoxometalates is appealing for targeting only the tumor cells and may use the synergic chemotherapeutic properties of both the polyoxometalate and the receptor's peptide antagonist.

3.0.1 Bombesin

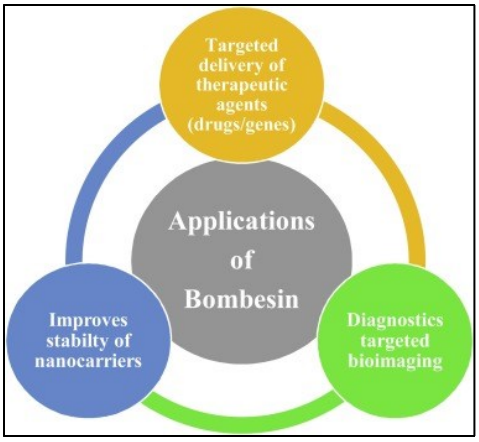

Figure 37. Scheme with all the possible uses of bombesin derivatives in medicine.

Bombesin is a 14-amino acid peptide with sequence Pyr-Gln-Arg-Leu-Gly-Asn-Gln-Trp-Ala-Val-Gly-His-Leu-Met-NH_2 and was initially isolated from the skin of two European aquatic toads of the family Bombinatoridae, Bombina bombina, and Bombina variegata, then two mammalian bombesin-like peptides were identified: gastrin-releasing peptide (GRP) and the neuromedin B. The former is a neuropeptide, a regulatory molecule that has been implicated in a number of physiological and pathophysiological process; most notably, it stimulates the release of gastrin from the G cells of the stomach, but it also plays a role play a role in human cancers of the lung, colon, stomach, pancreas, breast, and prostate.[83] The latter, neuromedin B, regulates body temperature, exocrine and endocrine secretions, cell growth, blood pressure and glucose level, and also sneezing.[84] Four different receptor subtypes have been characterized: the neuromedin B-preferring subtype (BB_1), the GRP-preferring subtype (BB_2), the bombesin receptor subtype 3 (BB_3), and the receptor subtype 4 (BB_4) which interacts with high affinity with both bombesin and GRP. The

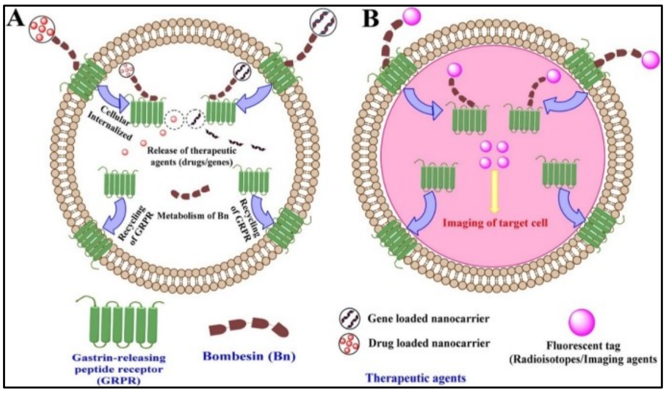

Figure 38. Bombesin receptor (GRPR) in cancer cells, which is the target for both delivering selective medications as well as diagnosis of tumors by functionalizing bombesin with fluorescently tagged radioisotope/imaging agents.

BB$_2$-subtype receptor is overexpressed in prostate, gastrointestinal, breast and small cell lung cancers. BB$_3$-subtype is frequently present in bronchial carcinomas, glucagonomas and vipomas (neuroendocrine pancreatic tumours), but is absent in both ileal carcinoids and insulinomas. BB$_1$ receptor is found in ilea carcinoids but is absent in other neuroendocrine tumors. BB$_4$ receptor is overexpressed in gastrinomas and some vipomas[85]. Bombesin and GRP have the same C-terminal amino acid sequence (Trp-Ala-L'al-Gly-His-Leu-Met-NH$_2$) therefore this peptide can be a good candidate to increase the selectivity of POMs.

Cancer type	Expression of BB2 or GRP receptors
Lung	75 - 100%
Prostate	60 – 100%
Pancreatic	75%
Breast	40-70 %
Neuroblastoma	2%

Table 2. Overexpression of GRP/BB2 receptors in percentage for various kinds of cancer.

Bombesin peptide derivatives and their mRNAs are found in many tumors and act as autocrine growth factors that stimulate tumor growth through specific receptors. These peptides have also been implicated in neo-angiogenesis in several cancer models. This suggests that the corresponding receptor is systematically expressed in tumor cells as well as in tumor vascular beds and plays an important biological function.[86]

In the past few decades, peptide receptor agonists were the ligands of choice for tracer development, utilization in nuclear medicine, and therapeutics primarily due to receptor-ligand complex internalization and the high accumulation of radioactivity inside the target cells. In contrast, antagonists, which do not trigger internalization, weren't considered for tumor targeting for years.[87] Some recent studies suggested that peptide antagonists showed preferable biodistribution, including considerably higher in vivo tumor uptake, compared with highly potent agonists, and even more promising were the results from the antagonist bombesin derivative Demobesin-1[88]: H-phe-Gln-Try-Ala-Val-Gly-His-Leu-NH-Et whish showed rapid blood clearance and excretion through the kidneys, whereas it was efficiently accumulated in the target organs with a high a prolonged localization at the tumor sites.[89] The tumor-to-kidney ratio for Demobesin-1 was more than 7-fold higher

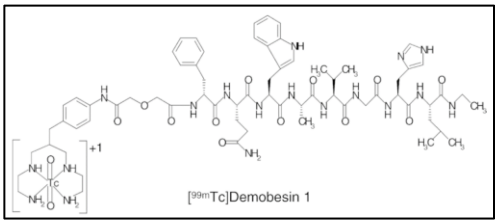

Figure 39. Demobesin-1 derivate with [Tc-99m] used for GRP receptor-targeted tumor imaging.

than the ratio for the corresponding agonist Demobesin-4, furthermore, it has been hypothesized that side effects observed during a clinical phase I dose escalation study of bombesin agonist, including abdominal cramps, nausea and diarrhea, might be avoided by using antagonists. In addition, antagonistic GRPR-based peptides may not induce the endocrinological side effects, including the stimulation of tumor-growth, that are known to occur with agonists.

Unfortunately, its hydrophilic nature makes it unable to cross the blood-brain barrier (less than 0.1% of total injected peptide), thus, the properties of bombesin are beneficial only when peripheral tumors are the desired targets.

3.0.2 Arginylglycylaspartic acid (RGD)

Another promising peptide is arginylglycylaspartic acid (Arg-Gly-Asp, RGD), which is the most common peptide motif responsible for cell adhesion to the extracellular matrix. Cell adhesion proteins called integrins recognize and bind to this sequence, which is found within many matrix proteins, including fibronectin, fibrinogen, vitronectin, osteopontin, and several other adhesive extracellular matrix proteins.[90]

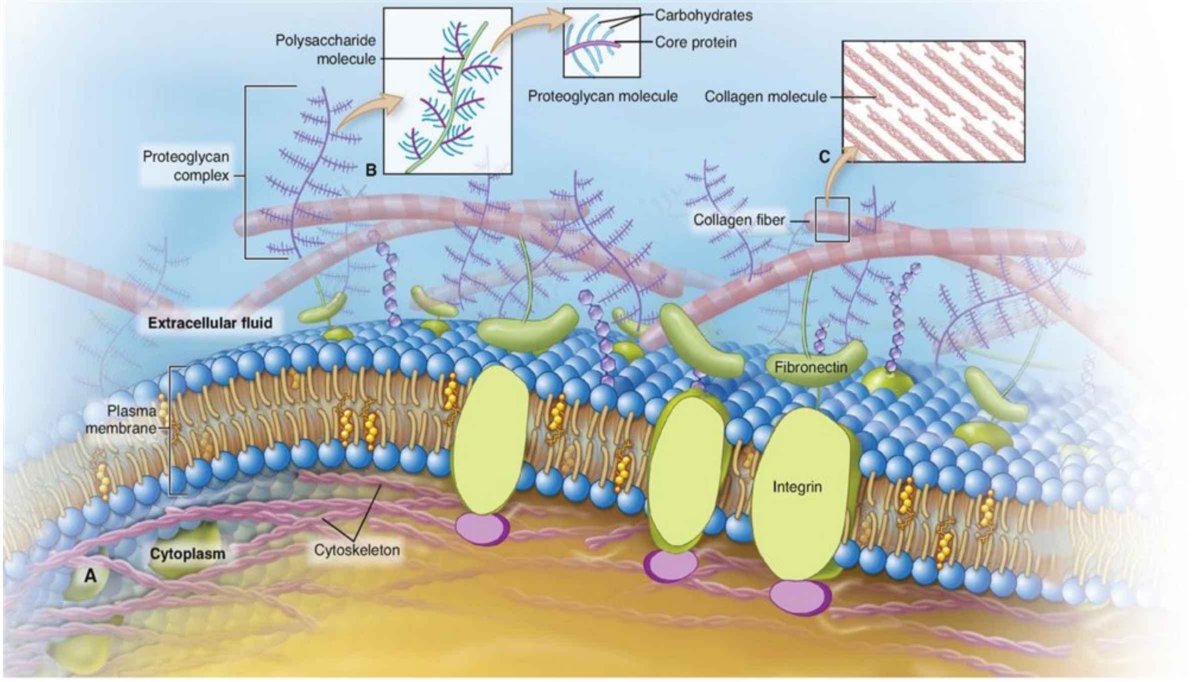

Figure 40. Schematic representation of the extracellular matrix proteins, which are responsible for cell adhesion and are an innovative antitumor target. The cell membrane proteins "integrins" recognize and bind to the RGD motif contained in fibronectin.

The binding of integrins to their ligands is dependent on divalent cations to mediate cell-cell and cell-matrix adhesion. Thus, integrins constituted cell adhesion receptors not only for cell-matrix adhesion but also for bidirectional signaling across the membrane[91], and are involved in fundamental cellular processes such as attachment migration, proliferation, differentiation, and survival. Integrins also contribute to the initiation and progression of many biological diseases such as angiogenesis, thrombosis, inflammation, osteoporosis neoplasia, tumor metastasis and gene expression.

RGD based peptides have been used to target various integrins, one of which, αvβ3, is preferentially expressed on proliferating endothelial cells, as well as on the cell membrane of various tumors including osteosarcomas, neuroblastomas, glioblastomas, melanomas, lung carcinomas, and breast cancer, and consequently it is considered a useful marker of both tumor-induced angiogenesis and cancer. It is also correlated to the invasive and metastatic potential of malignant tumors both in experimental models and in patient studies. Integrin αvβ3 interacts with RDG through the Asp218 at the entry of a shallow groove and located on the side, while Asp150 is present on the opposite side of this pocket. Asp150 offers an extra H-bond interaction opportunity. Both Asp residues provide a particularly strong interaction by interacting with the arginine. The Thr212 occupies the bottom of the groove. The sequence and the structure of RGD-containing peptides may have both linear and cyclic structure. The cyclic peptide (Arg-Gly-Asp-D-Phe-Lys) was found to be a better inhibitor of cell adhesion than the linear parent peptide, probably due to the conformationally less flexible structure to resist proteolysis and the ability to bind with higher affinities to integrin receptors. A methylated cyclic RGD-peptide acting as antagonist was also found efficient in blocking angiogenesis, microcirculation, growth and metastasis formation of a solid tumor in vivo, even in low doses.[91] Some tachyplesin functionalized RGDs were also capable of triggering apoptosis in TSU prostate cancer cells and B16 melanoma cells, and a Cyclic RGD peptide targeted monoclonal antibody (which could be replaced by a smaller polyoxometalate or other inorganic compound) was successfully able to inhibit αv

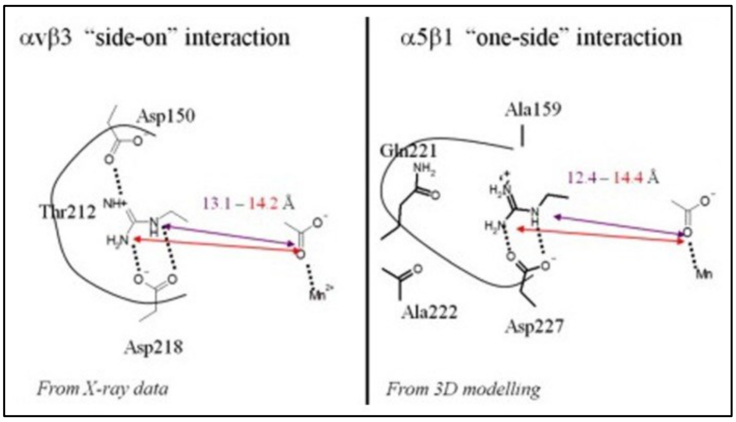

Figure 41. Mechanism of RGD interacting with integrins αvβ3 and α5β, both heterodimeric glycoprotein receptors. The one overexpressed on various tumors is the one on the left, αvβ3.

integrin–mediated cellular adhesion and induce detachment of previously substrate-attached tumor cells.

The usage of RGD in medicine presents several advantages, some of which are in common with other peptides that are being studies:

- RGD is much smaller as compared to monoclonal antibodies, and RGD conjugates can have easier access to the tumor tissue;
- The use of RGD minimizes the risk of immune reactivity or pathogen transfer;
- The synthesis of RGD peptides is relatively simple and inexpensive, which facilitates translation into the clinic;
- The applications of RGD are much wider than many other peptides. Not only is RGD used in tumor therapy, but it can also be coupled to material surfaces in controlled densities and orientations, which have promising applications in the field of tissue engineering to repair, maintain and improve biological tissues.[92]

Aim of this Thesis

The purpose of this thesis is to actively contribute to the research and development of new polyoxometalate hybrids with antitumor properties and high selectivity. More in detail, I will continue with the studies on the functionalization of the Mn-Anderson Evans polyoxomolybdates and Lindqvist polyoxovanadates carried out at the Department of Chemical Sciences of the University of Padua with a particular focus on Demobesin-1 and c(RGDfK) as peptides which will be used to functionalize the POM in order to target only cancerous cells where the corresponding peptide-receptors are overexpressed. The bombesin derivative used for the coupling reactions will also be pre-functionalized with different spacers, to gain information about the impact of the hydrophilic and anionic spacers on the interactions between the peptide and different POM surfaces. The molybdates and the vanadates, indeed, display different geometry and different charges, so they will be used as models to study peptide conformation/folding and assess in which case the latter become more accessible for intermolecular interactions. In particular, the project will require the synthesis of the polyoxomolybdate, followed by its reaction with (i) tris(hydroxymethyl)aminomethane (Tris), (ii) succinic anhydride and (iii) with N-hydroxysuccinamide to obtain a reactive POM, ready for peptide conjugation.

The same functionalization will be also attempted on the Lindqvist polyoxovanadates; however, this polyoxometalate will first be functionalized on both sides with pentaerythritol (ending with -CH_2OH-) instead of the previous -NH_2. Such reaction, indeed, seems more promising than the reaction with Tris but still requires some optimization. In both cases the active forms of POMs were reacted with all peptides available (DB and RGD derivatives) and studied by several techniques as ESI-MS, FT-IR, UV-vis, circular dichroism, 2D ^{1}H NMR.

Experimental Section

INSTRUMENTS USED

Circular Dichroism:

CD measurements were performed on Jasco J-1500 instrument. The measure range used was 260-190 nm in a 0.5 cm quartz cuvette, with 0.2 nm data pitch and 16 accumulations at 50 nm/min scanning speed. The solutions used were 50, 25, 12.5 μM at 25 °C. Analysis of CD spectra was carried out using Spectra Manager software supplied by Jasco. The secondary structure simulations were performed through the software CDApps with the CONTINLL algorithm and SP43 database (190–240 nm, estimating alpha-Helix type 1 and alpha-Helix type 2, beta-Strand type 1 and beta-Strand type 2 (S2), turns, unordered structures.

UV-vis measurements:

UV-vis measurements were carried out using two instruments: simultaneously on the CD Jasco J-1500 instrument, using the same parameters as the CD analysis, and the Varian Cary® 50 – Agilent with a 1 cm path quartz cuvette. The data of the latter instrument were processed by the Cary WinUV Application Software.

NMR Spectroscopy:

2D ^{1}H NMR data were recorded on a Bruker Avance DMX 600 and 400 MHz. Bruker 300 MHz UltraShield was used for monodimensional ^{1}H NMR and ^{51}V NMR (78.9 MHz). Deuterated DMSO and acetonitrile were used as solvents for analyes. Analysis of NMR spectra was performed on MestReNova and TopSpin software.

Electrospray Ionization Mass Spectroscopy:

MS measurements were carried out using a LC/MSD Trap SL instrument, equipped with an electrospray (ESI) source, supplied by Agilent Technologies. The samples, dissolved in acetonitrile, were injected by a HPLC pump, and analyzed in negative mode. Analysis of MS spectra was carried out using Data Analysis software supplied by Bruker.

Infrared Spectroscopy:

IR measurements were performed on a Jasco FT/IR-4100 spectrometer, by preparing KBr pellets. Analysis of IR spectra was performed on Jasco Spectra Manager 2.00.07.

MATERIALS

If not specified, all reagents and solvents were obtained from commercial sources and were used without further purification. For all the syntheses and solution, only MilliQ water has been used.

SYNTHESIS 1A:

Synthesis of “TBA-Mo_8O_{26}” - $[(C_4H_9)_4N]_4[Mo_8O_{26}]$

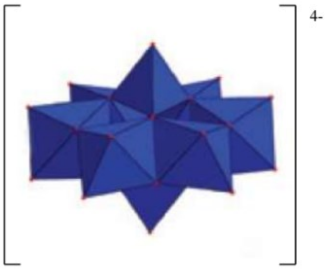

Reaction:

$12HCl + MoNa_2O_4 \cdot 2H_2O + 4C_{16}H_{36}BrN \rightarrow [(C_4H_9)_4N]_4[Mo_8O_{26}] + 12NaCl + 4NaBr + 6H_2O$

Procedure:

$MoNa_2O_4 \cdot 2H_2O$ (4.20g, 0.017mol) was dissolved in 10 mL of H_2O in a flask, and TBA-Br (2.8515g, $8.85x10^{-3}$ mol) was dissolved in 8 mL of H_2O in a beaker. 6.8 mL of HCl 3.8375M were added to the colorless solution of $MoNa_2O_4 \cdot 2H_2O$ under stirring, and then the solution of TBA-Br was added dropwise to the mixture under vigorous stirring with the immediate production of a white precipitate. The solid was filtered on a fitted funnel under vacuum and then washed with 30 mL of water, 20 mL of ethanol and 20 mL of diethyl ether. After 10 minutes the white precipitate was transferred in a round-bottom flask, dried under vacuum at first at the rotatory evaporator and finally with high vacuum pump. A white powder solid was obtained (MM = 2153.35 g/mol, 4.6782 g, 90% yield).

Analysis & Characterization:

FTIR (KBr, cm^{-1}): 3443 (w, br), 2963 (s), 2938 (s), 2873 (s), 1634 (w), 1483 (s), 1462 (m), 1381 (m), 1348 (w), 1153 (w), 951 (m), 924 (s), 909 (s), 853 (m), 806 (s), 663 (s), 599 (m), 501 (w).

ESI-MS (-) CH_3CN: 1913.7 ($[M-TBA]^-$), 1665.5 ($[M-2TBA+H]^-$), 833.8 ($[M-2TBA]^{2-}$).

SYNTHESIS 2A:

Synthesis of “Mn-Anderson TRIS” - $[(C_4H_9)_4N]_3[MnMo_6O_{18}\{(OCH_2)_3CNH_2)_2]$

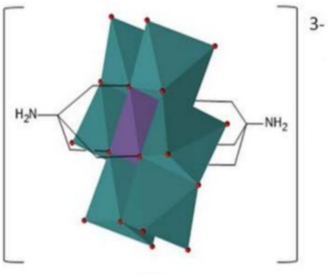

Reaction:

$$3\ [(C_4H_9)_4N]_4[\alpha\text{-}Mo_8O_{26}] + 4Mn(O_2CCH_3)_3 + 8(HOCH_2)_3CNH_2 \xrightarrow[ACN,\ 80°C,\ 22\ hours]{} [(C_4H_9)_4N]_3[MnMo_6O_{18}\{(OCH_2)_3CNH_2)_2] + 12CH_3COOH + 6H_2O$$

Procedure:

$[(C_4H_9)_4N]_4[\alpha\text{-}Mo_8O_{26}]$ (3.02g, $1.40\text{x}10^{-3}$ mol), $Mn(O_2CCH_3)_3$ (0.56893g, $2.12\text{x}10^{-3}$ mol) and $(HOCH_2)_3CNH_2$ (0.62702g, $5.22\text{x}10^{-3}$ mol) were dissolved in 75 mL of acetonitrile in a round-bottom flask and heated at 80°C for 22 hours with a reflux condenser attached to it. The day after the brown solution was cooled at room temperature and filtered twice until a red-orange solution was obtained. The solution was put under vacuum on the rotary evaporator until a milk color precipitate was obtained and it was again removed through filtration. The dark orange solution was put under diethyl ether atmosphere for 3 days until an orange solid was obtained. The orange crystals were recovered and washed multiple times with diethyl ether, then dried under vacuum with the rotary evaporator and finally high vacuum pump (MM = 1882.24 g/mol, 1.43 g, 41% yield).

Analysis & Characterization:

FTIR (KBr, cm^{-1}): 3444 (m, br), 2960 (s), 2943 (s), 2873 (s), 2360 (w), 1646 (s), 1480 (s), 1381 (m), 1039 (s), 939 (s), 919 (s), 902 (s), 800 (w), 663 (s), 562 (m), 460 (m), 411 (w).

ESI-MS (-) CH_3CN: 1639.7 ($[M\text{-}TBA]^-$), 1518 ($[2M\text{-}3TBA+H]^{2-}$), 1397.6 ($[M\text{-}2TBA+H)^-]$, 698.5 ($[M\text{-}2TBA]^{2-}$).

SYNTHESIS 3A:

Synthesis of "POM-SUCC" $[(C_4H_9)_4N]_3[MnMo_6O_{18}\{(OCH_2)_3CNHCO(CH_2)_2COOH\}_2]$

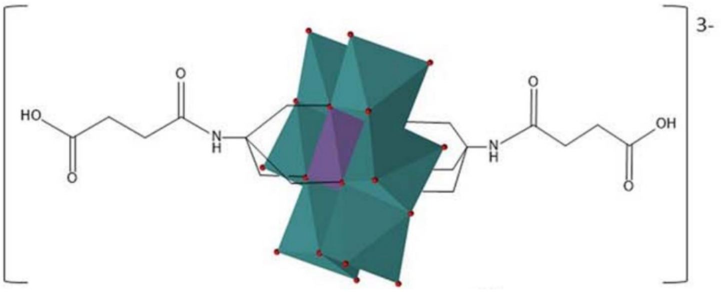

Reaction:

$$[(C_4H_9)_4N]_3[MnMo_6O_{18}\{(OCH_2)_3CNH_2)_2] + 2C_4H_4O_3 \xrightarrow[DMF,\ 50°C,\ 24\,hours]{} [(C_4H_9)_4N]_3[MnMo_6O_{18}\{(OCH_2)3CNHCO(CH_2)_2COOH\}_2]$$

Procedure:

POM-TRIS (0.73228g, $3.89x10^{-3}$ mol) was dissolved in 8 mL of DMF in a vial, and succinic anhydride $C_4H_4O_3$ was added (0.78875g, $7.78x10^{-3}$ mol). The orange reaction mixture was stirred at 50°C for one day without any noticeable color change. The solution was then cooled at room temperature and crystallized under diethyl ether atmosphere. After 1 day, the orange crystals were recovered and washed multiple times with diethyl ether, then dried under vacuum. (MM = 2082,32 g/mol, 0.70440g, 86% yield).

Analysis & Characterization:

FTIR (KBr, cm^{-1}): 3386 (m, br), 3072 (m), 2962 (s), 2943 (s), 2875 (m), 1718 (m), 1684 (s), 1540 (m), 1483 (m), 1382 (w), 1183 (w), 1068 (w), 1025 (m), 942 (s), 920 (s), 814 (w), 665 (s), 564 (w), 460 (w).

ESI-MS (-) CH_3CN: 2082.0 ($[M-H]^-$), 1839.8 ($[M-TBA]^-$), 1717.3 ($[2M-3TBA+H]^{2-}$), 1597.7 ($[M-2TBA+H]^-$), 1148 ($[2M-3TBA]^{3-}$).

SYNTHESIS 4A:

Synthesis of "POM-NHS" $[(C_4H_9)_4N]_3[MnMo_6O_{18}\{(OCH_2)_3CNHCO(CH_2)_2CO(C_4H_4NO_3)\}_2]$

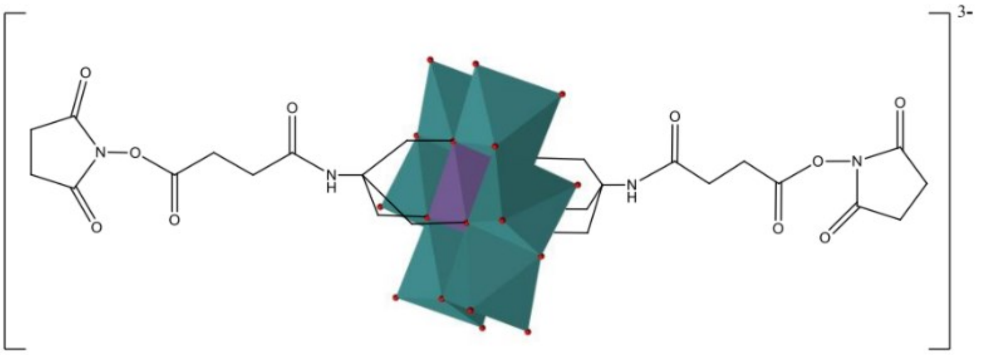

Reaction:

$[(C_4H_9)_4N]_3[MnMo_6O_{18}\{(OCH_2)_3CNHCO(CH_2)_2COOH\}_2] + 2\ C_4H_5NO_3$
$\xrightarrow[DMF,\ R.T,\ 24\,h.]{DCC} [(C_4H_9)_4N]_3[MnMo_6O_{18}\{(OCH_2)_3CNHCO(CH_2)_2CO(C_4H_4NO_3)\}_2]$

Procedure:

POM-SUCC (70.55 mg; 0,0339 mmol) was dissolved 1.5 mL of DMF in a vial. In order, NHS (18.08 mg, 0.15 mmol) and DCC (44.72 mg, 0.21 mmol) were added to the reaction mixture, and the orange solution was stirred for 24 hours at room temperature. The day after, the orange solution was centrifuged to remove a minor white precipitate and it was put under diethyl ether atmosphere to crystallize. After a few hours the orange needle-shaped crystals were recovered and washed with approximately 1.5 mL of diethyl ether for three times, dried under vacuum, and finally weighted (MM = 2276.55 g/mol, 0,018 mmol, 54% yield).

Analysis & Characterization:

FTIR (KBr, cm^{-1}): 3497 (m, br), 3271 (m), 3224 (m), 3062 (m), 2961 (s), 2935 (s), 2872 (s). 2119 (m), 1814 (m), 1782 (m), 1739 (s), 1660 (s), 1553 (m), 1484 (m), 1414 (w), 1387 (m), 1331 (w), 1225 (w), 1210 (m), 1150 (w), 1098 (s), 1061 (s), 1028 (s), 939 (s), 917 (s), 902 (s), 810 (w), 668 (s), 561 (m), 516 (w), 458 (w), 407 (w).

ESI-MS (-) CH_3CN: 2033.7 ($[M\text{-}TBA]^-$), 1793.6 ($[M\text{-}2TBA+H]^-$), 1553.4 ($[M\text{-}3TBA+2H]^-$), 516.4 ($[M\text{-}3TBA]^{3-}$)

SYNTHESIS 5A:

Synthesis of "$MnMo_6$ POM – L-Phe" $[(C_4H_9)_4N]_3[MnMo_6O_{18}\{(OCH_2)_3CNHCO(CH_2)_2COPheOMe\}_2]$

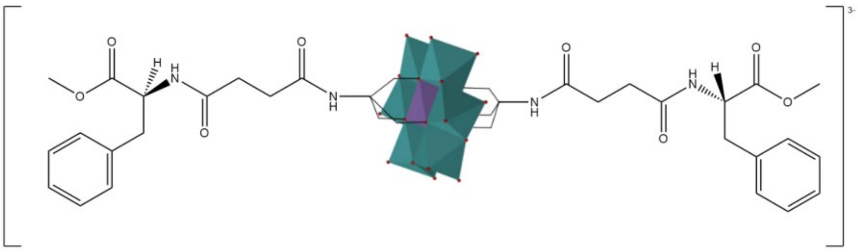

Reaction:

$[(C_4H_9)_4N]_3[MnMo_6O_{18}\{(OCH_2)_3CNHCO(CH_2)_2CO(C_4H_4NO_3)\}_2]$ +

$$+ \ 2\text{L-PheOMe}\cdot\text{HCl} \xrightarrow[DMF\ R.T.]{DIPEA} [(C_4H_9)_4N]_3[MnMo_6O_{18}\{(OCH_2)_3CNHCO(CH_2)_2COPheOMe\}_2]$$

Procedure:

POM-NHS (42.06 mg; 0.0185 mmol) has been dissolved in 1.5 mL of DMF in a vial. In order, L-PheOMe·HCl (9.50 mg, 0.044 mmol) and DIPEA (33 mg, 44 µL, 0.25 mmol) were added to the reaction mixture, and the orange solution was stirred for 24 hours at room temperature. The day after the vial was put under diethyl ether atmosphere to crystallize. After a few hours the orange greasy product was recovered and washed with approximately 1.5 mL of diethyl ether for three times and then dried under vacuum, and finally weighted (MM = 2404.86 g/mol, 0.034 g, 54% yield).

Analysis & Characterization:

FTIR (KBr, cm^{-1}): 3441 (m, br), 3372 (m), 3279 (m), 2961 (s), 2874 (m), 1738 (m), 1664 (s), 1543 (m), 1483 (m), 1384 (w), 1220 (w), 1064 (m), 1028 (m), 941 (s), 920 (s), 742 (w), 669 (s), 562 (w).

ESI-MS (-) CH_3CN: 2161.0 ([M-TBA]$^-$), 2042.9 ([2M-3TBA+H]$^{2-}$), 1919.8 ([M-2TBA+H]$^-$), 1677.5 ([M-3TBA+2H)$^-$], 1361.8 ([2M-3TBA)$^{3-}$].

^{1}H NMR (300MHz, CD_3CN, δ, ppm): 0.96 (t, $^+N(CH_2CH_2CH_2\mathbf{CH_3})_4$, 36H), 1.33 (m, $^+N(CH_2CH_2\mathbf{CH_2}CH_3)_4$, 24H), 1.59 (m, $^+N(CH_2\mathbf{CH_2}CH_2CH_3)_4$, 24H), 3.07 (m, $^+N(\mathbf{CH_2}CH_2CH_2CH_3)_4$, 24H), 3.64 (s, -O**CH**$_3$, 6H), 4.59 (s, CH phenylalanine, 2H), 6.78 (m, -(CO)**NH-**, 2H)**,** 7.1-7.4 (m, aromatic Phe of amino acid, 10H), 7.92 (s, NH TRIS, 2H), 65.89 (s, CH_2 TRIS, 12H).

UV-Vis (CH_3CN): Main band under 190 nm (ε_{190}=215200 cm^{-1}M^{-1}). Shoulder between 230 nm (ε_{230}=80000 cm^{-1}M^{-1}) and 205 nm (ε_{205}=128000 cm^{-1}M^{-1}).

CD (CH_3CN): Positive dichroic signals, with two bands recalling those of L-Phe. The maximums of intensity are located at 196 nm ([θ]=112806 deg*cm^2*dmol^{-1}) and 219 nm ([θ]=42729 deg*cm^2*dmol^{-1}).

Elemental Analysis: Calculated for $C_{84}H_{154}MnMo_6O_{32}N_7$: C 41.95%, H 6.45%, N 4.08%. Found: C 40.81%, H 6.87%, N 4.83%

SYNTHESIS 6A:

Synthesis of "$MnMo_6$ POM-DB"
$[(C_4H_9)_4N]_3[MnMo_6O_{18}\{(OCH_2)_3CNHCO(CH_2)_2CO(C_{49}H_{68}N_{13}O_9)\}_2]$

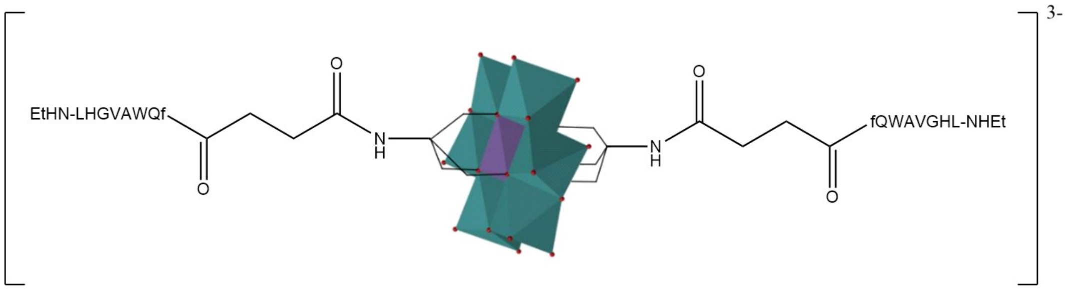

Reaction:

$[(C_4H_9)_4N]_3[MnMo_6O_{18}\{(OCH_2)_3CNHCO(CH_2)_2CO(C_4H_4NO_3)\}_2]$ + 2 $C_{49}H_{68}N_{13}O_9$ $\xrightarrow[DMF\ R.T.]{DIPEA}$ $[(C_4H_9)_4N]_3[MnMo_6O_{18}\{(OCH_2)_3CNHCO(CH_2)_2CO(C_{49}H_{68}N_{13}O_9)\}_2]$

Procedure:

POM-NHS (20.25 mg; 0.0089 mmol) has been dissolved in 1.2 mL of DMF in a vial. In order Demobesin-1 (20.28 mg, 0.021 mmol) and DIPEA (18 mg, 24 µL, 0.13 mmol) were added to the reaction mixture, and the slightly orange solution was been stirred for 24 hours at room temperature. The day after the vial was put under diethyl ether atmosphere to crystallize. After 24 hours the greasy milk color solid was recovered and washed with approximately 1.5 mL of diethyl ether for three times. The solid was then dissolved in 2 mL of DMF and put in diethyl ether atmosphere to crystallize for a weekend. The spongy product was then washed with diethyl ether and redissolved in DMF to attempt the crystallization under diethyl ether atmosphere. After two attempts lasting several days, a greasy milk color solid was obtained. The solid was washed with diethyl ether multiple times, put under vacuum, and finally weighted (MM = 4014.76 g/mol, 0.02985 g, 84% yield).

Analysis & Characterization:

FTIR (KBr, cm^{-1}): 3470 (m, br), 3285 (s, br), 3062 (w), 2961 (m), 2929 (m), 2873 (m), 1660 (s, br), 1540 (s, br), 1439 (m), 1409 (w), 1387 (m), 1342 (w), 1254 (m), 1157 (w), 1100 (m), 1061 (m), 1025 (m), 942 (s), 920 (s), 810 (w), 745 (m), 671 (s), 563 (w), 518 (w), 461 (w).

ESI-MS (-) CH_3CN: 1095.0 ($[M\text{-}3TBA]^{3-}$),1643.6 ($[M\text{-}3TBA+H]^{2-}$), 1763.6 ($[M\text{-}2TBA]^{2-}$).

UV (TFE-H_2O 1:10): Maximum at 193 nm (ε_{193}=289600 cm^{-1}M^{-1}) and weak shoulder between 215 nm (ε_{215}=120000 cm^{-1}M^{-1}) and 198 nm (ε_{193}=248000 cm^{-1}M^{-1}).

CD (TFE-H_2O 1:10): Minimum located at 202 nm ([θ]=-109508 deg*cm^2*dmol^{-1}) and maximum at 190.5 nm ([θ]=108404 deg*cm^2*dmol^{-1}).

SYNTHESIS 7A:

Synthesis of "$MnMo_6$ POM-EEEEβAla-fQWAVGHL-NHEt"

$[(C_4H_9)_4N]_3[MnMo_6O_{18}\{(OCH_2)_3CNHCO(CH_2)_2CO(C_{72}H_{101}N_{18}O_{22})\}_2]$

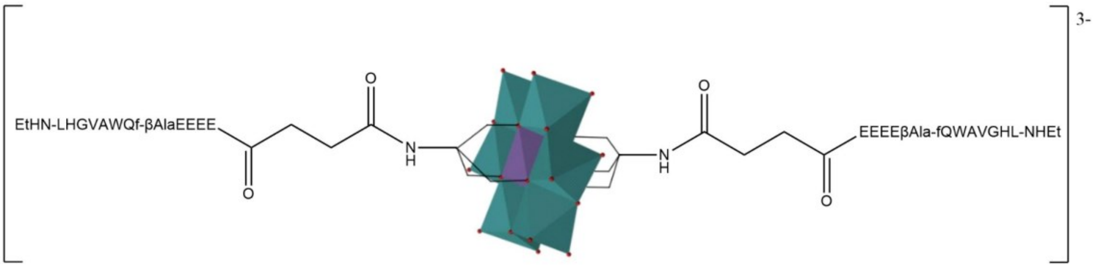

Reaction:

$[(C_4H_9)_4N]_3[MnMo_6O_{18}\{(OCH_2)_3CNHCO(CH_2)_2CO(C_4H_4NO_3)\}_2] + 2$
$C_{72}H_{101}N_{18}O_{22} \xrightarrow[DMF\ R.T.]{DIPEA}$

$[(C_4H_9)_4N]_3[MnMo_6O_{18}\{(OCH_2)_3CNHCO(CH_2)_2CO(C_{72}H_{101}N_{18}O_{22})\}_2]$

Procedure:

POM-NHS (10.63 mg; 0.0047 mmol) has been dissolved in 0.8 mL of DMF in a vial. In order EEEEβAla-fQWAVGHL-NHEt (16.50 mg, 0.011 mmol) and DIPEA (9.6 mg, 13 µL, 0.075 mmol) were added to the reaction mixture, and the orange solution was stirred for 24 hours at room temperature. The day after the vial was put under diethyl ether atmosphere to crystallize. After a few hours the greasy light orange product was recovered and washed with approximately 1.5 mL of diethyl ether for three times and then dried under vacuum and finally weighted (MM = 5189.2 g/mol, 0.023 g, 95% yield).

Analysis & Characterization:

FTIR (KBr, cm^{-1}): 3296 (m, br), 3061 (w, br), 2962 (m), 2934 (m), 2874 (m), 1656 (s, br), 1539 (s), 1452 (w), 1388 (m), 1252 (w), 1102 (w), 1062 (w), 1023 (w), 943 (m), 922 (m), 746 (w), 670 (s), 540 (w), 460 (w), 416 (w).

ESI-MS (-) CH_3CN: 1487.0 ($[M\text{-}3TBA]^{3-}$), 1503.4 ($[M\text{-}3TBA\text{-}2H\text{+}2Na]^{3-}$), 1574.5 ($[M\text{-}2TBA\text{-}2H\text{+}Na]^{3-}$).

UV (TFE-H_2O 2:10): Maximum at <190 nm (ε_{190}=289600 $cm^{-1}M^{-1}$) and shoulder at 218 nm (ε_{218}=112000 $cm^{-1}M^{-1}$).

CD (TFE-H_2O 2:10): Minimum located at 205 nm ([θ]=-269470 deg*cm^2*$dmol^{-1}$) and maximum under 190 nm ([θ]=404754 deg*cm^2*$dmol^{-1}$ at 190 nm).

SYNTHESIS 8A:

Synthesis of “$MnMo_6$-TtdsDB”

$[(C_4H_9)_4N]_3[MnMo_6O_{18}\{(OCH_2)_3CNHCO(CH_2)_2CO(C_{63}H_{94}N_{15}O_{14})\}_2]$

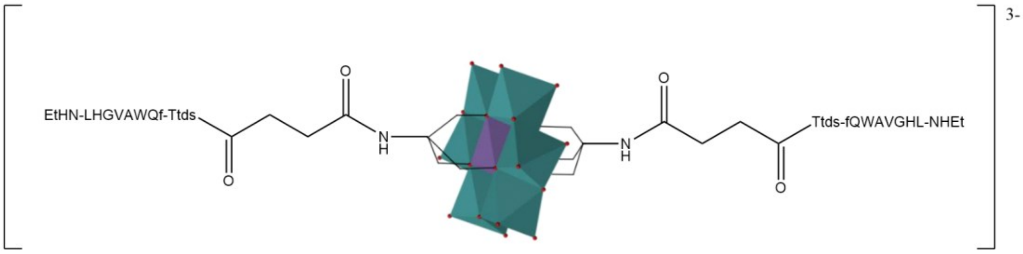

Reaction:

$[(C_4H_9)_4N]_3[MnMo_6O_{18}\{(OCH_2)_3CNHCO(CH_2)_2CO(C_4H_4NO_3)\}_2] + 2\ C_{63}H_{94}N_{15}O_{14}$ $\xrightarrow[DMF\ R.T.]{DIPEA}$ $[(C_4H_9)_4N]_3[MnMo_6O_{18}\{(OCH_2)_3CNHCO(CH_2)_2CO(C_{63}H_{94}N_{15}O_{14})\}_2]$

Procedure:

POM-NHS (9.24 mg; 0.0041 mmol) has been dissolved in 0.8 mL of DMF in a vial. In order Ttds-fQWAVGHL-NHEt (12.46 mg, 0.0097 mmol) and DIPEA (7.42 mg, 10 µL, 0.057 mmol) were added to the reaction mixture, and the yellow-orange solution was stirred for 24 hours at room temperature. The day after the vial was put under diethyl ether atmosphere to crystallize. After 96 hours the milk colour product was recovered and washed with approximately 1.5 mL of diethyl ether for three times and then dried under vacuum for several hours, and finally weighted (MM = 4619.48g/mol, 0.017 g, 90% yield).

Analysis & Characterization:

FTIR (KBr, cm^{-1}): 3429 (m, br), 3284 (s), 3076 (w), 2961 (m), 2926 (m), 2874 (m), 1660 (s), 1629 (s), 1549 (m), 1448 (w), 1386 (w), 1256 (w), 1099 (w), 1017 (w), 943 (s), 920 (s), 742 (w), 669 (s), 566 (w), 406 (m).

ESI-MS (-) CH_3CN: 2067.5 ($[M\text{-}2TBA]^{2-}$), 1947.8 ($[M\text{-}3TBA+H]^{2-}$), 1299.6 ($[M\text{-}3TBA]^{3-}$).

UV (TFE-H_2O 1:10): Maximum at <190 nm (ε_{190}=244800 $cm^{-1}M^{-1}$) and shoulder at 217 nm (ε_{217}=115200 $cm^{-1}M^{-1}$).

CD (TFE-H_2O 1:10): Minimum at 203 nm ([θ]=-160978 deg*cm^2*dmol^{-1}) and maximum under 190 nm ([θ]=107838 deg*cm^2*dmol^{-1} at 190 nm).

SYNTHESIS 9A:

Synthesis of "MnMo$_6$-c(RGDfK)"

$[(C_4H_9)_4N]_3[MnMo_6O_{18}\{(OCH_2)_3CNHCO(CH_2)_2CO(C_{27}H_{40}N_9O_7)\}_2]$

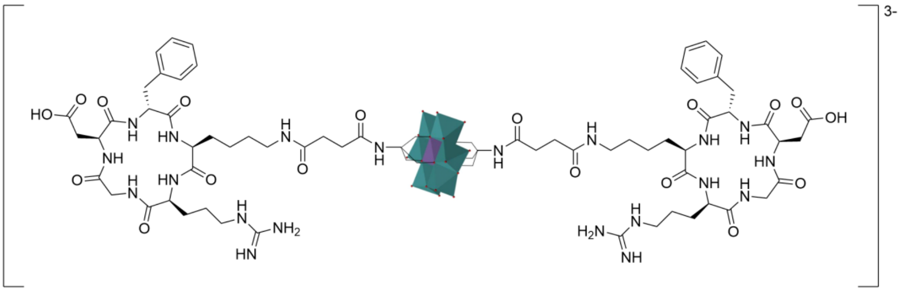

Reaction:

$[(C_4H_9)_4N]_3[MnMo_6O_{18}\{(OCH_2)_3CNHCO(CH_2)_2CO(C_4H_4NO_3)\}_2] + 2\ C_{27}H_{41}N_9O_7$
$\xrightarrow[DMF\ R.T.]{DIPEA} [(C_4H_9)_4N]_3[MnMo_6O_{18}\{(OCH_2)_3CNHCO(CH_2)_2CO(C_{27}H_{40}N_9O_7)\}_2]$

Procedure:

POM-NHS (20.92 mg; 0.0092 mmol) was dissolved in 0.6 mL of DMF in a vial. In c(RGDfK) (12.76 mg, 0.021 mmol) and DIPEA (16.4 mg, 22 μL, 0.12 mmol) were added to the reaction mixture, and the yellow solution has been stirred for 24 hours at room temperature. The day after the transparent solution was put under diethyl ether atmosphere for the crystallization. After 72 hours the pale orange colour product was recovered and washed with approximately 1.5 mL of diethyl ether for two times, then dried under vacuum, and finally weighted (MM = 3253.68g/mol, 0.023 g, 76% yield).

Analysis & Characterization:

FTIR (KBr, cm^{-1}): 3417 (s, br), 3057 (w), 2957 (w), 2935 (w), 2877 (w), 1660 (s), 1541 (m), 1377 (w), 1575 (w), 1107 (w), 1057 (w), 1021 (w), 943 (s), 921 (s), 915 (m), 670 (s), 570 (w).

ESI-MS (-) CH_3CN: 1386 ([M-2TBA]$^{2-}$), 1261.9 ([M-3TBA+H]$^{2-}$).

UV (TFE-H_2O 1:10): Maximum at <190 nm (ε_{190}=241600 cm^{-1}M^{-1}) and shoulder at 214 nm (ε_{214}=110400 cm^{-1}M^{-1}).

CD (TFE-H_2O 1:10): Minimum at 204 nm ([θ]=-163257 deg*cm^2*dmol^{-1}) and maximum under 190 nm ([θ]=78891 deg*cm^2*dmol^{-1} at 190 nm).

SYNTHESIS 2B:

Synthesis of "V_6-OH" - $[(C_4H_9)_4N]_2[V_6O_{13}\{(OCH_2)_3CCH_2OH\}_2]$

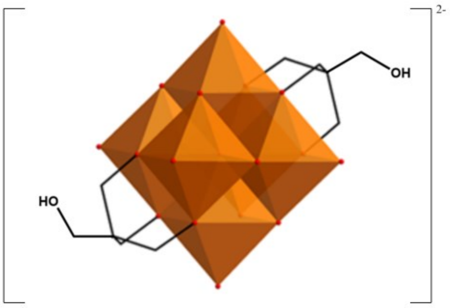

Reaction:

$$6NaVO_3 + 4HCl + 2(C_4H_9)_4BrN + 2(HOCH_2)_3CCH_2OH \xrightarrow[H_2O,\ 80°C,\ 48\ hours]{}$$

$$[(C_4H_9)_4N]_2[V_6O_{13}\{(OCH_2)_3CCH_2OH\}_2] + 5H_2O + 4NaCl + 2NaBr$$

Procedure:

In a round-bottom flask $NaVO_3 \cdot H_2O$ (5.00g, 0.036mol) was dissolved in 120 mL of H_2O under mild heating (≈50°C) and vigorous stirring until a clear almost colorless solution was obtained. The solution was cooled to room temperature and a 3.8375M solution of HCl (8.65 mL, 0.033 mol) was added dropwise with a burette, monitoring the pH level with a universal indicator until it reached pH=3. During the titration experiment the solution passed from being colorless to yellow, then orange, then red, till when it stabilized on a bright orange coloration. $(HOCH_2)_3CCH_2OH$ (3.75g, 0.028 mol) was added to the solution and the mixture was heated to 80°C for 48 hours using a reflux condenser attached to it. The final brown/dark orange mixture was cooled to room temperature and added dropwise to a previously prepared TBA-Br solution (10g, 0.031 mol in 20 mL H_2O) under powerful stirring until a red-orange solid was formed. The crude product was filtered on a fitted funnel and washed with 50 mL of H_2O, 80 mL of diethyl ether, monitoring its purity by ESI-MS and FT-IR, then it was dried under vacuum. A light orange powder was obtained (5.07g, 67% yield).

Analysis & Characterization:

FTIR (KBr, cm^{-1}): 3376 (m, br), 2962 (s), 2943 (s), 2873 (s), 1640 (m), 1481 (s), 1383 (m), 1263 (w), 1123 (s), 1074 (m), 1034 (s), 951 (s), 884 (w), 810 (s), 794 (s), 713 (s), 650 (m), 580 (s), 513 (w), 490 (w), 420 (s).

ESI-MS (-) CH_3CN: 1022 ([M-TBA]$^-$), 780.6 ([M-2TBA+H]$^-$).

SYNTHESIS 3B:

Synthesis of "V_6-O-Succinate"

$[(C_4H_9)_4N]_2[V_6O_{13}\{(OCH_2)_3CCH_2OOCCH_2CH_2COOH\}_2]$

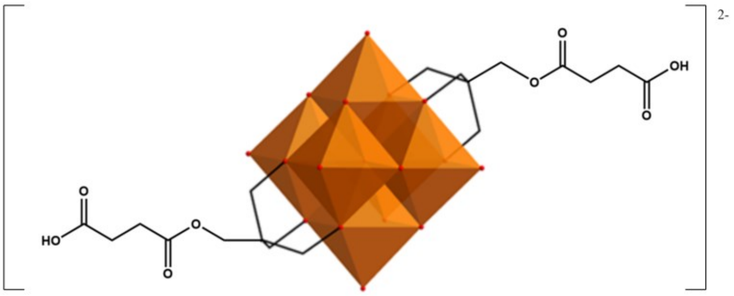

Reaction:

$$[(C_4H_9)_4N]_2[V_6O_{13}\{(OCH_2)_3CCH_2OH\}_2] + 2C_4H_4O_3 \xrightarrow[ACN,\ 50°C,\ 48\ hours]{DMAP,\ TEA} [(C_4H_9)_4N]_2[V_6O_{13}\{(OCH_2)_3CCH_2OOCCH_2CH_2COOH\}_2]$$

Procedure:

In a round-bottom flask $[(C_4H_9)_4N]_2[V_6O_{13}\{(OCH_2)_3CCH_2OH\}_2]$ (1.11962g, 8.85x10^{-4} mol) was dissolved in 40 mL acetonitrile until a clear orange solution was obtained. TEA (0.34 mL, ρ=0.726 g/mL, 2.44x10^{-3} mol) and then DMAP (0.06, 4.91x10^{-4} mol) were added to the mixture and a color change from orange to red orange was noticed. The mixture was heated at 50°C for 48 hours using a reflux condenser. The turbid orange solution was filtered to remove an orange precipitate. It was later put under vacuum to the rotary evaporator and the solvent was evaporated until a white precipitate was obtained and removed by filtration. The dark red solution was finally put in a beaker of cold water and the obtained red powder was collected on a fitted funnel, washed with cold water and finally dried under vacuum (0.68g, 52% yield).

Analysis & Characterization:

FTIR (KBr, cm^{-1}): 3444 (m, br), 2960 (s), 2932 (m), 2872 (m), 1738 (s), 1649 (w), 1469 (s), 1396 (w), 1380 (w), 1336 (w), 1265 (m), 1247 (m), 1224 (m), 1191 (m), 1161 (m), 1132 (s), 1061 (s), 1036 (m), 1000 (m), 950 (s), 933 (s), 879 (w), 810 (s), 723 (s), 582 (m), 417 (s).

ESI-MS (-) CH_3CN: 1221.9 ($[M\text{-}TBA]^-$), 980.8 ($[M\text{-}2TBA+H]^-$).

SYNTHESIS 4B:

Synthesis of “V_6-O-NHS”
$[(C_4H_9)_4N]_2[V_6O_{13}\{(OCH_2)_3CCH_2OOCCH_2CH_2CO(C_4H_4NO_3)\}_2]$

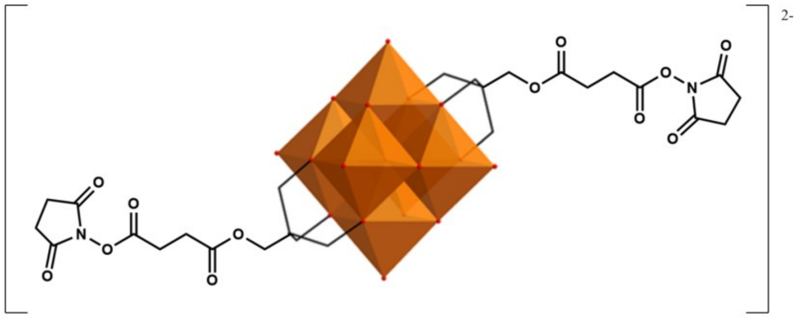

Reaction:

$$[(C_4H_9)_4N]_2[V_6O_{13}\{(OCH_2)_3CCH_2OOCCH_2CH_2COOH\}_2] + 2C_4H_5NO_3 \xrightarrow[DMF\ R.T.]{DCC} [(C_4H_9)_4N]_2[V_6O_{13}\{(OCH_2)_3CCH_2OOCCH_2CH_2CO(C_4H_4NO_3)\}_2]$$

Procedure:

V_6-O-Succinate (95.28mg, 6.50×10^{-2} mmol) was dissolved in 2 mL of DMF in a vial until a clear red-orange solution was obtained, then NHS (34.26mg, 0.26 mmol) was added without any noticeable color change. The DCC (85.01mg, 0.39 mmol) was added to the mixture and a color change toward a darker red shade was reported. The solution was stirred for 24 hours at room temperature and the day after the brown mixture was put under diethyl ether for 5 days until red needle shaped crystals were obtained. They were recovered and washed multiple times with diethyl ether and finally dried under vacuum (53.89 mg, 50% yield).

Analysis & Characterization:

FTIR (KBr, cm^{-1}): 3444 (m, br), 2962 (s), 2937 (m), 2875 (m), 1814 (w), 1783 (w), 1739 (s), 1667 (w), 1482 (w), 1383 (w), 1252 (w), 1205 (w), 1132 (w), 1085 (m), 954 (s), 883 (w), 809 (s), 719 (s), 648 (w), 582 (m), 422 (m).

ESI-MS (-) CH$_3$CN: 1415.5 ([M-TBA]$^-$), 1174.7 ([M-2TBA+H]$^-$), 1196 ([M-2TBA+Na]$^-$).

^{1}H NMR (300MHz, CD$_3$CN, δ, ppm): 0.96 (t, $^+N(CH_2CH_2CH_2\mathbf{CH_3})_4$ TBA, 24H), 1.35 (s, $^+N(CH_2CH_2\mathbf{CH_2}CH_3)_4$ TBA, 16H), 1.60 (m, $^+N(CH_2CH_2\mathbf{CH_2}CH_3)_4$ TBA, 16H), 2.66 (t, -OC$\mathbf{CH_2}$CH$_2$CO-, 4H), 2.77 (s, DMF solvent impurities, overlapped with -CH$_2$- from NHS, (3+4)H), 2.85 (m, -OC$\mathbf{CH_2}$CH$_2$CO-, 4H), 3.10 (m, $^+N(\mathbf{CH_2}CH_2CH_2CH_3)_4$ TBA, 16H), 3.95 (s, -C$\mathbf{CH_2}$O- TRIS, 4H), 5.01 (s, -C(CH$_2$O-)$_3$, 12H).

^{51}V NMR (78.9MHz, CD$_3$CN, δ, ppm): -497.4 (s, br)

UV-Vis (ACN): Maximum at 195 nm (ε_{195} = 38400 cm^{-1}M^{-1}), and shoulder at 221 nm (ε_{221}=44800 cm^{-1}M^{-1}).

Elemental Analysis: Calculated for $C_{50}H_{96}V_6O_{25}N_4$: C 41.16%, H 6.63%, N 3.84%. Experimental: C 42.18%, H 6.55%, N 4.10%.

SYNTHESIS 5B:

Synthesis of “V$_6$-O – L-Phe”

$[(C_4H_9)_4N]_2[V_6O_{13}\{(OCH_2)_3CCH_2OOCCH_2CH_2COPheOMe\}_2]$

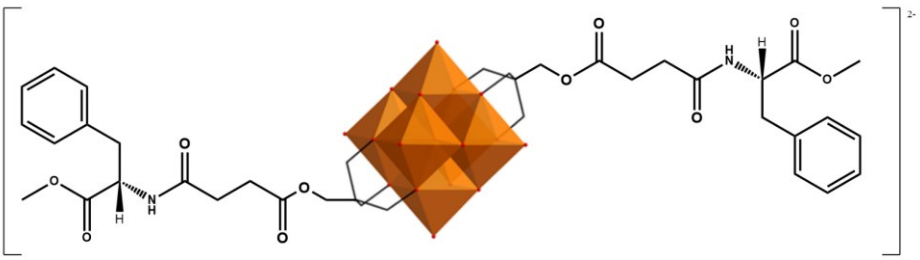

Reaction:

$[(C_4H_9)_4N]_2[V_6O_{13}\{(OCH_2)_3CCH_2OOCCH_2CH_2CO(C_4H_4NO_3)\}_2]$ +

2L-PheOMe·HCl $\xrightarrow[DMF\ R.T.]{DIPEA}$

$[(C_4H_9)_4N]_2[V_6O_{13}\{(OCH_2)_3CCH_2OOCCH_2CH_2COPheOMe\}_2]$

Procedure:

V$_6$O-NHS (40.50 mg; 0.0244 mmol) has been dissolved in 2.0 mL of DMF in a vial. In order L-PheOMe·HCl (14.70 mg, 0.068 mmol) and DIPEA (13 mg, 18 μL, 0.1 mmol) were added to the reaction mixture, and the dark orange solution was stirred for 24 hours at room temperature. The day after the vial was put under diethyl ether atmosphere to crystallize. After 24 hours the dark orange greasy product was recovered and washed with approximately 1.5 mL of diethyl ether for four times and then dried under vacuum, and finally weighted (MM = 1787.42 g/mol, 0.03810 g, 86% yield).

Analysis & Characterization:

FTIR (KBr, cm^{-1}): 3435 (m, br), 2961 (s), 2936 (m), 2874 (m), 1740 (s), 1668 (s), 1539 (m), 1465 (m), 1386 (m), 1212 (w), 1161 (m), 1131 (s), 1058 (s), 953 (s), 809 (s), 719 (s), 583 (s), 420 (s).

ESI-MS (-) CH$_3$CN: 1544.2 ([M-TBA]$^-$), 1302.9 ([M-2TBA+H]$^-$), 650.9 ([M-2TBA]$^{2-}$)

^{1}H NMR (300MHz, CD$_3$CN; δ, ppm): 0.97 (t, $^+N(CH_2CH_2CH_2\mathbf{CH_3})_4$ TBA, 24H), 1.37 (m, $^+N(CH_2CH_2\mathbf{CH_2}CH_3)_4$ TBA, 18H), 1.62 (m, $^+N(CH_2\mathbf{CH_2}CH_2CH_3)_4$ TBA, 16H), 3.11 (t, $^+N(\mathbf{CH_2}CH_2CH_2CH_3)_4$ TBA, 18H), 3.63 (s, -OCH$_3$, 6H), 5.03 (s, -C(CH$_2$O-)$_3$, 12H), 3.91 (s, -CCH$_2$O-, 4H), 6.66 (d, -C=ONH-, 2H), 7.16-7.36 (m, aromatic ring Phe, 10H).

^{51}V NMR (78.9MHz, CD$_3$CN; δ, ppm): -499.75 (s, br)

UV (CH$_3$CN): Maximum at 191 nm (ε_{191}=150400 cm^{-1}M^{-1}), shoulder at 209 nm (ε_{209}=69600 cm^{-1}M^{-1}).

CD (CH$_3$CN): Maximum at 195 nm ([θ]=122438 deg*cm^2*dmol^{-1}) and approximately 216 nm ([θ]=35933 deg*cm^2*dmol^{-1}).

SYNTHESIS 6B:

Synthesis of “V_6-O - DB”
$[(C_4H_9)_4N]_2[V_6O_{13}\{(OCH_2)_3CCH_2OOCCH_2CH_2CO(C_{49}H_{68}N_{13}O_9)\}_2]$

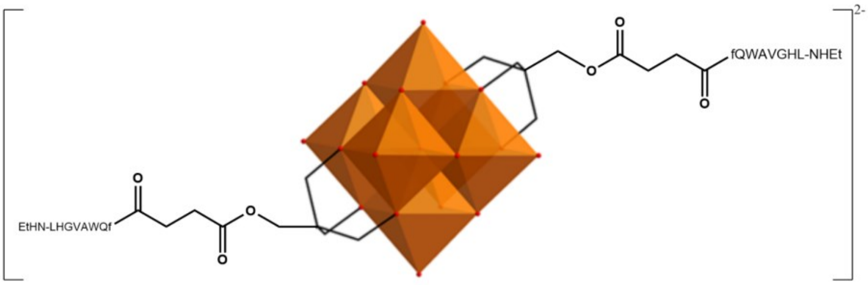

Reaction:

$$[(C_4H_9)_4N]_2[V_6O_{13}\{(OCH_2)_3CCH_2OOCCH_2CH_2CO(C_4H_4NO_3)\}_2] + 2\ C_{49}H_{68}N_{13}O_9$$
$$\xrightarrow[DMF\ R.T.]{DIPEA} [(C_4H_9)_4N]_2[V_6O_{13}\{(OCH_2)_3CCH_2OOCCH_2CH_2CO(C_{49}H_{68}N_{13}O_9)\}_2]$$

Procedure:

V_6O-NHS (8.17 mg; 0.0049 mmol) was dissolved in 0.8 mL of DMF in a vial. In order Dembesin-1 (10.05 mg, 0.010 mmol) and DIPEA (9.6 mg, 13 µL, 0.075 mmol) were added to the reaction mixture, and the orange solution has been stirred for 24 hours at room temperature. The day after the vial was put under diethyl ether atmosphere to crystallize. After a few hours the white powder was recovered and washed with approximately 1.5 mL of diethyl ether for four times and then dried under vacuum, and finally weighted (MM = 3395.3 g/mol, 0.01217 g, 73% yield).

Analysis & Characterization:

FTIR (KBr, cm^{-1}): 3291 (s, br), 3061 (w), 2962 (m), 2933 (m), 2872 (m), 1738 (m), 1647 (s, br), 1533 (s, br), 1452 (w), 1389 (w), 1233 (w), 1160 (w), 1130 (w), 1055 (m), 955 (s), 880 (w), 809 (m), 716 (m), 586 (m), 420 (m).

ESI-MS (-) CH_3CN: 1455.9 ($[M\text{-}2TBA]^{2-}$)

UV (TFE/H_2O) 1:10: Maximum at 191.5 nm (ε_{191}=169600 cm^{-1}M^{-1}) and a shoulder at 218 nm (ε_{212}=112800 cm^{-1}M^{-1}).

CD (TFE/H_2O) 1:10: Minimum located at 207 nm ([θ]=-102122 deg*cm^2*dmol^{-1}), and the maximum at 192 nm ([θ]=114616 deg*cm^2*dmol^{-1}).

^{51}V NMR (78.9MHz, CD_3CN; δ, ppm): -496.3 (s, br)

SYNTHESIS 7B:

Synthesis of "V_6-O - EEEEβAla-fQWAVGHL-NHEt"

$[(C_4H_9)_4N]_2[V_6O_{13}\{(OCH_2)_3CCH_2OOCCH_2CH_2CO(C_{72}H_{101}N_{18}O_{22})\}_2]$

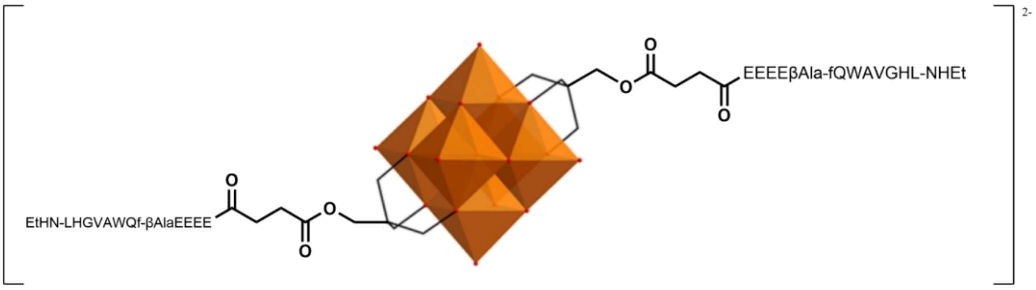

Reaction:

$[(C_4H_9)_4N]_2[V_6O_{13}\{(OCH_2)_3CCH_2OOCCH_2CH_2CO(C_4H_4NO_3)\}_2] + 2\ C_{72}H_{101}N_{18}O_{22}$ $\xrightarrow[DMF\ R.T.]{DIPEA}$ $[(C_4H_9)_4N]_2[V_6O_{13}\{(OCH_2)_3CCH_2OOCCH_2CH_2CO(C_{72}H_{101}N_{18}O_{22})\}_2]$

Procedure:

V_6O-NHS (13.64 mg; 0.00823 mmol) was dissolved in 1 mL of DMF in a vial. In order, EEEEβAla-fQWAVGHL-NHEt (29.93 mg, 0.019 mmol) and DIPEA (14.8 mg, 20 μL, 0.11 mmol) were added to the reaction mixture, and the orange solution was stirred for 24 hours at room temperature. The day after the vial was put under diethyl ether atmosphere to foster the crystallization. After 72 hours the light orange product was recovered and washed with approximately 1.5 mL of diethyl ether for three times and then dried under vacuum for 48 hours and finally weighted (MM = 4571 g/mol, 0.04277 g, 92% yield).

Analysis & Characterization:

FTIR (KBr, cm^{-1}): 3440 (m, br), 3289 (s), 3056 (w), 2955 (m), 2934 (m), 2879 (w), 1659 (s), 1539 (m), 1387 (m), 1255 (m), 1130 (w), 1052 (w), 958 (s), 808 (m), 718 (w), 578 (w), 473 (w), 426 (w).

ESI-MS (-) CH_3CN: 2163 ($[M-TBA-H]^{2-}$), 2043 ($[M-2TBA]^{2-}$), 1362 ($[M-2TBA-H]^{3-}$)

UV (TFE/H_2O 1:10): Maximum <190 nm (ε_{190}=289600 $cm^{-1}M^{-1}$) and a shoulder at 214 nm (ε_{214}=137600 $cm^{-1}M^{-1}$).

CD (Pure TFE): Minimum located at 206 nm ([θ]=-338766 deg*cm^2*$dmol^{-1}$), while the maximum is at 192 nm ([θ]=756593 deg*cm^2*$dmol^{-1}$).

^{51}V NMR (78.9MHz, CD_3CN; δ, ppm): -493.9 (s, br)

SYNTHESIS 8B:

Synthesis of "V_6-O - TtdsDB"

$[(C_4H_9)_4N]_3[V_6O_{13}\{(OCH_2)_3CCH_2OOCCH_2CH_2CO(C_{63}H_{94}N_{15}O_{14})\}_2]$

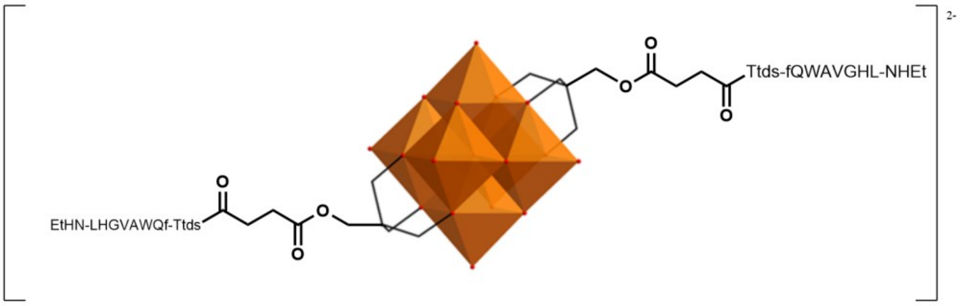

Reaction:

$[(C_4H_9)_4N]_2[V_6O_{13}\{(OCH_2)_3CCH_2OOCCH_2CH_2CO(C_4H_4NO_3)\}_2]$ + 2 $C_{63}H_{94}N_{15}O_{14}$ $\xrightarrow[DMF\ R.T.]{DIPEA}$ $[(C_4H_9)_4N]_3[V_6O_{13}\{(OCH_2)_3CCH_2OOCCH_2CH_2CO(C_{63}H_{94}N_{15}O_{14})\}_2]$

Procedure:

V_6O-NHS (8.47 mg; 0.0051mmol) was dissolved in 0.8 mL of DMF in a vial. In order, Ttds-fQWAVGHL-NHEt (15.15 mg, 0.012 mmol) and DIPEA (9.6 mg, 13 µL, 0.073 mmol) were added to the reaction mixture, and the yellow-orange solution was stirred for 24 hours at room temperature. The day after the vial was put under diethyl ether atmosphere for the crystallization of the product. After 96 h, the greasy dark red product was recovered and washed with approximately 1.5 mL of diethyl ether and then dried under vacuum at the rotary evaporator and later under high vacuum pump for multiple hours. The solid seemed to embed solvent, therefore it was spread on the surfaces of the glass vial and remained one night under vacuum finally weighted (MM = 4000.4 g/mol, 0.095 g, 46% yield).

Analysis & Characterization:

FTIR (KBr, cm^{-1}): 3429 (m, br), 3292 (s), 3071 (m), 2930 (m), 2874 (m), 1743 (m), 1664 (s), 1639 (s), 1541 (m), 1432 (w), 1386 (w), 1192 (w), 1139 (m), 1954 (m), 957 (s), 808 (m), 718 (m), 582 (m), 507 (w), 422 (m).

ESI-MS (-) CH_3CN: 1758.5 ([M-2TBA]$^{2-}$)

UV (TFE/H_2O 1:10): maximum at <190 nm (ε_{190}=289600 cm^{-1}M^{-1}) and shoulder at 218 nm (ε_{214}=120160 cm^{-1}M^{-1}).

CD (Pure TFE): The minimum for pure TFE is located at 206 nm ([θ]=-342728 deg*cm^{2}*dmol^{-1}), while the maximum is at 192 nm ([θ]=759366 deg*cm^{2}*dmol^{-1})

^{51}V NMR (78.9MHz, CD_3CN; δ, ppm): -494.7 (s, br)

SYNTHESIS 9B:

Synthesis of "V_6-O-c(RGDfK)"

$[(C_4H_9)_4N]_3[V_6O_{13}\{(OCH_2)_3CCH_2OOCCH_2CH_2CO(C_{27}H_{40}N_9O_7)\}_2]$

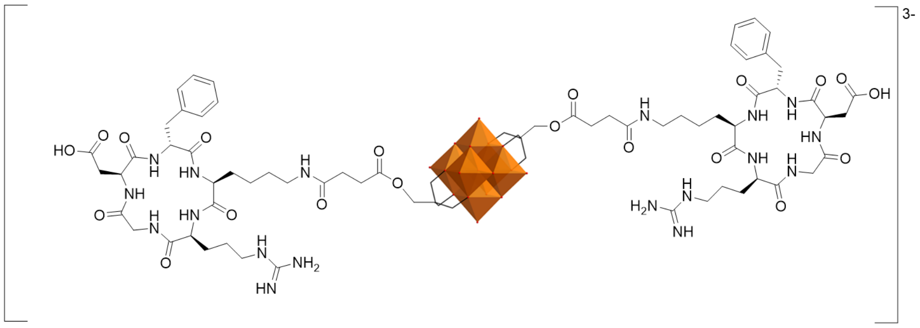

Reaction:

$$[(C_4H_9)_4N]_2[V_6O_{13}\{(OCH_2)_3CCH_2OOCCH_2CH_2CO(C_4H_4NO_3)\}_2] + 2\ C_{27}H_{41}N_9O_7 \xrightarrow[DMF\ R.T.]{DIPEA} [(C_4H_9)_4N]_3[V_6O_{13}\{(OCH_2)_3CCH_2OOCCH_2CH_2CO(C_{27}H_{40}N_9O_7)\}_2]$$

Procedure:

V_6O-NHS (14.97 mg; 0.009 mmol) was dissolved in 0.8 mL of DMF in a vial. In order, c(RGDfK) (13.54 mg, 0.022 mmol) and DIPEA (17 mg, 23 µL, 0.13 mmol) were added to the reaction mixture, and the yellow-orange solution was stirred for 48 hours at room temperature. The day after the vial was put under diethyl ether atmosphere for the crystallization of the product. After 96 h, the greasy dark red product was recovered and washed with approximately 1.5 mL of diethyl ether for two times and then dried under vacuum at the rotary evaporator and later under high vacuum pump for one week and finally weighted (MM = 2636.32 g/mol, 0.02250 g, 95% yield).

Analysis & Characterization:

FTIR (KBr, cm^{-1}): 3372 (s, br), 3061 (w, br), 2932 (m), 2859 (m), 1739 (m), 1660 (s), 1540 (m), 1438 (w), 1387 (m), 1253 (w), 1166 (w), 1131 (m), 1052 (m), 958 (s), 808 (m), 715 (m), 585 (w), 507 (w), 419 (m).

ESI-MS (-) CH_3CN: 2152.0 ([M-2TBA+H)$^-$, 1075.7 ([M-2TBA]$^{2-}$)

UV (TFE-H_2O 1:10): Maximum at <190 nm (ε_{190}=211200 cm^{-1}M^{-1}) and shoulder at 211 nm (ε_{211}=164000 cm^{-1}M^{-1}),

CD (Pure TFE): The minimum for V_6O-c(RGDfK) in pure TFE is located at 207 nm ([θ]=-79633 deg*cm^2*dmol^{-1}) and the maximum noticeable value falls at 190 nm ([θ]=73026 deg*cm^2*dmol^{-1}).

^{51}V NMR (78.9MHz, CD_3CN; δ, ppm): -496.2 (s, br)

Results and discussions

Everything dates back to 1965 when the first report on the anticancer activity of certain polyoxometalates was published. It took almost fifty years to spark a more and more increasing interest in the world of research. As previously mentioned, many are the scientific works published in the last few years which successfully aimed to functionalize both polyoxomolybdates and polyoxovanadates with biological ligands. In almost all cases the results were very promising, and the commitment of my research work is to continue the investigation on this field.[93]

Since the syntheses in this thesis are various, this chapter will be divided in two parts. The first part (syntheses A) will be dedicated to peptide coupling reactions with Mn-Anderson Evans polyoxomolybdates, while the second part (syntheses B) will be dedicated to peptide coupling reactions with polyoxovanadates.

Mn-Anderson Evans polyoxomolybdates (A)

Regarding the organic modification of POMs, as previously mentioned, the Anderson archetype is one of the best studied systems as it can be easily tris-functionalized, leading to an amino group(s) bearing structure, which can be further modified via amidation.[94] This is, indeed, the main reason for which Mn-Anderson-Evans POMs were chosen an ideal basis for the synthesis of versatile POM-ligand complexes in my thesis. The other main advantage is their good hydrolytic stability in physiological-like conditions.

In order to perform coupling reactions between polyoxometalates of molybdenum and peptides, the activate form, also called POM-NHS must be generated. The procedure is a multistep reaction, which I have performed for my thesis, and is schematized as follows.

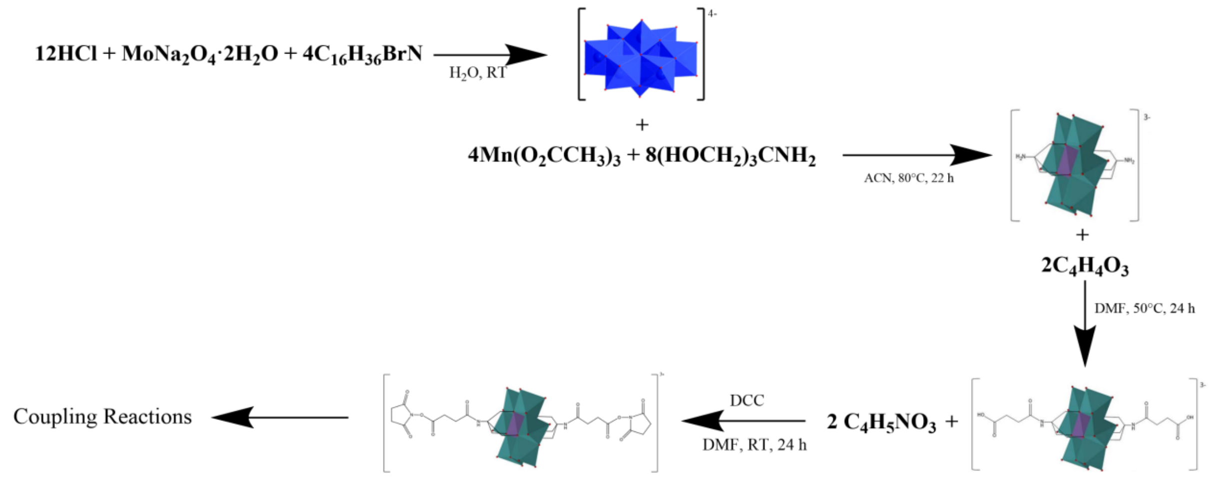

Figure 42. Various reaction steps in order to synthesize $MnMo_6$ POM – NHS. The counterions and byproducts have intentionally been omitted to avoid further confusion.

The first reaction consists in the synthesis of the polyoxometalate precursor $[Mo_8O_{26}]^{4-}$ starting from inorganic $MoNa_2O_4{\cdot}H_2O$ and $[(C_4H_9)_4N]Br$ with stoichiometric amount of HCl. The second step allows the production of tris-functionalized Mn-Anderson Evans POM through a reaction with *tris* ligands on both sides of the inorganic core. The following step allows a further functionalization with succinic anhydride to generate $MnMo_6$-succinate, and the final step, which is the reaction with n-hydroxysuccinimide (NHS) in the presence of dicyclohexylcarbodiimide (DCC) finally generates POM-NHS. In all these reactions the countercation $[(C_4H_9)_4N]^-$ is retained.

The choice of not discussing every single step in detail comes from the decision of avoiding repeating scientific knowledge which is already well established (see experimental section for details). [95–97]

Instead, I will start from the coupling reaction between POM-NHS and the amino acid L-phenylalanine, taken as a model reaction, continuing then with more complex couplings, first the simple peptide like Demobesin-1, and then analyzing the effect of introducing two spacers between the polyoxometalate and the peptide: βAlaEEEE and Ttds. A final coupling reaction between POM-NHS and RGD will also be presented.

Synthesis 5A

“MnMo$_6$ POM – L-Phe” -

$[(C_4H_9)_4N]_3[MnMo_6O_{18}\{(OCH_2)_3CNHCO(CH_2)_2COPhe\}_2]$

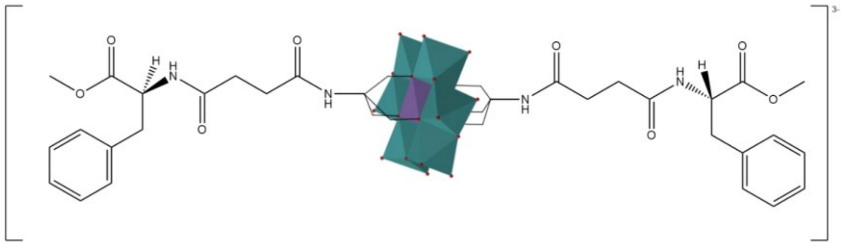

The coupling reaction between the Mn-Anderson Evans POM-NHS and L-phenylalanine, with ratio 1:2.4 has been performed in the presence of N,N-Diisopropylethylamine (DIPEA) with dimethylformamide (DMF) as solvent. The reaction time was 24 hours at room temperature, with a 54% yield. An excess of amino acid was used to avoid further purification steps to remove the unreacted POM. DIPEA is commonly used as base in amide coupling reactions between a carboxylic acid (in this case activated with NHS) and a nucleophilic amine, since its hindered and poorly nucleophilic nature allows to avoid competing reactions.

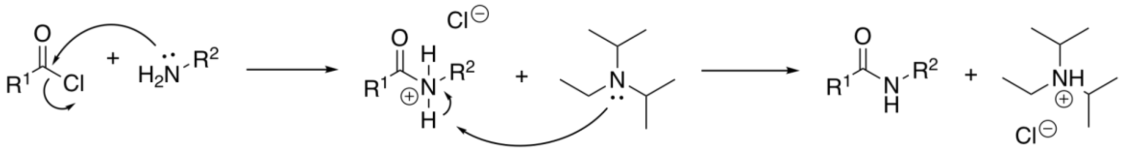

Figure 43. Generic mechanism of DIPEA in the reaction between an activated compound (acyl halide) and a primary amine.

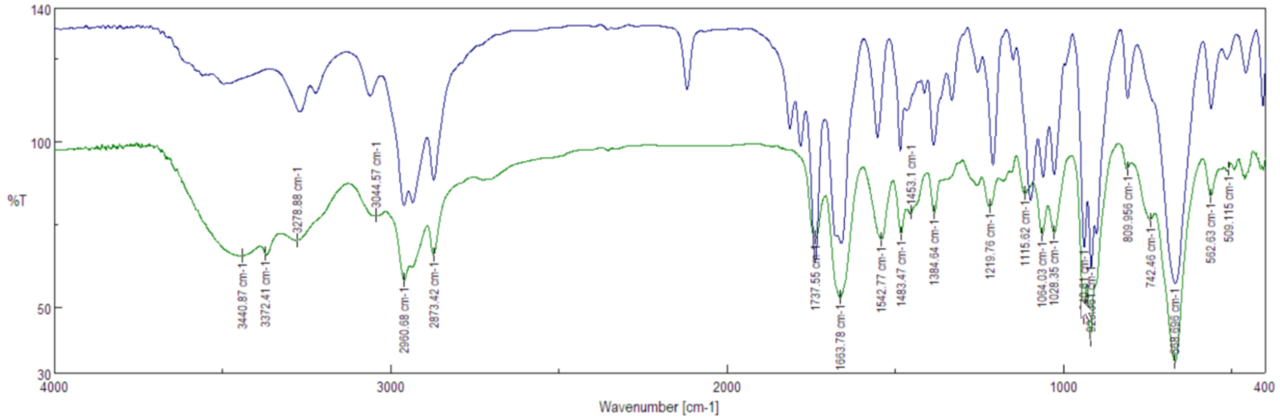

Figure 44. IR spectra of the POM-NHS (blu) and the coupling product with L-Phe (green)

In the FT-IR (KBr) spectra it is possible to distinguish the disappearance of the bands at 1816 cm^{-1} and 1784 cm^{-1}, which is typical of the POM-NHS carbonyls, and the appearance of two medium-to-low intensity new bands: one at 1663.78 cm^{-1} due to the ester carbonyl and the other at 1542 cm^{-1} due to the amide bond. The other typical peaks of the Mn-Anderson-Evans framework in the region from 1000 cm^{-1} to approximately 500 cm^{-1} are fully preserved, confirming the integrity of the POM scaffold.

The second confirmation comes from the ESI-MS (-) spectrum in acetonitrile in which there are several peaks arising from the loss of one or more TBA cations, such as the [M-TBA]$^-$ peak at m/z 2161.0 (m/z calculated: 2161.5), [M-2TBA+H]$^-$ at m/z 1919.8 (m/z calculated: 1920.0), and [M-3TBA+2H]$^-$ at 1677.7 (m/z calculated: 1679.4). The dimer is also detected as [2M-3TBA+H]$^{2-}$ at 2042.9 (m/z calculated: 2041.7) and [2M-3TBA]$^{3-}$ at 1361.8 (m/z calculated: 1360.8).

Another confirmation comes from the elemental analysis (C 40.81%, H 6.87%, N 4.83%) which coincides with the calculated values for the structure $C_{84}H_{154}MnMo_6O_{32}N_7$ (C 41.95%, H 6.45%, N 4.08%).

The ^1H NMR spectrum in CD_3CN (see appendix) further confirms the structure of the desired product since it is possible to notice the presence of the aromatic CH between 7 and 7.5 ppm, as well as the singlet at 3.6 ppm, which corresponds to the methyl ester group $-OCH_3$, belonging to the amino acid. It is also likely that the multiplet at 3.1 ppm is an overlap between TBA and the CH_2-CH protons of the amino acid. The signal at 4.6 ppm might be due to the primary (C)-H atom in the amino acid.

The UV and CD spectra were recorded for the POM-NHS, the POM – L-phenylalanine, and the free amino acid alone at corresponding concentrations, i.e., the first two were 12.5 µM, while the phenylalanine alone was at double concentration (25 µM) since every coupling product contains 2 amino acids, one on each side. The solvent of choice was acetonitrile, which showed good solubility properties.

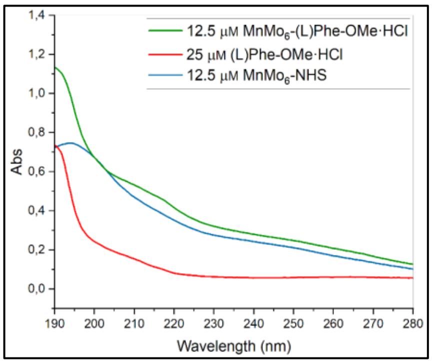

Figure 45. UV spectrum of POM $MnMo_6NHS$, $MnMo_6Phe$ (coupling product), and the single amino acid phenylalanine (Phe).

The UV spectrum of $MnMo_6$ POM – L-Phe resembles the ones of the two reagents $MnMo_6$ POM – NHS and L-phenylalanine, appearing like the overall combination of the two, and shows a significantly intense peak whose maximum falls <190 nm (ε_{190}=215200 $cm^{-1}M^{-1}$). A shoulder is visible at 218 nm (ε_{218}=73600 $cm^{-1}M^{-1}$). The amino acid alone shows the same major peak and shoulder with lower molar absorption coefficient (ε_{190}=96000 $cm^{-1}M^{-1}$ and ε_{205}=28800 $cm^{-1}M^{-1}$).

The circular dichroism analysis further confirmed that the coupling reaction was successful, as it is possible to notice that the final product has a similar trend compared with the single amino acid, which is also absent in the POM-NHS. This is mainly due to the electronic metal-oxygen transitions which are influenced by the chiral near-field induced by the appended amino acid. The positive dichroic signals are located at 196 nm ([θ]=112806 $deg*cm^2*dmol^{-1}$) and 219 nm ([θ]=42729 $deg*cm^2*dmol^{-1}$) approximately like

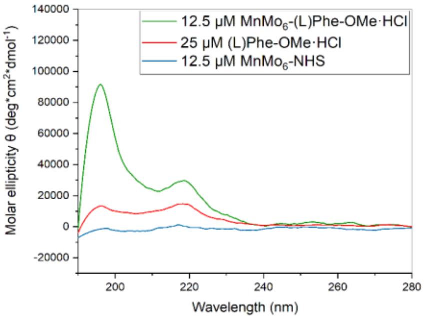

Figure 46. Molar ellipticity of POM $MnMo_6$-NHS, $MnMo_6$-Phe (coupling product), and the single amino acid phenylalanine (Phe).

the ones of phenylalanine, falling at 195 nm (([θ]=21510 deg*cm^2*dmol^{-1}) and 219 nm (([θ]=15703 deg*cm^2*dmol^{-1}).

Synthesis 6A

Synthesis of "MnMo$_6$ POM-DB" $[(C_4H_9)_4N]_3[MnMo_6O_{18}\{(OCH_2)_3CNHCO(CH_2)_2CO(C_{49}H_{68}N_{13}O_9)\}_2]$

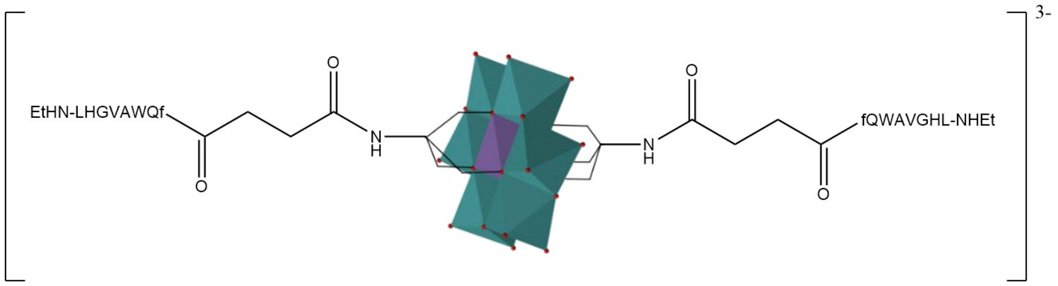

The peptide used in this synthesis is the (Demobesin-1), which is a bombesin antagonist peptide composed by 8 amino acids: H-Phe-Gln-Trp-Ala-Val-Gly-His-Leu-NH-Et, which has already been described in literature for its superior biological profile[98] and for showing a much more pronounced uptake compared to other agonists. Another benefit of using an antagonist rather than an agonist is a lower number of side effects due to its reduced physiologic activity.[99] Finally, since bombesin agonists stimulate tumor growth and angiogenesis, it is probable that the use of a GRP receptor antagonist may prevent such tumor-proliferative side effects.[100]

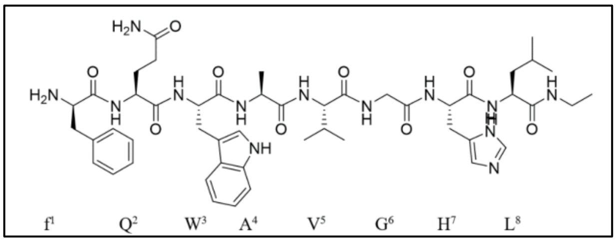

Figure 47. Structure of Demobesin-1. It is possible to notice the N-terminal side on the left where the coupling reaction occurs.

The reaction has been performed with a small excess of peptide, for the same reasons explained in the previous synthesis to avoid further purification steps. The greasy solid was purified by multiple precipitation steps in diethyl ether atmosphere. The product, which still contained absorbed DMF (see NMR data), was isolated with 84% yield.

The product was immediately characterized by ESI-MS(-) in acetonitrile and it was possible to notice the [M-3TBA+H]$^{2-}$ peak, with m/z 1643.6, compared to the theoretical value at m/z 1644. Other peaks were [M-2TBA]$^{2-}$ at m/z 1763.6, compared to the calculated m/z 1764.9, and finally [M-3TBA]$^{3-}$ seen at m/z 1095.0, compared to the calculated m/z 1095.8. No mono-substituted side products were identified. On the other hand, the unreacted peptide, which yields a minor peal at m/z 986.4 (molar mass of peptide 983.53 g/mol) disappeared after the various precipitation steps.

The FT-IR (KBr) spectrum of the product was compared to the one of the reagent (Mn-Anderson POM-NHS) showing unvaried region characteristic on the $MnMo_6$ POM structure between 1000 cm^{-1} and 500 cm^{-1}. It is possible to notice a strong band at approximately 1680 cm^{-1}, which is the confirmation of the C=O peptide bond, and the value at 1539 cm^{-1} is due to the N-H stretching. Important to notice is the disappearance of the C=O carbonyl signal which was present in the NHS groups of the reagent, and which verifies the correct progress of the reaction, at 1737 cm^{-1}.

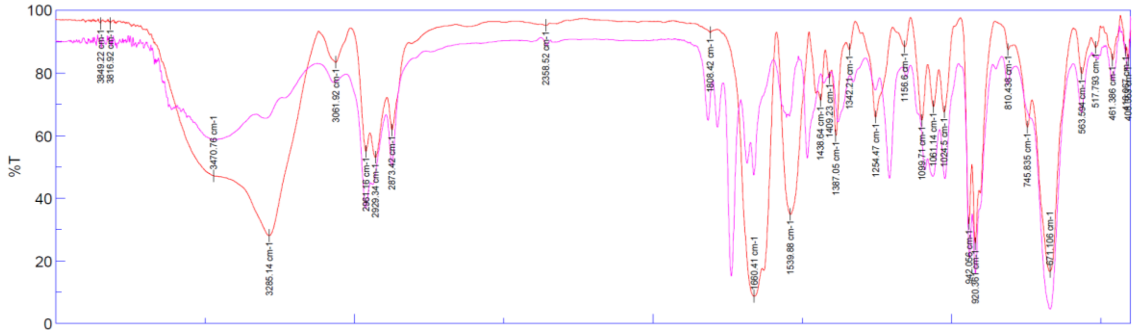

Figure 48. IR spectrum of the coupling product between $MnMo_6$ POM-NHS and Demobesin-1: $MnMo_6$ POM-DB (in red), and the initial reagent $MnMo_6$ POM-NHS (in purple). It is possible to notice the complexity caused by the 8 amino acidic residues.

The product was further characterized together with $MnMo_6$ POM-NHS and Demobesin-1 alone (this last one at double) through UV and CD in TFE/H_2O 1:10. The choice of using this solvent for all the CD analyses involving peptides and derivatives comes from its substantial lack of absorption bands in the 190-260 spectral range used for the characterization of the hybrids in this thesis. It is also the solvent of choice to solubilize both the inorganic and organic domains and allow to study the evolution of the secondary structure by varying the TFE/H_2O ratio as it will be discussed in the next syntheses.

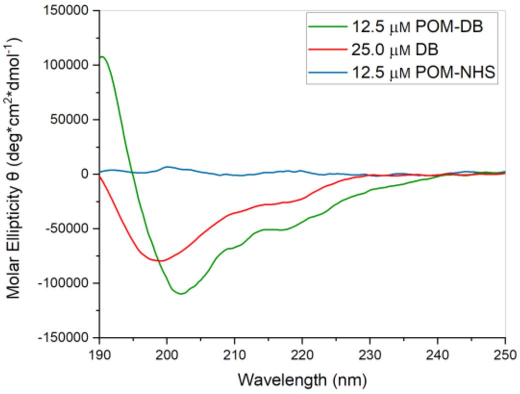

Figure 49. Molar ellipticity of MnMo$_6$ POM-NHS, MnMo$_6$ POM-DB (coupling product), and the single peptide DB (Demobesin-1) alone. Solvent: TFE/H$_2$O

The CD of the coupling product, in TFE/H$_2$O 1:10, shows a profile with positive Cotton effect, together with a series of negative "shoulders" which resembles the trend of the peptide alone. Once again it is possible to distinguish the induction of the peptide chirality to the inorganic framework. The molar ellipticity minimun of the POM-DB is located at 202 nm ([θ]=-109508 deg*cm^2*dmol^{-1}) and the one of the peptide is located at 199 nm ([θ]=-79077 deg*cm^2*dmol^{-1}). The maximum for POM-DB falls at 190.5 nm ([θ]=108404 deg*cm^2*dmol^{-1}) and the one of the peptide is < 190 nm; however the molar ellipticity value at 190 nm is [θ]=-2546 deg*cm^2*dmol^{-1}.

It is also possible to discuss the structure of the peptide, as CD is an excellent method for rapidly evaluating the secondary structure, folding and binding properties of proteins. The chains appear to have mainly a random coil secondary structure, as the trend is coherent with data found in various scientific publications. The coupling product assumes a stronger α-helix character. This is an important observation to understand the behaviour of the peptide chain during the binding to its target receptors.

Finally, the UV spectra of the coupling product and its precursors have been registered, and it appears that the MnMo$_6$ POM-DB spectrum is the sum of the two of the reagents: Demobesin-1 and MnMo$_6$ POM-NHS, which confirms the reaction outcome. The maximum of intensity for the coupling product is located at 193 nm (ε_{193}=289600 cm^{-1}M^{-1}) and a weak shoulder arising from DB absorbance can be seen in the range 215 nm (ε_{215}=120000 cm^{-1}M^{-1}) to 198 nm (ε_{193}=248000 cm^{-1}M^{-1}). The MnMo$_6$ POM-NHS shows a less intense maximum at 196 nm, while Demobsin-1 displays two main peaks at 217 nm and at < 190 nm.

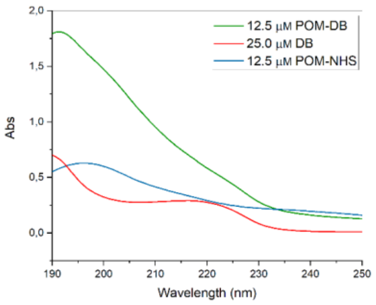

Figure 50. UV spectra of the coupling product MnMo$_6$ POM-DB and the precursors. Solvent: TFE/H$_2$O 1:10.

The CD analysis has been performed also at different TFE/H$_2$O ratios as TFE is the solvent of choice to study the evolution of the peptide secondary structure in solution and allows the evaluation of the influence of a membrane-like environment on the peptide conformation thanks to its lower polarity. It provides great solubility, and its chemical properties, such as being a strong hydrogen bond donor and poor acceptor, together with the possibility of establishing fluorous interactions, stabilize different peptide conformations as its percentage in water varies.[101] The various curves of the $MnMo_6$ POM-DB appear significantly different and more intense if compared to the ones of the Demobesin-1 alone. Indeed, a maximum of molar ellipticity is clearly recognizable at 193 nm with higher percentages of TFE. The different graphs were further processed through a secondary structure simulator, CDApps, which attempts to extrapolate the different secondary structure components using an X-ray database of proteins. The outcomes seem to indicate that the peptide alone primarily maintains a beta strand conformation at almost 40% at all the TFE/H_2O ratios, which decrease till 30% in pure TFE. The hybrid POM-peptide shows instead a preferred α-helix conformation at increasing percentages till 60% in pure TFE, except for the first ratio 1/10 TFE/H_2O which still indicates a 37% beta strand. As already reported by Cronin et al. the polyoxometalate framework proves to have a determining effect on the peptide conformation, leading to α-helix structures. It is important to note, however, that the peptide is too short to form an actual “α-helix”, and in reality, it is more appropriate to imagine it like a “pseudo α-helix” which only partially resembles the standard motif.

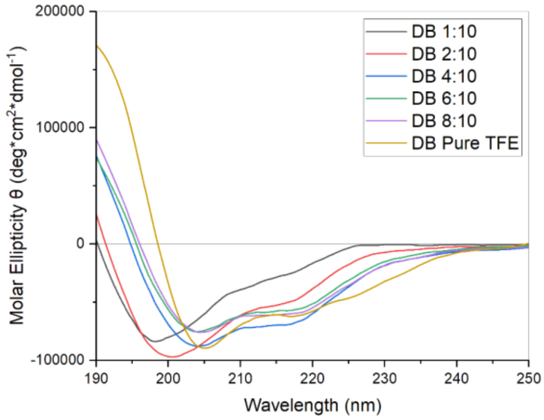

Figure 51. Molar Ellipticity of Demobesin-1 25 µM at different solvent TFE/H_2O ratio: 1:10, 2:20, 4:10, 6:10, 8:10, TFE pure.

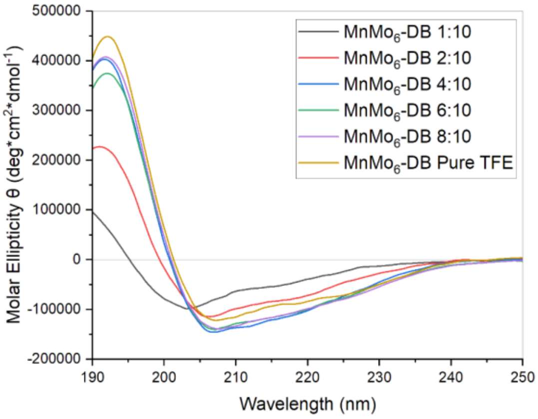

Figure 52. Molar Ellipticity of the $MnMo_6$ POM- DB 12.5 µM at different solvent TFE/H_2O ratio: 1:10, 2:20, 4:10, 6:10, 8:10, TFE pure.

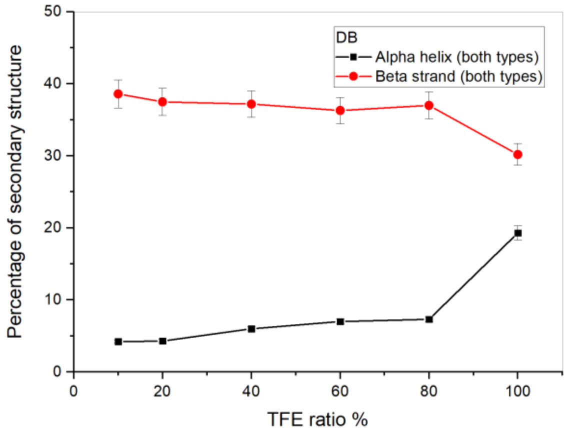

Figure 53. Percentage of α-helix and β-strand for Demobesin-1 at different TFE/H_2O percentages: 1:10, 2:20, 4:10, 6:10, 8:10, TFE pure.

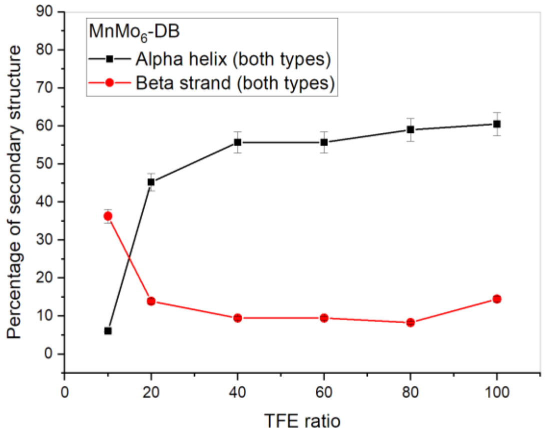

Figure 54. Percentage of α-helix and β-strand for the $MnMo_6$ POM-DB at different TFE/H_2O percentages: 1:10, 2:20, 4:10, 6:10, 8:10, TFE pure.

The hybrid has also been analyzed through two-dimensional ^1H NMR in deuterated DMSO which proved to be a good solvent for the POM-peptides, suitable for NMR analyses, and easily available compared to deuterated TFE. The correct peptide sequence has been experimentally confirmed through COSY, TOCSY and ROESY both for the peptide alone and for the final coupling product. The COSY spectrum was used to confirm the number of amino acids (NH on the x-axis and $CH_\alpha/CH_{2\alpha}$ on the y-axis), which were later on identified and labelled thanks to the overlapping between COSY and TOCSY in which the side chains of each amino acid become visible. The final peptide sequence was deduced by overlapping the previous spectra with ROESY in which it was possible to correlate the NH of an amino acid with the $CH_\alpha/CH_{2\alpha}$ of the previous amino acid.

The chemical shifts of both Demobesin-1 alone and the final coupling were compared, and it was noticed that all the values appear up-shielded in $MnMo_6$ POM-DB, which means they fall at a lower frequency, in accordance with the theoretical shielding effect of the polyoxometalate framework bearing 3 negative charges. The high influence of the POM on the peptide might be due to a folding of the organic domain over the inorganic one, which may have a negative impact on the peptide-receptor binding. Another observation is about the ROESY of the hybrid, in which a match between valine (5) and tryptophan (3) was clearly identified. A possible explanation could be a partial folding or turn in the peptide structure which, influenced by the polyoxometalate framework, allowed valine to "feel" tryptophan.

	MnMo$_6$ POM-DB			**DB**	
AA	**NH (ppm)**	**CH$_\alpha$ (ppm)**	**Rest of the chain (ppm)**	**NH (ppm)**	**CH$_\alpha$ (ppm)**
D-Phe	8.40	4.37	-CH$_{2\beta}$ 2.87 Aromatics not assigned	-	-
Gln	8.55	3.87	-CH$_{2\beta}$ (diastereotopic) 1.68, 1.74 -CH$_{2\gamma}$ 1.45 -NH$_2$ not observed	8.55	4.33
Trp	7.93	4.45	-CH$_{2\beta}$ (diastereotopic) 3.06, 3.20 Aromatics not assigned	8.30	4.56
Ala	7.74	4.32	-CH$_3$ 1.25	8.25	4.41
Val	7.52	4.09	-CH$_\beta$ 2.00 (-CH$_{3\gamma}$)$_2$ 0.87	7.77	4.17
Gly	8.19	-CH$_{2\alpha}$ 3.72	/	8.23	-CH$_{2\alpha}$ 3.72, 3.79
His	8.00	4.54	-CH$_{2\beta}$ 3.02 -NH aromatics not observed -CH aromatics not assigned	8.13	4.61
Leu	7.96	4.18	-CH$_{2\beta}$ 1.46	8.09	4.20

			$-CH_{\gamma}$ 0.83 $(-CH_{3\delta})_2$ not observed		
NHEt	8.00	$-CH_{2\alpha}$ 3.08	$-CH_{3\beta}$ 1.00	8.04	$-CH_{2\alpha}$ 3.08

Table 3. Chemical shift of each amino acid in the Demobesin-1 alone and linked to the POM. Additionally, the side chains of each amino acid in the hybrid were identified.

SYNTHESIS 7A:

Synthesis of "$MnMo_6$ POM-EEEEβAla-fQWAVGHL-NHEt"

$[(C_4H_9)_4N]_3[MnMo_6O_{18}\{(OCH_2)_3CNHCO(CH_2)_2CO(C_{72}H_{101}N_{18}O_{22})\}_2]$

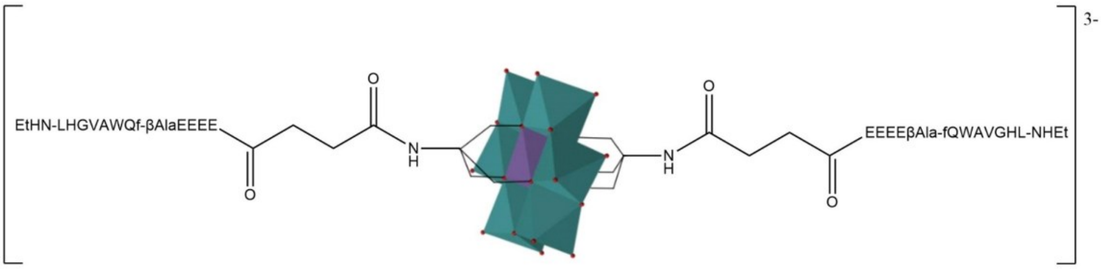

This coupling reaction was performed in the same conditions as the previous ones, in detail the Mn-Anderson-Evans POM-NHS reacted with 2.3 times excess of EEEEβAla-fQWAVGHL-NHEt, which is the Demobesin-1, with 4 glutamic acids as spacers, which is aimed at (i) increasing the distance between POM and DB, and (ii) creating a repulsion between the negatively charged polyoxometalate framework and the peptide chains. This is expected to avoid strong interactions with the polyoxometalate, which would result in unwanted folding, preventing the peptide from binding with the corresponding receptor.

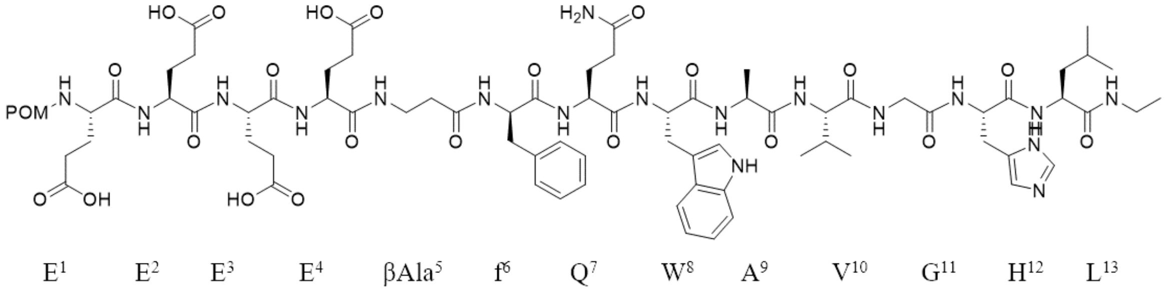

Figure 55. Structure of the peptide used in this synthesis: EEEEβAla-fQWAVGHL-NHEt

The coupling reaction was performed, in the presence of DIPEA as the hindered base, in approximately 24 hours at room temperature. As in the previous synthesis, the final solid was greasy and we were unable to obtain crystals. Nevertheless, the precipitation form the DMF solution, in a diethyl ether atmosphere, was faster. The reaction yield (95%) was much higher compared to the previous coupling reactions, and all the analyses performed were in agreement with a good purity. The ESI-MS (-) analysis in acetonitrile shows a peak at m/z 1487, which can be the $[M\text{-}3TBA]^{3-}$ species (m/z 1487.26). There are also other possible fragmentations such as m/z 1503.4 for $[M\text{-}3TBA\text{-}2H+2Na]^{3-}$, whose calculated value is m/z 1501.86 and 1574.5 for $[M\text{-}2TBA\text{-}2H+Na]^{3-}$ which corresponds to the theoretical m/z 1575.0. We were unable to assign the most prominent signal at 1454.0 m/z which carries a 2- negative charge according to the deconvolution performed by the ESI-MS software; however, a previous attempt carried out at the Dept. of Chemical Science in University of Padua lead to the same results, and other analyses seem to confirm the correct synthesis. No mono-functionalized product or unreacted precursors were found. The FT-IR (KBr) spectrum confirms the formation of the new peptide bond (1656 cm^{-1}) with full retention of POM signals <1000 cm^{-1}. The UV and CD spectra were recorded for the coupling product together with POM-NHS, and DB-βAlaEEEE alone at double concentration. The solvent used was TFE/H_2O 1:10.

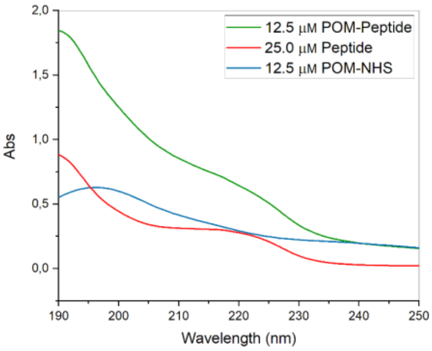

Figure 56. UV spectra of the final product POM-EEEEβAlaDB and the two reagents: POM-NHS, and the single peptide. The solvent is TFE-H_2O 2:10.

The absorbance spectrum shows a maximum at <190 nm (ε_{190}=289600 $cm^{-1}M^{-1}$). A shoulder at 218 nm (ε_{218}=112000 $cm^{-1}M^{-1}$) can also be noticed and the same pattern can be distinguished for the peptide which has a two peak profile: one which falls at less than 190 nm (ε_{190}=70400 $cm^{-1}M^{-1}$) and the other at approximately 216 nm (ε_{216}=24000 $cm^{-1}M^{-1}$). The product and the reagents were also independently analyzed through CD spectroscopy at tied concentrations (double concentration for the peptide since two molecules of it bind to each polyoxometalate) and it is noticeable that the structure of the peptide alone is mostly β-strand, before and after the reaction. Anyways, the peptide chains chirality has a strong impact on the polyoxometalate framework, whose transitions modulate the intensity of the previous, enhancing the positive Cotton effect. The minimun of the POM-EEEEβAlaDB is located at 205 nm ([θ]=-269470 deg*cm^2*dmol^{-1}) and the one of the peptide DB-βAlaEEEE is located at 203 nm ([θ]=-82216 deg*cm^2*dmol^{-1}). The maximum falls under at <190 nm for both POM-EEEEβAlaDB ([θ]=404754 deg*cm^2*dmol^{-1} at 190 nm) and DB-βAlaEEEE alone ([θ]=79088 deg*cm^2*dmol^{-1} at 190 nm).

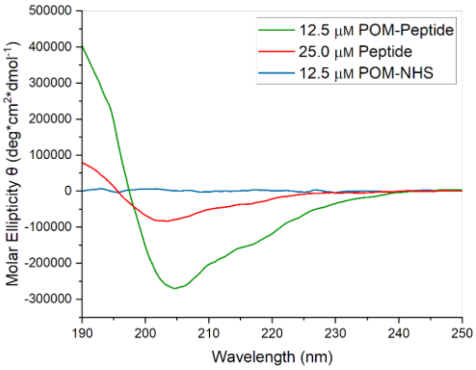

Figure 57. Molar Ellipticity graphs of the final product POM-EEEEβAlaDB and the two reagents POM-NHS and the single peptide. The solvent is TFE-H$_2$O 2:10.

Further CD analyses were performed for both the peptide DB-βAlaEEEE and the final product POM- EEEEβAlaDB at different TFE/H$_2$O solvent ratios, in particular 1:10,

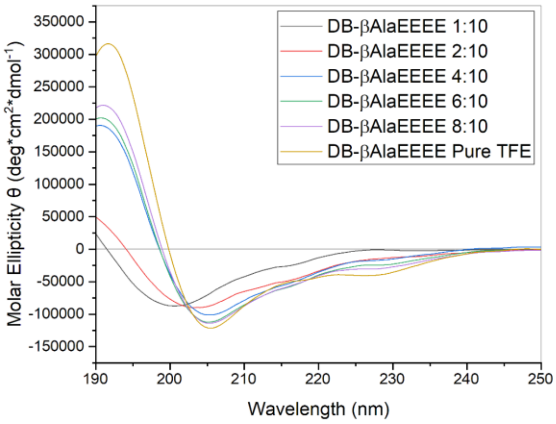

Figure 58. Molar Ellipticity of the peptide DB-βAlaEEEE 25 µM at different solvent TFE/H$_2$O ratio: 1:10, 2:20, 4:10, 6:10, 8:10, TFE pure.

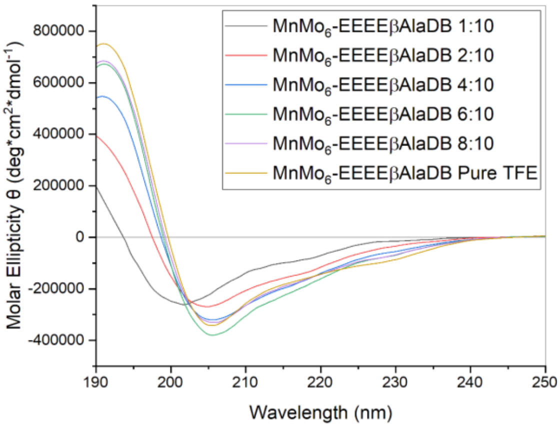

Figure 59. Molar Ellipticity of the POM-EEEEβAlaDB 12.5 µM at different solvent TFE/H$_2$O ratio: 1:10, 2:20, 4:10, 6:10, 8:10, TFE pure

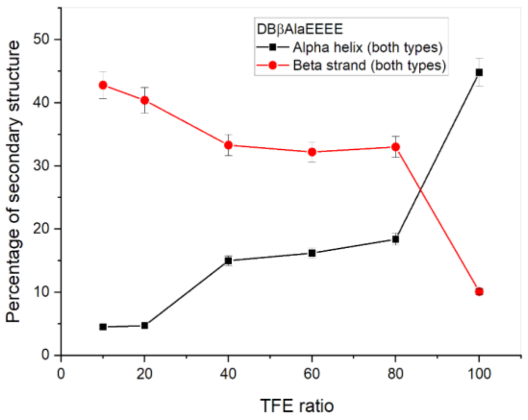

Figure 60. Percentage of α-helix and β-strand for the peptide DB-βAlaEEEE at different TFE/H$_2$O percentages: 1:10, 2:20, 4:10, 6:10, 8:10, TFE pure.

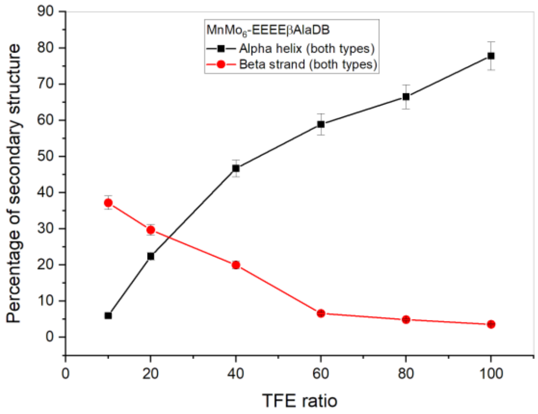

Figure 61. Percentage of α-helix and β-strand for the POM-EEEEβAlaDB at different TFE/H$_2$O percentages: 1:10, 2:20, 4:10, 6:10, 8:10, TFE pure.

2:20, 4:10, 6:10, 8:10, and pure TFE to study the impact of the polyoxometalate framework on the stability of the secondary structure of the peptide in a less hydrophilic environment. The overall behavior is similar for both samples. The presence of an isodichroic point in each graph confirms the existence of a conformational equilibrium between β-strand and α-helix in solution.

The CD spectra were later on processed through CDApps to provide an approximate percentage of α-helix and β-strand secondary structures for each TFE/H_2O ratio. While the peptide alone primarily maintains a beta strand structure for all the TFE/H_2O ratios except pure TFE (in which there is a higher percentage of α-helix), the POM-peptide appears in beta strand only at low TFE concentration (<1:10 and 2:10 TFE/H_2O), with an immediate overtaking for the "pseudo-α-helix" structure.

The 2D ^{1}H NMR analysis (COSY, TOCSY and ROESY) of both the peptide and the POM-peptide have been recorded in deuterated DMSO. In the ROESY of POM-peptide there seems to be a match between the amino acids His 12 and Gln 7, which would prove a folding of the peptide over itself; whereas no such match is recognizable in the ROESY of the peptide alone. This is in agreement with a different impact of the POM on the modified peptide.

The absence of doubled signals proves that the hybrid is symmetric, and the ROESY spectrum has been carefully analyzed to verify that the peptide chain has remained intact during the reaction process. The chemical shifts of DB-βAlaEEEE alone and POM-EEEEβAlaDB are generally comparable, if not identical, proving that there are no effects from the negatively charged POM on the peptide (which would have otherwise been noticeable from up-shifts or down-shifts). Only the chemical shifts of the spacer -EEEE- was affected, in particular up-shifted, probably because of the proximity with the newly formed bond (with the POM). No conformational effects due to the condensation or folding between the POM and peptide were encountered either, therefore the introduction of the spacer is determining.

	POM-EEEEβAlaDB			**DBβAlaEEEE**	
AA	**NH (ppm)**	**CH_α (ppm)**	**Rest of the chain (ppm)**	**NH (ppm)**	**CH_α (ppm)**
Glu^1	8.13	4.20	$-CH_{2\beta}$ 2.26	-	-

			$-CH_{2\gamma}$ (diastereotopic) 1.73, 1.85		
Glu^2	8.08	4.17	$-CH_{2\beta}$ 2.27 $-CH_{2\gamma}$ (diastereotopic) 1.77, 1.89	8.62	4.35
Glu^3	7.93	4.12	$-CH_{2\beta}$ 2.26 $-CH_{2\gamma}$ (diastereotopic) 1.76, 1.90	8.21	4.25
Glu^4	7.86	4.14	$-CH_{2\beta}$ 2.20 $-CH_{2\gamma}$ (diastereotopic) 1.73, 1.84	8.01	4.15
bAla	7.82	$-CH_{2\alpha}$ 3.18	$-CH_{2\beta}$ 2.27	7.93	$-CH_{2\alpha}$ 3.11, 3.21
D-Phe	8.27	4.44	$-CH_{2\beta}$ (diastereotopic) 2.94, 2.78 Aromatici non osservati	8.27	4.45
Gln	8.34	4.09	$-CH_{2\beta}$ (diastereotopic) 1.89, 1.78 $-CH_{2\gamma}$ 1.59	8.36	4.10
Trp	7.96	4.38	$-CH_{2\beta}$ (diastereotopic) 2.72, 2.88 Aromatics not assigned	8.01	4.48
Ala	7.97	4.40	$-CH_3$ 1.21	7.97	4.37
Val	7.66	4.18	$-CH_{\beta}$ 2.01 $(-CH_{3\gamma})_2$ 0.85	7.61	4.14
Gly	8.22	$-CH_{2\alpha}$ 3.73	/	8.24	$-CH_{2\alpha}$ 3.70, 3.77
	8.01	4.46	$-CH_{2\beta}$ 2.91	8.08	4.61

His			-NH aromatics not observed -CH aromatics not assigned		
Leu	7.93	4.12	-CH$_{2\beta}$ 1.48 -CH$_{\gamma}$ 0.82 (-CH$_{3\delta}$)$_2$ non observed	8.07	4.20
NHEt	8.12	-CH$_{2\alpha}$ 3.08	-CH$_{3\beta}$ 1.00	8.04	-CH$_{2\alpha}$ 3.08

Table 4. COSY and TOCSY signals for the amino acids composing the POM-EEEEβAlaDB and the peptide alone.

SYNTHESIS 8A:

Synthesis of "MnMo$_6$ POM-TtdsDB"

$[(C_4H_9)_4N]_3[MnMo_6O_{18}\{(OCH_2)_3CNHCO(CH_2)_2CO(C_{49}H_{68}N_{13}O_9)\}_2]$

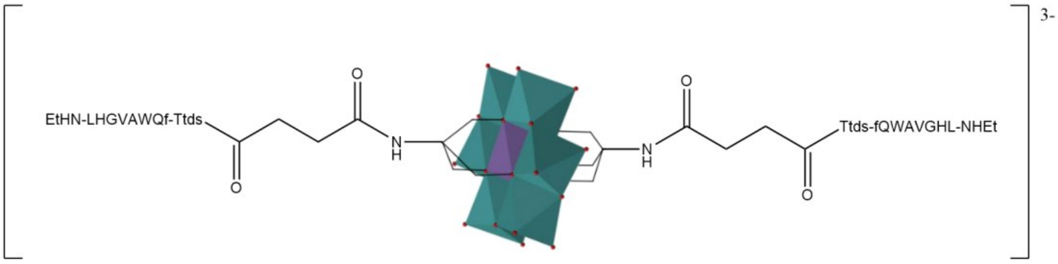

The reaction has been performed in the same conditions as the previous couplings. The peptide used in this case is the same as the previous reactions, but once again it was attempted to use a different spacer to study its influence on distancing the target sequence from the polyoxometalate. The peptide sequence is H-Ttds-(D-)Phe-Gln-Trp-(β-)Ala-Val-Gly-His-Leu-NHEt.

The spacer consists in a small PEG-like chain, the Ttds (trioxatridecan-succinamic acid) which improves water solubility, while inducing a better overall stability.

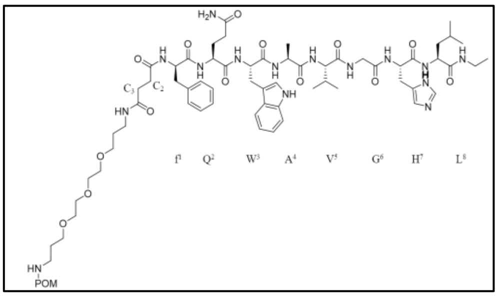

Figure 62. Amino acid sequence of the DB-Ttds peptide used in this coupling reaction.

The product, obtained with 90% yield, has been analyzed by FT-IR, which shows all the expected signal. ESI-MS(-) was performed in acetonitrile and all the three major peaks have been attributed. In detail the $[M\text{-}2TBA]^{2-}$ fragmentation was seen at m/z 2067.5, compared to the theoretical m/z 2067 value. The $[M\text{-}3TBA+H]^{2-}$ fragmentation was noticed at m/z 1947.8, compared to a calculated m/z 1946. Finally, the $[M\text{-}3TBA]^{3-}$ fragmentation was seen at m/z 1299.6, compared to 1297. No mono-functionalized products or unreacted precursors were noticed.

The POM-TtdsDB has been analyzed through UV and CD and compared with the POM-NHS and DBTtds spectra at the corresponding concentrations in TFE/H_2O 1:10.

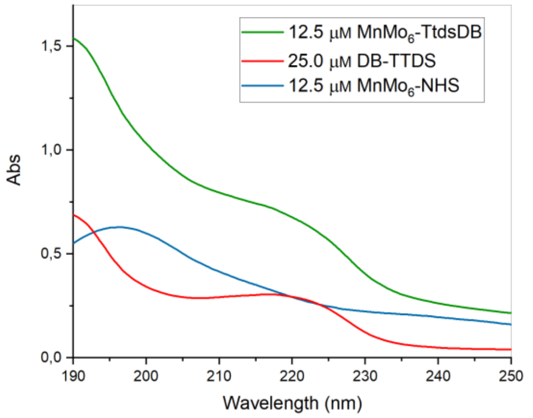

Figure 63. UV spectra of the product MnMo$_6$-TtdsDB and the two (organic and inorganic) precursors. The solvent used was TFE/H_2O 1:10.

Like in the previous syntheses, the UV spectrum of the coupling product resembles the one of the two reagents together, especially the peptide one, since they both have a two-peak profile. The maximum for POM-TtdsDB is located at less than <190 nm (ε_{190}=244800 cm^{-1}M^{-1}) and a shoulder is visible at 217 nm (ε_{217}=115200 cm^{-1}M^{-1}) and similar wavelength values are encountered for the DB-Ttds (ε_{190}=55200 cm^{-1}M^{-1} and ε_{217}=24000 cm^{-1}M^{-1}).

The CD analysis has been performed for both the peptide DB-TTDS and the final product POM-TtdsDB at different TFE/H_2O solvent ratios, in particular 1:10, 2:20, 4:10, 6:10, 8:10, and pure TFE to study the impact of the polyoxometalate framework on the peptide secondary structure. The first interesting difference is that at ratio 6:10, 8:10 and 10:10 (pure TFE) the polyoxometalate stabilized the same peptide structure, whereas this does not occur with the single peptide which shows identical molar ellipticity curves at 4:10 6:10 and 8:10 ratios but not in pure TFE. In this case as well it is possible to analyze an isodichroic point which indicates a local two-state (α-helix, β-strand) population.

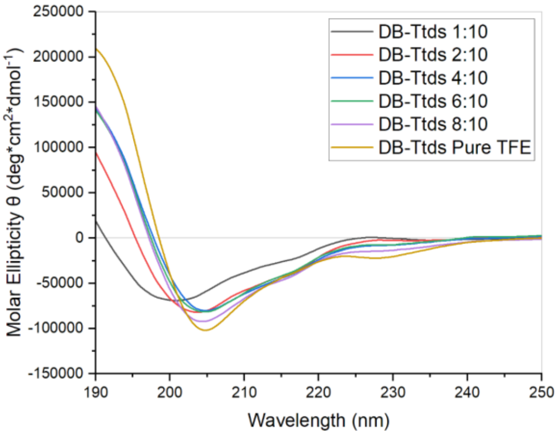

Figure 64. Molar ellipticity of 25µM DB-Ttds at different ratio of TFE/Water: 1:10, 2:20, 4:10, 6:10, 8:10, and pure TFE.

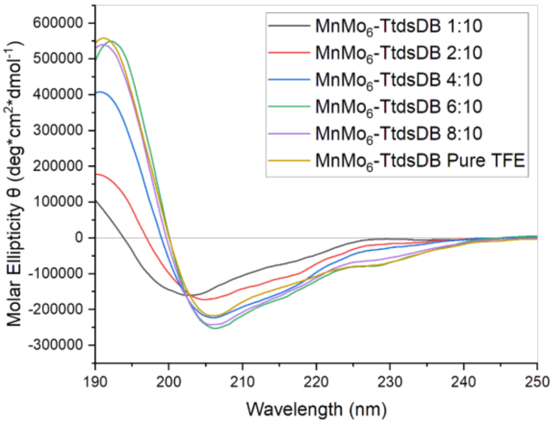

Figure 65. Molar ellipticity of 12.5 µM $MnMo_6$-TtdsDB at different ratio of TFE/Water: 1:10, 2:20, 4:10, 6:10, 8:10, and pure TFE.

The molar ellipticity minimum of the curve for POM-TtdsDB at 1:10 TFE/H_2O ratio is located at 203 nm ([θ]=-160978 deg*cm^2*dmol^{-1}) and the one of the peptide DB-βAlaEEEE is located at 203 nm, with a lower intensity ([θ]=-68506 deg*cm^2*dmol^{-1}). The maximum signal for POM-TtdsDB falls under 190 nm ([θ]=107838 deg*cm^2*dmol^{-1} at 190 nm), while the molar ellipticity at 190 nm for DBTtds alone is [θ]=14006 deg*cm^2*dmol^{-1}.

The CD spectra were elaborated to extrapolate the percentage of α-helix and β-strand for each TFE/H2O ratio. With respect to the former case, the peptide appears to maintain the beta strand structure for all the TFE/H_2O ratios, while the POM-peptide has a stronger tendency to form the helix.

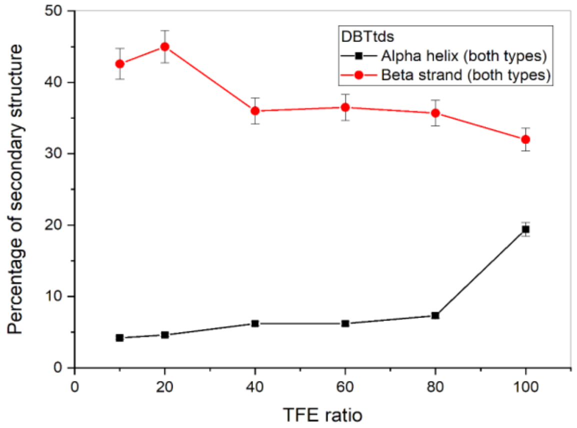

Figure 66. Percentage of α-helix and β-strand for the peptide DB-Ttds at different TFE/H_2O percentages: 1:10, 2:20, 4:10, 6:10, 8:10, TFE pure.

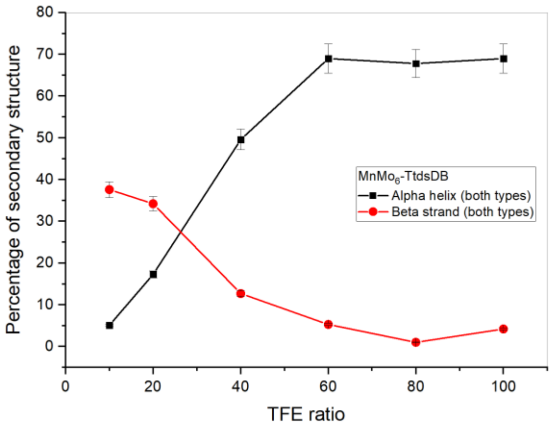

Figure 67. Percentage of α-helix and β-strand for the POM-peptide DB-Ttds at different TFE/H_2O percentages: 1:10, 2:20, 4:10, 6:10, 8:10, TFE pure.

The 2D ^{1}H NMR spectrum (COSY, TOCSY, ROESY) appears more complex compared to the one of POM-EEEEβAlaDB; however, no ROESY signals which might cause to think about a structure folding are visible. No meaningful influence by the polyoxometalate was encountered, besides for the last 2 amino acids in the chain (leu and his) seems to experience a higher chemical shift variation, up-shifts, which means there is still some interaction between the POM and peptide, however the values are average 0,10 δ shifted, which is a very low value compared to the POM-DB alone in which several signals were heavily influenced.

The absence of signals indicating an α-helix-like peptide folding is due to the different solvent used for the 2D NMR (deuterated DMSO) compared to trifluoroethanol which was used for the CD.

Another interesting observation is about the peptides. More in detail, the signals of the single peptide DB-Ttds remain almost identical to DBβAlaEEEE except the first few amino acids because of the influence of the negatively charged spacer -EEEE-, compared to the neutral Ttds.

	$MnMo_6$-TtdsDB			**DBTtds**	
AA	**NH (ppm)**	**CH_α (ppm)**	**Rest of the chain (ppm)**	**NH (ppm)**	**CH_α (ppm)**
D-Phe	8.26	4.39	$-CH_{2\beta}$ (diastereotopic) 2.78, 2.94 Aromatics not observed	8.25	4.41
Gln	8.33	4.06	$-CH_{2\beta}$ (diastereotopic) 1.78, 1.89 $-CH_{2\gamma}$ 1.59	8.34	4.07
Trp	7.97	4.47	$-CH_{2\beta}$ (diastereotopic) 3.00, 3.17 Aromatics not assigned	7.98	4.46
Ala	7.91	4.35	$-CH_3$ 1.21	7.90	4.35
Val	7.64	4.16	$-CH_\beta$ 2.00 $(-CH_{3\gamma})_2$ 0.84	7.61	4.13
Gly	8.21	$-CH_{2\alpha}$ 3.73	/	8.22	$-CH_{2\alpha}$ 3.70, 3.76
His	8.02	4.46	$-CH_{2\beta}$ 2.91	8.08	4.60

			-NH aromatic not observed -CH aromatics not assigned		
Leu	7.94	4.15	$-CH_{2\beta}$ 1.48 $-CH_{\gamma}$ 0.81 $(-CH_{3\delta})_2$ not observed	8.06	4.20
NH-Ttds	7.79	$-CH_{2\alpha}$ 3.03	$-CH_{2\beta}$ 1.58 $-CH_{2\gamma}$ 3.35	7.79	$-CH_{2\alpha}$ 3.03
NHEt	8.11	$-CH_{2\alpha}$ 3.07	$-CH_{3\beta}$ 1.00	8.02	$-CH_{2\alpha}$ 3.06

Table 6. Chemical shift of each amino acid in the DB-Ttds alone and linked to the POM. Additionally, the side chains of each amino acid in the hybrid were identified.

SYNTHESIS 9A:

Synthesis of "MnMo$_6$-c(RGDfK)"

$[(C_4H_9)_4N]_3[MnMo_6O_{18}\{(OCH_2)_3CNHCO(CH_2)_2CO(C_{27}H_{40}N_9O_7)\}_2]$

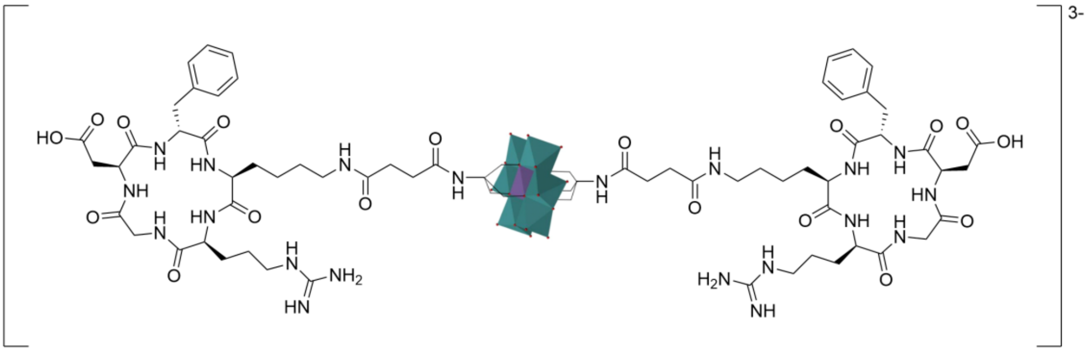

This synthesis has been performed with the cyclic peptide c(RGDfK), containing the RGD binding sequence found in the extracellular matrix. The reason why a cyclic pentapeptide was used instead of a linear one is that previous literature data[102] proved that cyclic RGD peptides had a more stable configuration in binding to integrins $\alpha_v\beta_3$, which depended on the higher binding energy

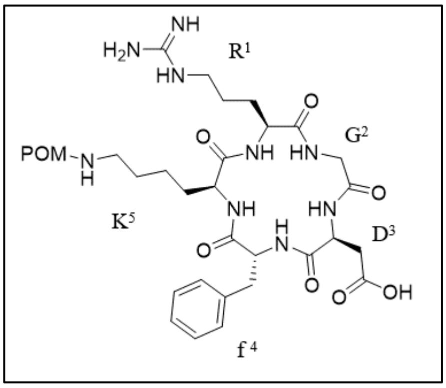

Figure 68. The cyclic peptide c(RGDfK) used in this coupling reaction.

and higher static electrical energy, especially in the interaction between AspRGD-MIDAS (in which MIDAS is a common motif characteristic of integrins). As opposed, linear RGD-containing peptides easily form hydrogen bonds because of their flexibility, which negatively impact the ability to bind integrin $\alpha_v\beta_3$ accurately. Another consideration is about their stability in vivo, since in plasma there are specific enzymes such as peptidase and protease which can easily degrade linear peptides. The insertion of non-natural or D-amino acids (D-phenylalanine for the peptide in this synthesis), as well as the synthesis of a cyclic structure contributes to their longer life in plasma. The cyclic peptide in this reaction has been synthesized without a spacer since the lateral chain of Lys, which is the fifth amino acid used to close the cycle, already works both as a small spacer and as site for grafting.

The reaction followed the same mechanism and conditions as the previous ones, with a yield of 76%. The final solid was colored light orange and appeared as a dry powder, which did not seem to include solvent residues as the previous non-cyclic peptides. The product has been characterized through ESI-MS(-) and two main fragmentations were identified: the first was m/z 1386 which was assigned to $[M\text{-}2TBA]^{2-}$ (m/z 1384.4) and secondly m/z 1261.9, which was coherent with $[M\text{-}3TBA+H]^{+}$ (m/z 1263.6). The IR spectrum of the $MnMo_6$-c(RGDfK) shows the same signals as the previous syntheses which further confirms the successful outcome of the reaction without modifying the inorganic framework.

The UV spectra show a similar trend compared to the previous syntheses. The polyoxometalate-c(RGDfK) hybrid displays a peak at maximum falling under 190 nm (ε_{190}=241600 $cm^{-1}M^{-1}$) and a shoulder at 214 nm (ε_{214}=110400 $cm^{-1}M^{-1}$). The two same features are visible also for the c(RGDfK) peptide but at a lower absorbance: a maximum falling under 190 nm (ε_{190}=63200 $cm^{-1}M^{-1}$) and a shoulder at approximately

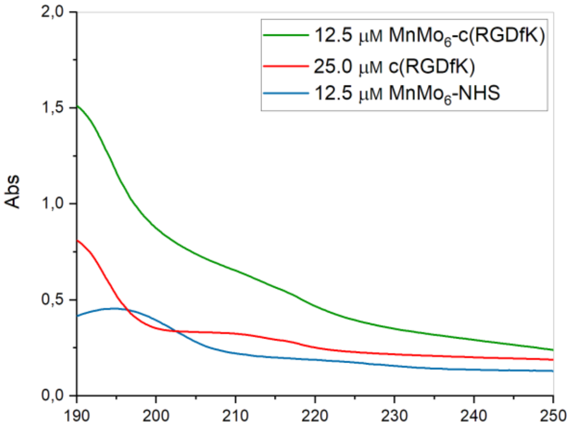

Figure 69. UV absorption spectra of the Mn-Anderson-RGD hybrid, the peptide alone and Mn-Anderson NHS.

217 nm (ε_{217}=83200 $cm^{-1}M^{-1}$). No particular differences were identified compared to the previously analyzed spectra.

The molar ellipticity trends at different TFE/H_2O ratios for the $MnMo_6$-c(RGDfK) and the cyclic peptide alone appear generally comparable in the shape, meaning that no major changes of conformation can be identified. The higher the TFE concentration, the higher molar ellipticity the curves in the graphs fall. The minimum for $MnMo_6$-c(RGDfK) in pure TFE falls at 206 nm ([θ]=-82397 deg*cm^2*$dmol^{-1}$), while the same value in TFE/H_2O 1:10 (TFE 10%) at approximately the same wavelength is [θ]=-162564 deg*cm^2*$dmol^{-1}$. The same trend can be found for the peptide alone in pure TFE. It is important to note that the maximum and minimum values for the final hybrid are approximately 4 times more intense than the ones of c(RGDfK) alone, as a confirmation of the influence of a chiral center on the polyoxometalate metal=oxygen transitions which also become chiral.

Considering that the peptide is cyclic and no major conformation changes can occur, it was decided not to perform any further secondary structure simulation with CDApp, considering also the limitations caused by the secondary structure database SP43 (SP stands for soluble protein, and the following number is the number of reference proteins N_{REF}), which would not be reliable on a cyclic peptide.

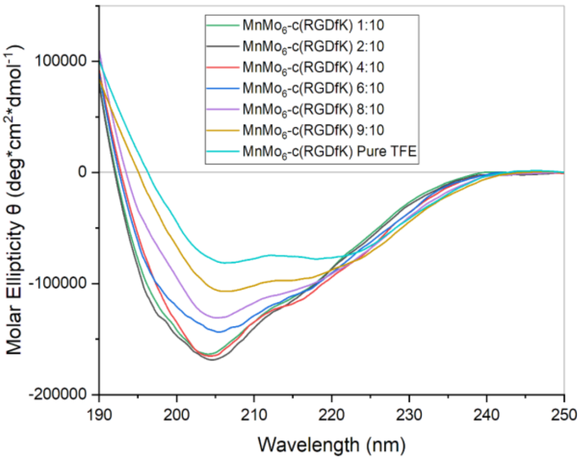

Figure 70. Molar ellipticity trends for $MnMo_6$-c(RGDfK) at different TFE/H_2O ratios: 1:10, 2:10, 4:10, 6:10, 8:10, 9:10, pure TFE.

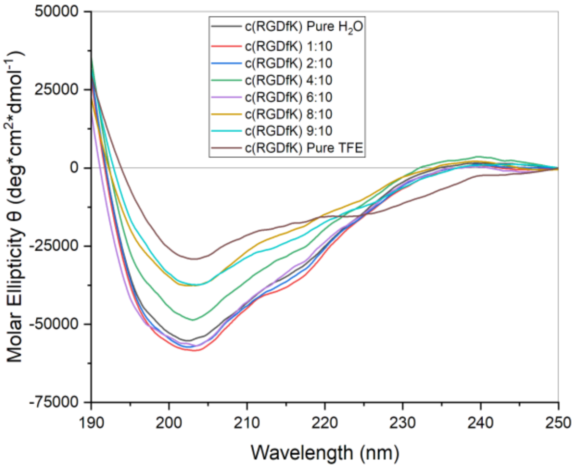

Figure 71. Molar ellipticity trends for c(RGDfK) at different TFE/H_2O ratios: pure water, 1:10, 2:10, 4:10, 6:10, 8:10, 9:10, pure TFE.

The hybrid has been analyzed through COSY, TOCSY and ROESY 2D NMR to confirm the peptide sequence and analyze the impact of the inorganic framework. While the signals due to some amino acids have similar values of chemical shifts and are slightly shielded, others like arginine have been deeply influenced, being up-shielded of 1.2 ppm. A possible explanation comes from the structure of the side chain of this amino acid, which is probably long enough to interact (together with a structure folding) with the polyoxometalate framework. The disappearance of the signal due to the NH_3^+ of lysin can be considered a proof of the formation of the new POM-peptide bond. The sequence has been confirmed through ROESY even though no coupling signals due to arginine with other amino acids were identified.

	MnMo$_6$-c(RGDfK)			**c(RGDfK)**	
AA	**NH (ppm)**	**CH$_\alpha$ (ppm)**	**Rest of the chain (ppm)**	**NH (ppm)**	**CH$_\alpha$ (ppm)**
Arg	7.81	2.97	-CH$_{2\gamma}$ 1.33 -CH$_{2\beta}$ 1.11	7.62	4.16
δ-Arg	-	-	-	7.58	-CH$_\delta$ 3.09
NH_3^+ Arg	8.21	3.28	/	8.48	3.25 (?)
D-Phe	7.83	4.55	-CH$_{2\beta}$ (diastereotopic) 2.72, 3.09 Aromatics not assigned	8.08	4.42
Gly	8.21	-CH$_{2\alpha}$ 4.10	/	8.48	-CH$_{2\alpha}$ 4.05
Asp	8.11	4.43	-CH$_{2\beta}$ 2.51	8.10	4.64
Lys	8.07	4.07	-CH$_{2\beta}$ (diastereotopic) 1.47, 1.58 -CH$_{2\gamma}$ 1.33 -CH$_{2\delta}$ 1.10	8.09	3.95
NH_3^+ Lys	-	-	-	7.69	-CH$_{2\varepsilon}$ 2.67

Table 7. Chemical shift of each amino acid in the c(RGDfK) alone and linked to the POM. Additionally, the side chains of each amino acid in the peptide linked to the POM were identified.

Lindqvist type polyoxovanadates (B)

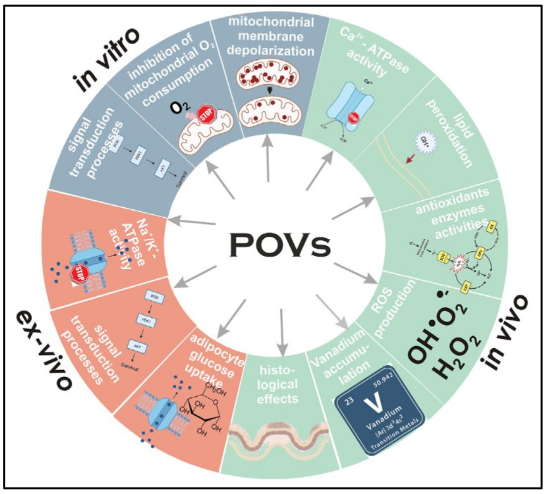

Figure 72. A scheme illustrating some biological processed affected by polyoxovanadates,

Polyoxovanadates have recently been considered a "universal biological key" to potentially unlock many processes: from influencing enzymes and pumps activity, to affecting signal transduction, to inhibition of mitochondria respiration and ATP production. While, like previously said, the first studies on anticancer activity of polyoxotungstates and polyoxomolybdates were described in 1965, the first polyoxovanadate report was published in 2009. [93] The idea of hybrids also influenced the studies on these chemical species, as they were already seen as good potential antitumoral drug. The recent studies in which the hybrids were tested both in vitro, in vivo, and ex-vivo attracted even more researchers enlightened by these compounds. What they lack is still a structural tuning to ensure appropriate selectivity on specific human targets.

Linqvist vanadates and Anderson-Evans molybdates share two common features: a small number of addenda metal ions (6 Mo or V) and reactivity towards trialkoxy derivatives, to yield symmetric bis-conjugates. The procedure to perform coupling reactions between polyoxometalates of vanadium and peptides follows an analogous procedure of the Mn-Anderson Evans POMs. The procedure requires once again the generation of an activated form consisting in the POM bearing a reactive NHS moiety, through various synthetic steps which start from inorganic $NaVO_3$, $(C_4H_9)_4NBr$, $(HOCH_2)_3CCH_2OH$ and HCl. The pentaerythritol was used instead of the Tris. The former contains a -CH_2-OH linked to the quaternary carbon, whereas the latter holds a -NH_2.

The procedure follows various reaction steps which I have performed for my thesis and are schematized as follows. In all these reactions the countercation is TBA: $[(C_4H_9)_4N]^+$.

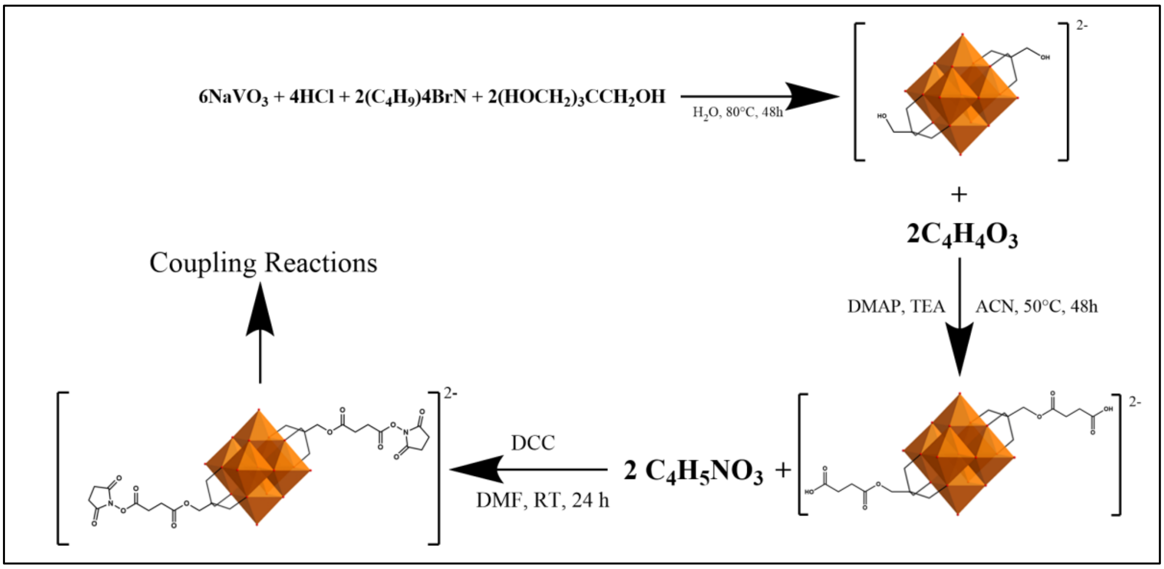

Figure 73. Various reaction steps in order to synthesize V_6 -O – NHS. The counterions and byproducts have intentionally been omitted to avoid further confusion.

The first reaction consists in the synthesis of the (OH)-functionalized polyoxovanadate starting from inorganic $NaVO_3$, $C_{16}H_{36}BrN$, stoichiometric HCl and $(HOCH_2)_3CCH_2OH$. The second step allows further functionalization with succinic anhydride to generate V_6-O-succinate, and the final step, which is the reaction with n-hydroxysuccinimide (NHS) in the presence of dicyclohexylcarbodiimide (DCC) finally generates V_6-O-NHS. In this case, the bis-functionalization with pentaerythritol occurs in the first reaction step, being required for the stabilization of the V_6-POM under harsher reaction conditions compared to the Mn-Anderson Evans polyoxomolybdate.

For this synthesis as well, only the newly relevant species will be thoroughly discussed and analyzed, and in this case also the V_6O-NHS species appears new in scientific literature, therefore my work of characterization will start with this species. The following reactions will be analogue to the ones in the previous section for polyoxomolydates: the coupling with amino acid phenylalanine, the peptides Demobesin-1, the analogues with different spacers: DB-βAlaEEEE and DB-Ttds, and RGD.

Synthesis 4B

“V_6-O-NHS” - $[(C_4H_9)_4N]_2[V_6O_{13}\{(OCH_2)_3CCH_2OOCCH_2CH_2CO(C_4H_4NO_3)\}_2]$

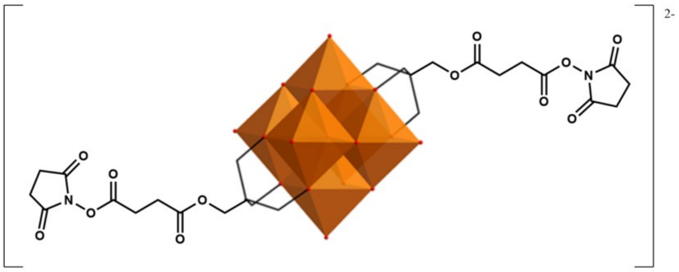

To prepare the activated form of the polyoxometalate V_6-OH, which was used for the coupling reactions shown in the next sections, the starting reagent is the V_6-O- bis substituted succinate, which reacts with an excess of n-hydroxysuccinimide and N,N'-Dicyclohexylcarbodiimide to form the desired bis substituted product. The reaction mechanism involves the production of the intermediate O-acylisourea by DCC, which enhances the electrophilicity of carboxylate group and converts it in a better leaving group. More in detail, the proton from the carboxylic acid is accepted by one of the N atoms in DCC. The negatively charged oxygen will act as a nucleophile and it will attack the DCC, forming a highly electrophilic intermediate, thanks to the delocalization of the π electrons to the DCC nitrogen atoms. The following step is the nucleophilic attack by NHS to the C=O, which is now more efficient thanks to the electrophilic intermediate. The product was slowly precipitated under diethyl ether atmosphere. The final yield was approximately 50%.

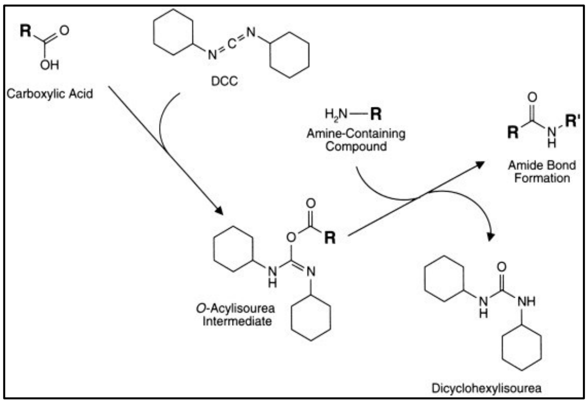

Figure 74. Mechanism of DCC in the amide bond formation starting from a carboxylic acid.

The product has been fully analyzed and characterized since there is no available data in literature. The ESI analysis confirms the successful production of V_6-O-NHS. There are several peaks displaying the loss of one or more TBA cations, such as the $[M\text{-}TBA]^-$ peak at m/z 1416.0 (m/z calculated: 1415.5), $[M\text{-}2TBA+H]^-$ at m/z 1174.7 (m/z calculated: 1174.2), and $[M\text{-}2TBA]^{2-}$ at 586.8 (m/z calculated: 586.5).

The IR spectrum (shown in green), compared to the one of the reagent V_6-O-succinate (blue) confirms that the fingerprint region of the POM between 1000 and 500 cm^{-1} has not undergone any significant variations. It is also possible to notice at 1783 and 1814 cm^{-1} the weak intensity stretching signals related to the C=O of the NHS, which are present in the spectrum of the product, and absent in the one of the reagent. The other assignments are unclear: however, the medium intensity signal at 1205 cm^{-1} might be due to the C-N-C asymmetric stretching, and the low intensity signal at 647 cm^{-1} might be due to the -O-C-N out of plane asymmetric deformation.[103]

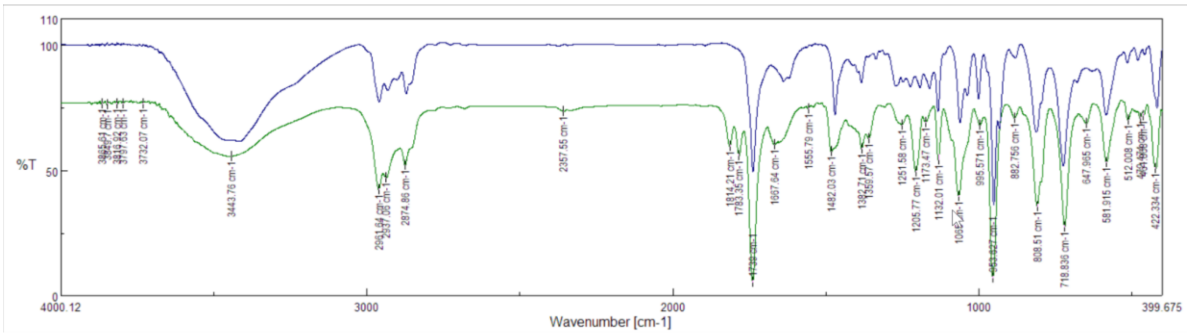

Figure 75. IR spectrum of V_6O-NHS (in green), compared to the reagent V_6-O-succinate (blue).

Continuing with the ^1H NMR spectrum, it is possible to notice at 2.77, overlapped with the leftovers of DMF solvent (-CH_3 singlet, 3H), the signal of the -CH_2- characteristic of N-Hydroxysuccinimide, which prove the reaction has been successfully performed. It is also possible to notice at 2.66 and 2.85 ppm the triplets of the two -CH_2- on each side of the polyoxometalate. The triplet at 2.66 is probably due to the more external CH_2, which is more shielded (thanks to the influence of the nearby N atom of the hydroxysuccinimide, whereas the triplet at 2.85 is probably due to the CH_2 closer to the POM framework. At 3.95 ppm it is possible to note the -CCH_2O- singlet due to the Tris-OH structure. Finally, at 5.01 ppm the singlet of intensity 12 due to the -C(CH_2O-)$_3$ is visible, which confirms that the POM substitution has not changed during the reaction.

The ^{51}V NMR spectrum displays only one singlet at -498.5, which is the proof of a highly symmetrical *anti* Lindqvist-hybrid isomer (bearing two substituents on opposite sides) in which all the six vanadium atoms are equal. This result is in accordance with previous studies found in literature, and appears slightly down-shielded to the corresponding signal of V_6-O-Succinate falling at -501.46.

A sample of the compound has also been analyzed through elementary analysis (C 42.18%, H 6.55%, N 4.10%) which is approximately the same as the calculated values for the structure $C_{50}H_{96}V_6O_{25}N_4$ (C 41.16%, H 6.63%, N 3.84%). The UV spectrum of V_6O-NHS displays a main peak at 199 nm (ε_{199}=64000 $cm^{-1}M^{-1}$) and a shoulder at approximately 221 nm (ε_{221}=44800 $cm^{-1}M^{-1}$).

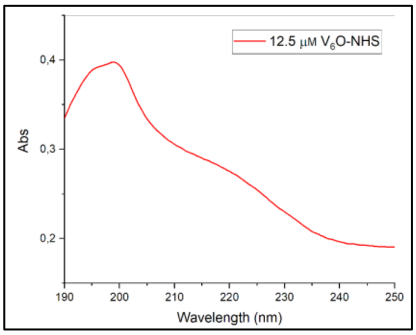

Figure 76. UV spectrum of V_6O-NHS in ACN.

Synthesis 5B "V_6-O – L-Phe" $[(C_4H_9)_4N]_2[V_6O_{13}\{(OCH_2)_3CCH_2OOCCH_2CH_2COPheOMe\}_2]$

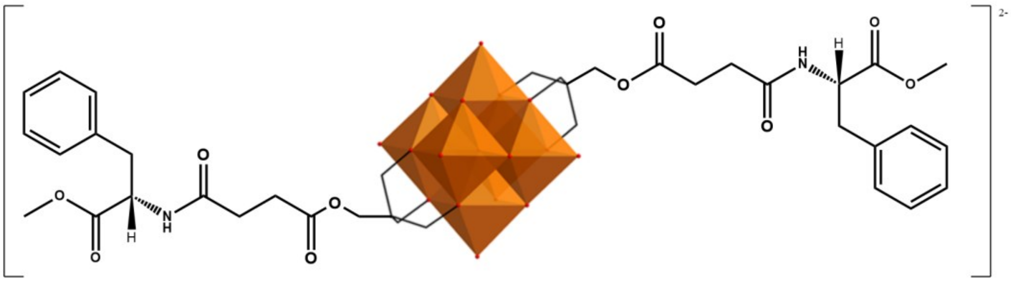

The reaction was performed at room temperature for 24 hours in the presence of dimethylformamide as solvent and N,N-Diisopropylethylamine (DIPEA) as base, since it worked fine with the Mn-Anderson-Evans coupling reactions. The L-amino acid was used in excess to make all the polyoxovanadate react and avoid further purification steps. The final yield was of 86% and the product was a greasy solid, containing minor impurities of the solvent DMF (see NMR spectra in the Appendix).

The ESI-MS(-) in acetonitrile shows a peak at m/z 1544.2, which is coherent with the theoretical m/z 1544.9 due to $[M-TBA]^-$. A second peak at m/z 1302.9 is also noticeable, which is due to $[M-2TBA+H]^-$, whose corresponding calculated value is m/z 1303.4. Finally, a peak at m/z 650.9 is visible, and it is due to $[M-2TBA]^{2-}$ as the theoretical value is m/z 651.

The FT-IR (KBr) spectrum of the product displays no structural changes in the 1000 to 500 cm^{-1} region typical of the polyoxometalate framework. It is possible to notice an intense absorption band at 1668 cm^{-1} caused by the N-C=O amidic bond which is the fundamental feature of the successful synthesis of the hybrid between the amino acid and the polyoxometalate. A medium intensity band at 1538 cm^{-1} may be assigned to the -N-H bending, and at 1160 cm^{-1} a medium intensity signal can be characteristic of the ester C-O in the -O-Me phenylalanine. A weak band is also visible at 2680 cm^{-1} and is probably due to the N-CH aliphatic stretching.

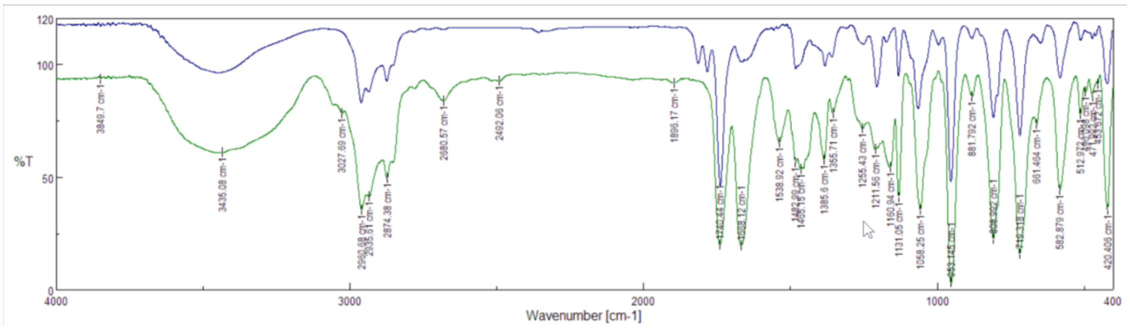

Figure 77. IR spectra of the coupling product V_6O-(L)-Phe in green, and the precursor V_6O-NHS in blu.

The ^{1}H NMR (300Hz) spectrum in CD_3CN presents the multiplet in aromatic area at 7.25 ppm, which is characteristic of the amino acid structure and approximately integrate 10, corresponding to the number of aromatic C-H on both sides of the polyoxometalate (10). The signal at 6.66 ppm might be due to the -C=O**NH**- which would be a confirmation of the successful coupling reaction. The singlet at 3.63 of intensity approximately 6 is caused by $-OCH_3$ of the amino acid used in the reaction. At 5.03 the singlet due to the $-C(CH_2O-)_3$ is visible, as well as a singlet at 3.91 ppm due to the $-CCH_2O-$ proving that the polyoxometalate has remained bis-substituted. The benzylic CH_2 hydrogen signals as well as the central amino acid CH were not attributed probably due to the overlapping with other signals, especially solvents or TBA.

Only one signal was identified in the ^{51}V NMR, which is identical to the one in the V_6-O-NHS form and proves that we are still dealing with a highly symmetrical *anti* Lindqvist-hybrid isomer, which has not changed its nature during the reaction.

Both the UV and CD spectra were recorded for the V_6O-Phe, V_6-OH-NHS and Phe. The first two were 25 µM, and the last, phenylalanine, was 50 µM.

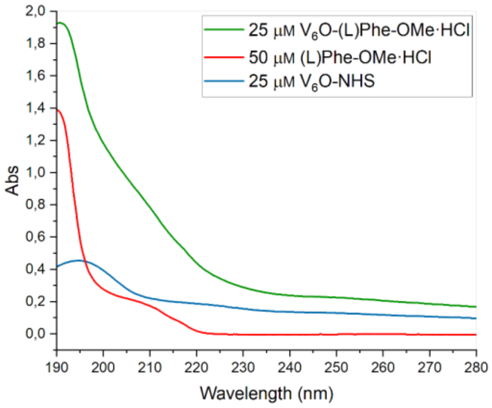

Figure 78. UV spectra of V_6O-PheOMe, and the single precursors at tied concentrations (double for the amino acid).

The UV spectrum of the V_6-O-Phe resembles the shape of the V_6-O-NHS and amino acid alone. It is possible to notice an intense peak whose maximum falls at 191 nm (ε_{191}=150400 $cm^{-1}M^{-1}$) and a shoulder at 209 nm (ε_{209}=69600 $cm^{-1}M^{-1}$). Both these two values are also characteristic of the spectrum of the amino acid alone. The peak due to the V_6-O-NHS is visible at 195 nm (ε_{190}=36000 $cm^{-1}M^{-1}$).

The circular dichroism analysis displays how the coupling product with phenylalanine incorporates the chiral behavior of the amino acid, as well as the metal-oxygen atom transitions, which are now affected by the symmetric environment.

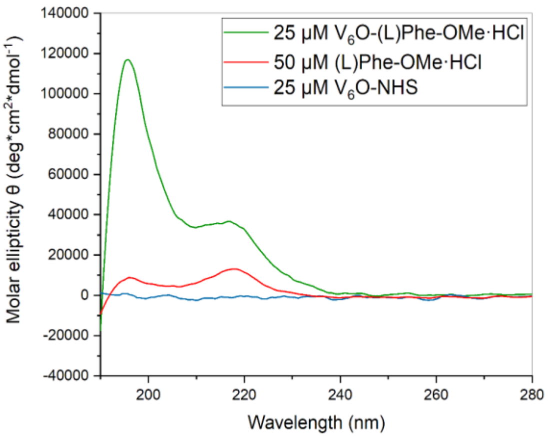

Figure 79. Molar ellipticity of POM V_6O-NHS, V_6-O-Phe (coupling product), and the single amino acid phenylalanine (Phe).

The molar ellipticity maximum of the POM-Phe at 195 nm is 122438 deg*cm^2*$dmol^{-1}$, and a second peak is visible at approximately 216 nm ([θ]=35933 deg*cm^2*$dmol^{-1}$).

The maxima for the amino acid alone fall at the same wavelength as the coupling product V_6-O-Phe.

Synthesis 6B - “V_6-O-DB”

$[(C_4H_9)_4N]_2[V_6O_{13}\{(OCH_2)_3CCH_2OOCCH_2CH_2CO(C_{49}H_{68}N_{13}O_9)\}_2]$

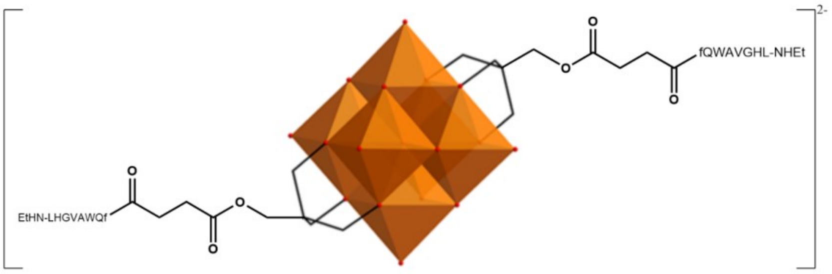

The coupling reaction between V_6O-NHS and Demobesin-1 was performed in similar conditions to the one with the Mn-Anderson POM. An excess of peptide was used, in the presence of DIPEA. The main difference I observed was in the crystallization process, which resulted in a very fast and easy formation of solid which was rapidly purified and dried, as opposed to the purification of the $MnMo_6$-DB compound which required several weeks of wait and multiple attempts to obtain a dry less-porous solid with 73% yield.

Only one fragmentation in the ESI-MS(-) mass analysis performed with solvent acetonitrile was successfully assigned: m/z 1455.9 ($[M\text{-}2TBA]^{2-}$) which is comparable to the calculated value m/z 1455. No mono-functionalized products or unreacted precursors were found.

The FT-IR (KBr) spectrum of the product displays no structural changes in the region typical of the polyoxometalate framework. It is possible to notice an intense absorption band at 1668 cm^{-1} caused by the N-C=O amide bond which is the fundamental feature of the successful synthesis of the hybrid between the peptide and the polyoxometalate. A medium intensity band at 1534 cm^{-1} may be assigned to the -N-H bending.

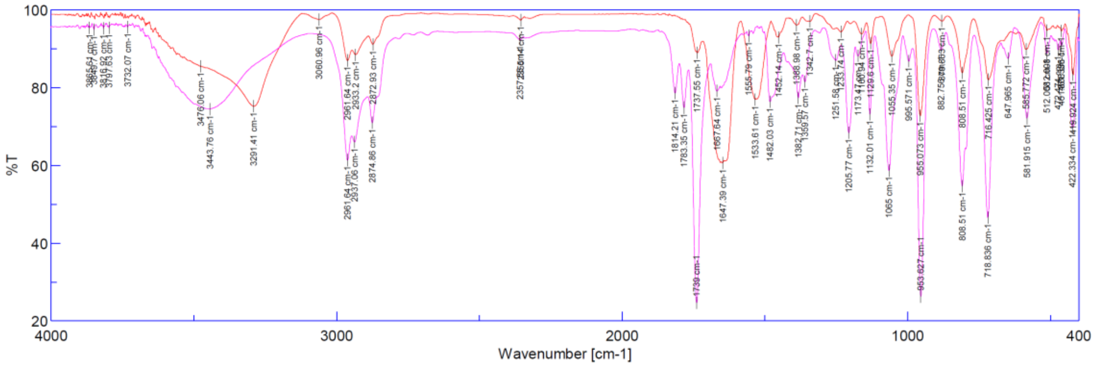

Figure 80. IR spectrum of the coupling product V_6O-DB (in red) and the reagent V_6O-NHS (in purple).

Both UV and CD spectra were recorded for the coupling product V_6O-DB, V_6O-NHS and Demobesin-1 alone with respective concentrations 12.5 µM, 12.5 µM, and 25 µM. The UV spectrum of the V_6O-DB resembles the shape of the Demobesin-1 alone. It is possible to notice a maximum which probably falls at less than 191.5 nm (ε_{191}=169600 $cm^{-1}M^{-1}$) and a shoulder at 218 nm (ε_{218}=112800 $cm^{-1}M^{-1}$). Both these two values are also characteristic of the peptide with a similar wavelength and a lower molar absorption coefficient (ε_{190}=56000 $cm^{-1}M^{-1}$$\varepsilon_{217}$=23200 $cm^{-1}M^{-1}$).

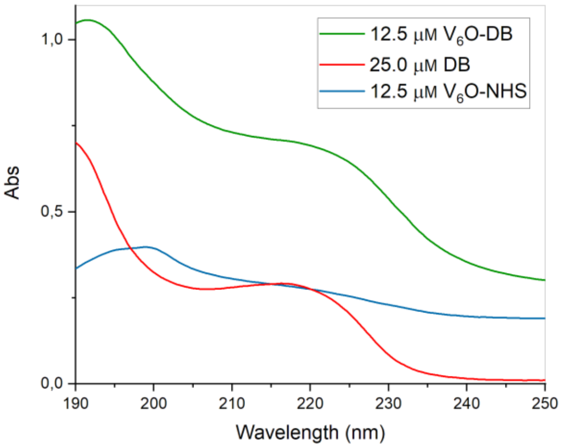

Figure 81. UV spectrum of V_6O-DB, V_6O-NHS and Demobesin-1 in TFE/H_2O 1:10.

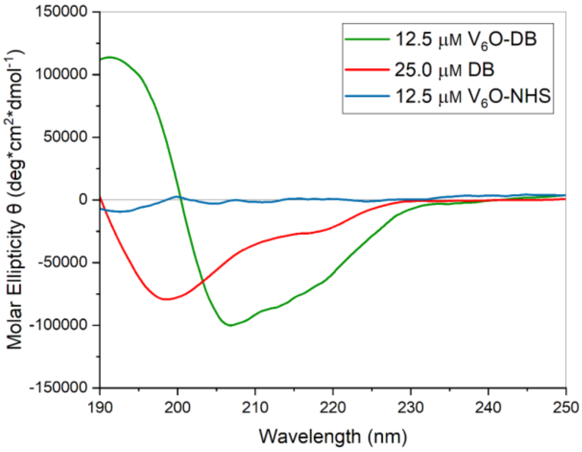

Figure 82. Molar Ellipticity graph of V_6O-DB, V_6O-NHS and Demobesin-1 in TFE/H_2O 1:10.

The molar ellipticity graph of the POM-DB is characterized by a positive Cotton effect. The minimum is located at 207 nm ([θ]=-102122 $deg*cm^2*dmol^{-1}$), and the maximum at less than 190 nm ([θ]=114616 $deg*cm^2*dmol^{-1}$).

The peptide has only one minimum located at 198 nm ([θ]=-79324 $deg*cm^2*dmol^{-1}$). Once again, the influence of the peptide chirality has an impact on the metal centers – oxygen transitions in the POM.

The analysis at different TFE/H_2O ratios appeared similar to the one of the corresponding $MnMo_6$ POM-DB with the difference of higher values of molar ellipticity and a maximum which falls at a slightly shorter wavelength and therefore not fully visible. The secondary structure extrapolation through CDApps for the DB indicates the already discussed preference of beta strand at all the TFE/H_2O ratios, even in pure TFE, whereas the hybrid is found in α-helix at all the ratios following 4:10, and reaches an almost 80% of pseudo α-helix in pure TFE, which is even higher than $MnMo_6$ POM-DB.

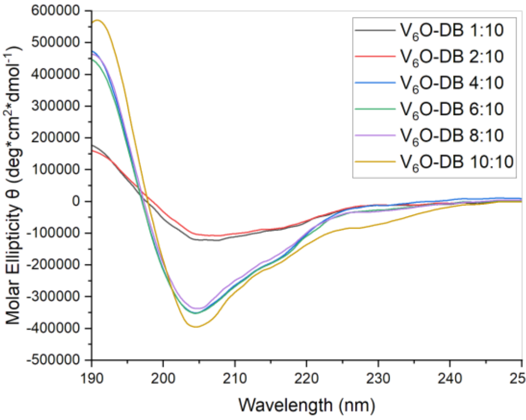

Figure 83. Molar Ellipticity of V_6O-DB 25 µM at different solvent TFE/H_2O ratio: 1:10, 2:20, 4:10, 6:10, 8:10, TFE pure.

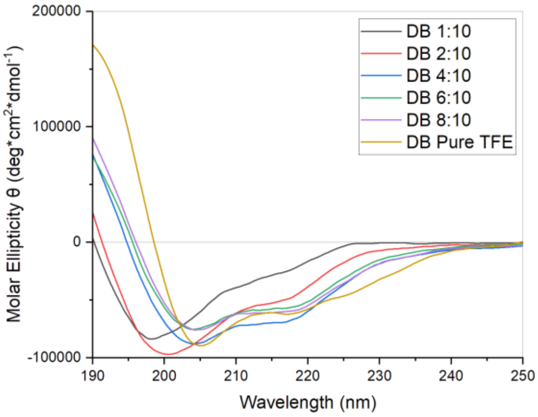

Figure 84. Molar Ellipticity graph of DB at different TFE/H_2O ratio, more in detail 1:10, 2:10, 4:10, 6:10, 8:10, 10:10.

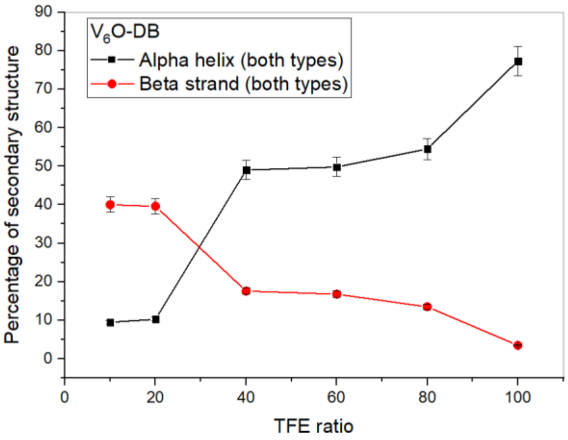

Figure 85. Percentage of α-helix and β-strand for the V_6O-DB at different TFE/H_2O percentages: 1:10, 2:20, 4:10, 6:10, 8:10, TFE pure.

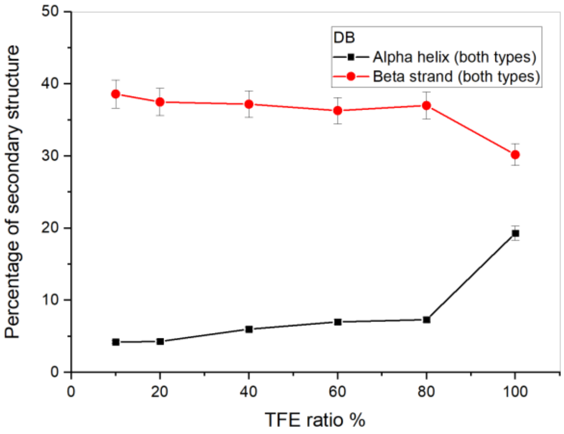

Figure 86. Percentage of α-helix and β-strand for the DB at different TFE/H_2O percentages: 1:10, 2:20, 4:10, 6:10, 8:10, TFE pure.

The 2D NMR spectra of V_6-O-DB in deuterated DMSO appear generally similar to the ones of the $MnMo_6$ POM-DB. The structure of the peptide before and after the coupling reaction was deduced and confirmed through COSY, TOCSY and ROESY, and the shielding effect of the inorganic framework was noticed for this hybrid as well. Another difference for this hybrid was the lack of signals indicating a "match" between valine (5) and tryptophan (3) or any other amino acid. This was not sufficient to exclude a lack of folding between the peptide and the V_6-POM (the up-shifts of the hybrid still indicate some sort of interaction between the two domains); however, the average up-shifts appear lower compared to the $MnMo_6$ POM-DB. The main reason might be the overall charge of the inorganic domain of the Mn-Anderson POM (-3) compared to the V_6-Lindqvist POM (-2) which could indicate weaker interactions between the two domains in the V_6-Lindqvist POM.

	V_6 POM-DB	**DB**

AA	**NH (ppm)**	**CH$_{\alpha}$ (ppm)**	**Rest of the chain (ppm)**	**NH (ppm)**	**CH$_{\alpha}$ (ppm)**
D-Phe	8.28	4.43	-CH$_{2\beta}$ (diastereotopic) 2.79, 2.90 Aromatics not assigned	-	-
Gln	8.32	4.05	-CH$_{2\beta}$ (diastereotopic) 1.75, 1.85 -CH$_{2\gamma}$ 1.55 -NH$_2$ not noticed	8.55	4.33
Trp	7.94	4.49	-CH$_{2\beta}$ (diastereotopic) 2.98, 3.15 Aromatics not assigned	8.30	4.56
Ala	7.93	4.35	-CH$_3$ 1.20	8.25	4.41
Val	7.63	4.15	-CH$_{\beta}$ 2.00 (-CH$_{3\gamma}$)$_2$ 0.85	7.77	4.17
Gly	8.22	-CH$_{2\alpha}$ 3.73	/	8.23	-CH$_{2\alpha}$ 3.72, 3.79
His	8.02	4.48	-CH$_{2\beta}$ 2.93 -NH aromatics not noticed -CH aromatics not assigned	8.13	4.61
Leu	7.94	4.15	-CH$_{2\beta}$ 1.47 -CH$_{\gamma}$ 0.81 (-CH$_{3\delta}$)$_2$ not noticed	8.09	4.20
NHEt	8.08	-CH$_{2\alpha}$ 3.07	-CH$_{3\beta}$ 0.99	8.04	-CH$_{2\alpha}$ 3.08

Table 7. Chemical shift of each amino acid in the Demobesin-1 alone and linked to the POM. Additionally, the side chains of each amino acid in the peptide linked to the POM were identified.

The compound also showed a broad ^{51}V NMR signal at -496.3 ppm.

SYNTHESIS 7B:

Synthesis of “V_6-O - EEEEβAla-fQWAVGHL-NHEt”

$[(C_4H_9)_4N]_2[V_6O_{13}\{(OCH_2)_3CCH_2OOCCH_2CH_2CO(C_{72}H_{101}N_{18}O_{22})\}_2]$

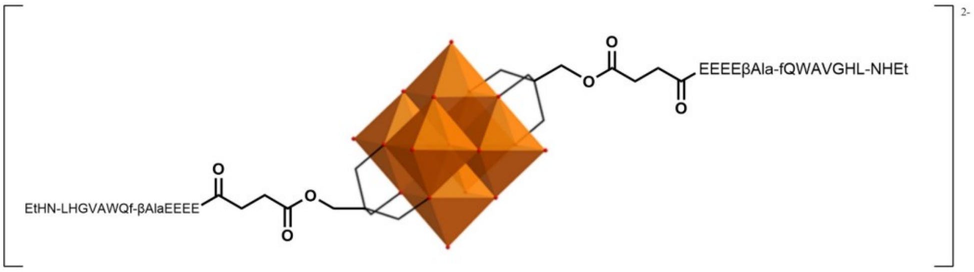

This coupling reaction follows the previous ones and uses once again the spacer “tetra-Glu” seen for the Mn-Anderson Evans POM. The peptide sequence is the same: EEEEβAla-fQWAVGHL-NHEt and also the reaction conditions have remained unvaried (an excess of peptide and hindered base DIPEA). The final yield is 92% and no difficulties were encountered to isolate the product.

The ESI-MS(-) analysis in acetonitrile confirmed the correct synthesis of the product: m/z 2163.7 ($[M\text{-}TBA\text{-}H]^{2-}$) compared to the calculated m/z 2163.7, then 2043.1 ($[M\text{-}2TBA]^{2-}$) with calculated value m/z 2043, and finally m/z 1362.0 ($[M\text{-}2TBA\text{-}H]^{3-}$) compared to the calculated m/z 1361.7. For the first time M-TBA-H fragmentations were noticed in the spectrum, which are probably due to the deprotonation of one of the amino acidic residues or side chains.

The FT-IR (KBr) spectrum shows that the region <1000 cm^{-1} has remained unvaried compared to the precursor V_6-O-NHS, proving that the POM maintains the same structure. The loss of -NHS group signals is noticeable, together with the new peptide bond stretching at 1659 cm^{-1}.

Both the UV and CD spectra were recorded for the coupling product V_6O-EEEEβAlaDB, V_6OH-NHS and DB-βAlaEEEE alone with respective concentrations 12.5 µM, 12.5 µM, and 25 µM.

The UV spectrum graph is coherent with the ones of the other coupling reactions. There are always two visible major peaks of the peptide alone, one at 217 nm (ε_{217}=21600 cm^{-1}M^{-1}) and the other at less than 190 nm (ε_{190}=66400 cm^{-1}M^{-1}) and the same peaks can be found for the coupling product: maximum at slightly less than 190 nm (ε_{190}=289600 cm^{-1}M^{-1}) and a shoulder at 214 nm (ε_{214}=137600 cm^{-1}M^{-1}).

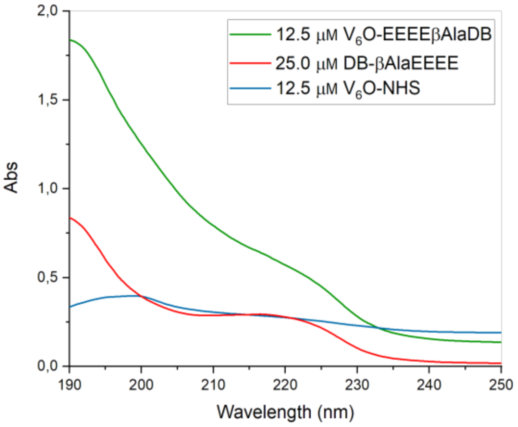

Figure 87. UV spectrum of V_6O-EEEEβAlaDB, V_6O-NHS and DBβAlaEEEE in TFE/H_2O 1:10.

The screening of the molar ellipticity at different TFE/H_2O ratios has been performed both for the peptide alone and for the V_6O-peptide. The molar ellipticity graph of the V_6O-EEEEβAlaDB is characterized both by a minimum and a maximum which are both visible only at high TFE/H_2O ratios. The minimum for pure TFE is

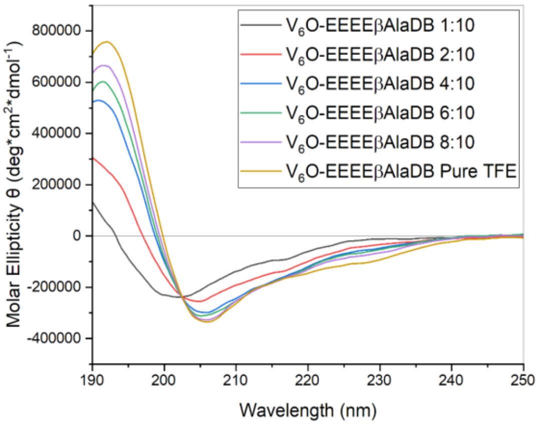

Figure 88. Molar ellipticity of V_6O-EEEEβAlaDB at different ratio of TFE/Water: 1:10, 2:20, 4:10, 6:10, 8:10, and pure TFE.

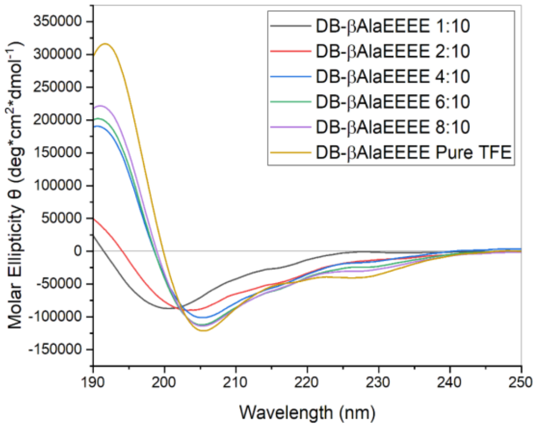

Figure 89. Molar ellipticity of DB-βAlaEEEE at different ratio of TFE/Water: 1:10, 2:20, 4:10, 6:10, 8:10, and pure TFE

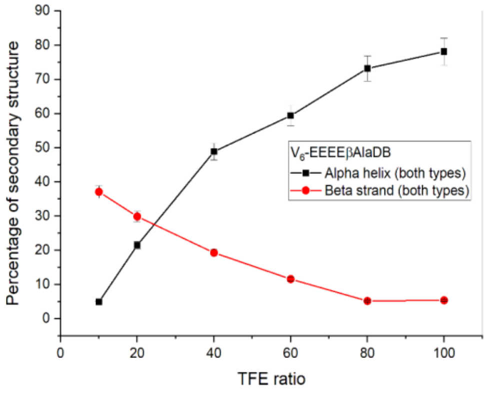

Figure 90. Percentage of α-helix and β-strand for the V_6O- EEEEβAlaDB at different TFE/H2O percentages: 1:10, 2:20, 4:10, 6:10, 8:10, TFE pure.

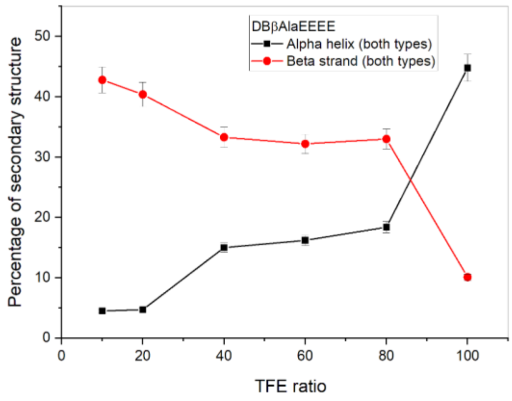

Figure 91. Percentage of α-helix and β-strand for the DB-βAlaEEEE at different TFE/H2O percentages: 1:10, 2:20, 4:10, 6:10, 8:10, TFE pure.

located at 206 nm ([θ]=-338766 deg*cm^2*dmol^{-1}), while the maximum is at 192 nm ([θ]=756593 deg*cm^2*dmol^{-1}). The trend reflects the one of the peptide alone, whose minimum is located at 205 nm ([θ]=-121930 deg*cm^2*dmol^{-1}), and the maximum at 192 nm ([θ]=318350 deg*cm^2*dmol^{-1}). The CDApps contributions to the α-helix and β-strand secondary structures show the same trend as Mn-Anderson polyoxometalates: the peptide remains at a higher percentage in beta strand conformation till 8:10 TFE/H_2O and passes to a pseudo α-helix folding only for the last value in pure TFE. The opposite occurs for the V_6O-EEEEβAlaDB in which the percentage of pseudo α-helix folding overtakes the β-strand after TFE/H_2O ratio 2:10. Therefore it is interesting to note how the inorganic domain induces certain conformational changes in the peptide, which are essential for further analysis of the interactions between the hybrid and the cellular active site.

The 2D ^{1}H NMR analysis (COSY, TOCSY and ROESY) of both the peptide and the V_6O- EEEEβAlaDB have been recorded in deuterated DMSO, and in the ROESY spectrum of the coupling product it is possible to notice the same matching between the amino acids His 12 and Gln 7 which was noticed the corresponding Mn-Anderson Evans coupling product $MnMo_6$-EEEEβAlaDB, and proves a folding of the peptide over itself.

The absence of doubled signals proves that the peptide is symmetric, and the ROESY spectrum has been carefully analyzed to verify that the peptide chain has remained intact during the reaction process. The chemical shifts of DB-βAlaEEEE alone and V_6-EEEEβAlaDB are generally comparable, confirming that the introduction of the spacer was determining.

	V_6-O-EEEEβAlaDB			**DBβAlaEEEE**	
AA	**NH (ppm)**	**CH_α (ppm)**	**Rest of the chain (ppm)**	**NH (ppm)**	**CH_α (ppm)**
Glu^1	8.14	4.23	$-CH_{2\beta}$ 2.24 $-CH_{2\gamma}$ (diastereotopic) 1.72, 1.87	-	-
Glu^2	8.06	4.19	$-CH_{2\beta}$ 2.25 $-CH_{2\gamma}$ (diastereotopic)	8.62	4.35

			1.77, 1.90		
Glu[3]	7.97	4.21	$-CH_{2\beta}$ 2.24 $-CH_{2\gamma}$ (diastereotopic) 1.75, 1.90	8.21	4.25
Glu[4]	7.90	4.14	$-CH_{2\beta}$ 2.20 $-CH_{2\gamma}$ (diastereotopic) 1.73, 1.86	8.01	4.15
bAla	7.84	$-CH_{2\alpha}$ 3.16	$-CH_{2\beta}$ 2.27	7.93	$-CH_{2\alpha}$ 3.11, 3.21
D-Phe	8.29	4.45	$-CH_{2\beta}$ (diastereotopic) 2.94, 2.78 Aromatics not observed	8.27	4.45
Gln	8.34	4.10	$-CH_{2\beta}$ (diastereotopic) 1.78, 1.89 $-CH_{2\gamma}$ 1.59	8.36	4.10
Trp	8.03	4.48	$-CH_{2\beta}$ (diastereotopic) 3.00, 3.17 Aromatics not assigned	8.01	4.48
Ala	7.99	4.38	$-CH_3$ 1.21	7.97	4.37
Val	7.68	4.18	$-CH_{\beta}$ 2.01 $(-CH_{3\gamma})_2$ 0.86	7.61	4.14
Gly	8.24	$-CH_{2\alpha}$ 3.74	/	8.24	$-CH_{2\alpha}$ 3.70, 3.77
His	8.02	4.46	$-CH_{2\beta}$ 2.90 -NH aromatic not observed -CH aromatics not assigned	8.08	4.61
Leu	7.93	4.14	$-CH_{2\beta}$ 1.48 $-CH_{\gamma}$ 0.81	8.07	4.20

			($-CH_{3\delta}$)$_2$ non observed		
NHEt	8.13	$-CH_{2\alpha}$ 3.08	$-CH_{3\beta}$ 1.00	8.04	$-CH_{2\alpha}$ 3.08

Figure 8. Table of the COSY and TOCSY signals for the amino acids composing the V_6-EEEEβAlaDB and the peptide alone.

The hybrid V_6-O-EEEEβAlaDB was also characterized through ^{51}V NMR and only one signal was noticed at 494.7 ppm. Compared to the V_6 O-L-phenylalanine, the signal appears at similar chemical shift, slightly shielded, however it is interesting to notice how the peak is wider. This is due to the different chemical environment the V atoms “feel”, which is characterized by a higher complexity and diversified because of the two bigger substituents.

SYNTHESIS 8B:

Synthesis of “V_6-O - TtdsDB”

$[(C_4H_9)_4N]_3[V_6O_{13}\{(OCH_2)_3CCH_2OOCCH_2CH_2CO(C_{49}H_{68}N_{13}O_9)\}_2]$

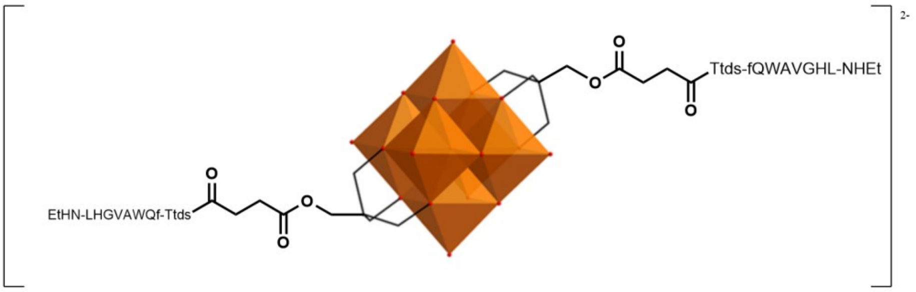

The peptide sequence is H-Ttds-(D-)Phe-Gln-Trp-(β-)Ala-Val-Gly-His-Leu-NHEt, and is the same used in *Synthesis 8A* and the reaction was performed in the same conditions. The final yield was pretty low compared to average (46%) but it is also important to mention that the product had difficulties at drying under vacuum and requested to be constantly spread on the glass surface of the vial before having to be put under vacuum again.

At the ESI-MS(-) analysis only one signal was successfully assigned: m/z 1758.5 ([M-2TBA]$^{2-}$), compared to m/z 1757.7 calculated. No other major peaks were identified, and no signals of the mono-functionalized product or precursors were identified.

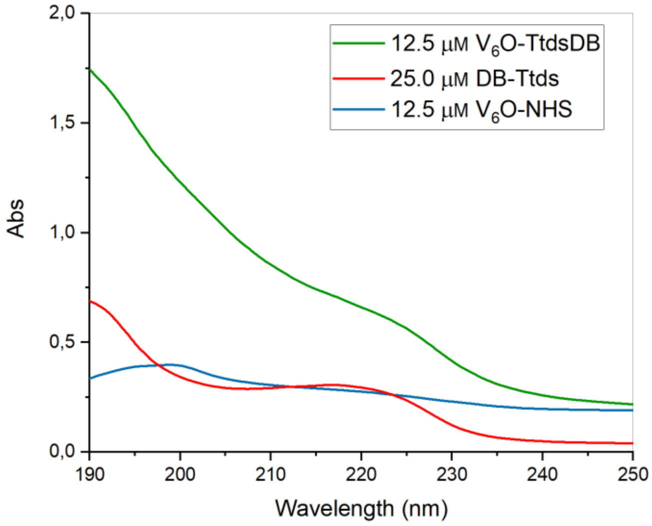

Figure 92. UV spectrum V_6O-TtdsDB, V_6O-NHS and DBTTDS in TFE/H_2O 1:10.

Both the UV and CD spectra were recorded for the coupling product V_6O-TtdsDB, V_6OH-NHS and DB-Ttds alone with respective concentrations 12.5 µM, 12.5 µM, and 25 µM.

The UV spectrum of the V_6O-TtdsDB shows the usual maximum at <190 nm (ε_{190}=289600 cm^{-1}M^{-1}) and shoulder at 218 nm (ε_{218}=120160 cm^{-1}M^{-1}), which resembles the peptide DB-TTDS alone. FT-IR (KBr) spectrum is very similar to the ones previously analyzed, where the bands due to the new peptide bond are visible (1659 cm^{-1} and 1539 cm^{-1}).

The screening of the molar ellipticity at different TFE/H_2O ratios has been performed both for the DB-Ttds alone and for the V_6O-TtdsDB. For the latter, the minimum in pure TFE is located at 206 nm ([θ]=-342728 deg*cm^2*dmol^{-1}), while the maximum is at 192 nm ([θ]=759366 deg*cm^2*dmol^{-1}). The trend reflects the one of the peptide alone. The elaboration through CDApps showed an interesting difference. As previously analyzed in Section 8A, the contributions to the α-helix and β-strand secondary structures for the DB-Ttds alone show that the peptide remains always at a high percentage of beta strand conformation for all the TFE/H_2O ratios, also in pure TFE, which is an important difference compared to the previous peptide DB-βAlaEEEE. The trend resembles the one of Dembesin-1, therefore marking a minor effect due to the spacer. The trend for the V_6O-TtdsDB is similar to the previous ones with a change of the most favorable conformation for > TFE/H_2O ratio 2:10.

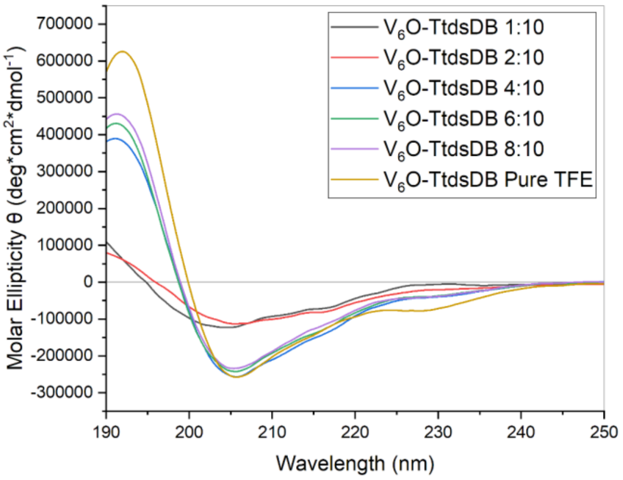

Figure 93. Molar Ellipticity of V_6O-TtdsDB at different ratio of TFE/Water: 1:10, 2:20, 4:10, 6:10, 8:10, and pure TFE.

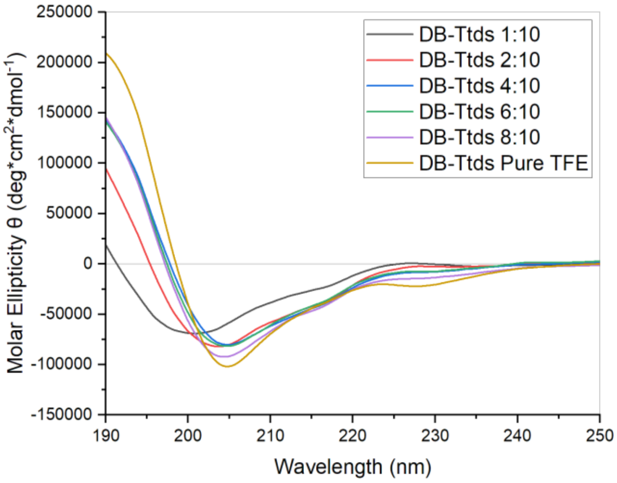

Figure 94. Molar ellipticity of DB-Ttds at different ratio of TFE/Water: 1:10, 2:20, 4:10, 6:10, 8:10, and pure TFE.

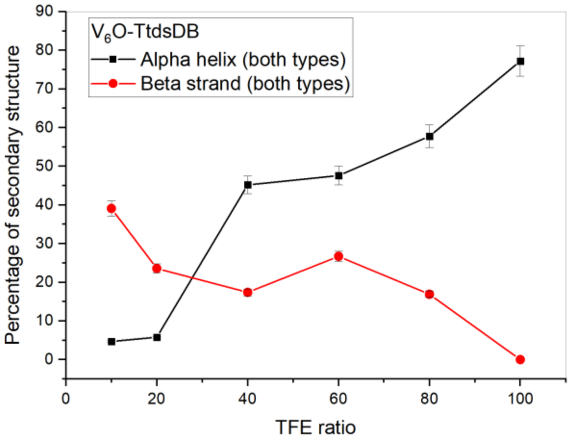

Figure 95. Percentage of α-helix and β-strand for the V_6O-TtdsDB at different TFE/H2O percentages: 1:10, 2:20, 4:10, 6:10, 8:10, TFE pure.

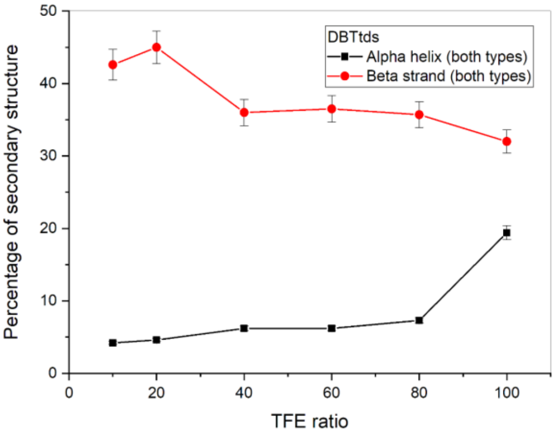

Figure 96. Percentage of α-helix and β-strand for the DBTtds at different TFE/H2O percentages: 1:10, 2:20, 4:10, 6:10, 8:10, TFE pure.

The 2D NMR COSY and TOCSY allowed for the amino acids composing the hybrid and peptide alone to be identified and verified. The values of chemical shift are generally very similar, and in many cases identical to the ones of the $MnMo_6$ POM-Ttds DB, which means the two polyoxometalate frameworks affect the peptide in approximately the same way. Moreover, the chemical shifts of the hybrid are also generally similar to the ones of the peptide alone (±0,01 δ) indicating that the influence of the polyoxometalate is basically absent, which confirms the actual positive impact of the Ttds spacer in reducing the folding of the peptide over the POM. Only the last 2 amino acids in the chain (His and Leu) display a small (0.13ppm) chemical shift variation, (up-field shift), which means there is still some interaction between the POM and peptide. No signal indicating a possible folding of the peptide over itself was identified.

	V_6-O-TtdsDB			**DBTtds**	
AA	**NH (ppm)**	**CH_α (ppm)**	**Rest of the chain (ppm)**	**NH (ppm)**	**CH_α (ppm)**
D-Phe	8.26	4.40	$-CH_{2\beta}$ (diastereotopic) 2.78, 2.94 Aromatics not observed	8.25	4.41
Gln	8.33	4.07	$-CH_{2\beta}$ (diastereotopic) 1.77, 1.89 $-CH_{2\gamma}$ 1.59	8.34	4.07
Trp	7.97	4.48	$-CH_{2\beta}$ (diastereotopic) 3.00, 3.17 Aromatics not assigned	7.98	4.46
Ala	7.92	4.36	$-CH_3$ 1.21	7.90	4.35
Val	7.65	4.17	$-CH_\beta$ 2.00 $(-CH_{3\gamma})_2$ not observed	7.61	4.13
Gly	8.22	$-CH_{2\alpha}$ 3.73	/	8.22	$-CH_{2\alpha}$ 3.70, 3.76
His	8.02	4.47	$-CH_{2\beta}$ 2.92 -NH aromatics not observed -CH aromatics not assigned	8.08	4.60
Leu	7.95	4.13	$-CH_{2\beta}$ 1.47 $-CH_\gamma$ 0.81 $(-CH_{3\delta})_2$ non observed	8.06	4.20
NH-Ttds	7.79	$-CH_{2\alpha}$ 3.04	$-CH_{2\beta}$ 1.58 $-CH_{2\gamma}$ 3.35	7.79	$-CH_{2\alpha}$ 3.03
NHEt	8.11	$-CH_{2\alpha}$ 3.08	$-CH_{3\beta}$ 1.00	8.02	$-CH_{2\alpha}$ 3.06

Table 9. Chemical shift of each amino acid in the DB_Ttds alone and linked to the POM. Additionally, the signals due to the side chains of each amino acid in peptide linked to the POM were identified.

The hybrid V_6-O-Ttds was also characterized through ^{51}V NMR and only one broad signal was noticed at -494.7 ppm, which is the same as the previous synthesis.

SYNTHESIS 9B:

Synthesis of "V_6-O-c(RGDfK)"

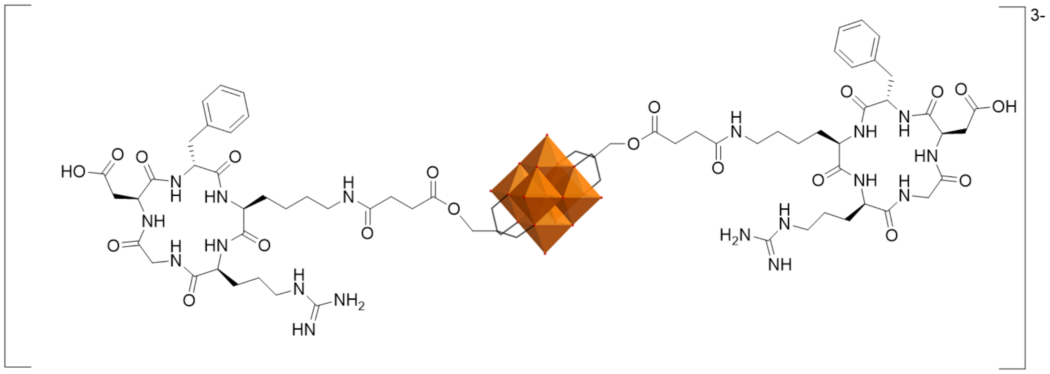

$[(C_4H_9)_4N]_3[V_6O_{13}\{(OCH_2)_3CCH_2OOCCH_2CH_2CO(C_{27}H_{40}N_9O_7)\}_2]$

This coupling reaction has been performed with the cyclic peptide c(RGDfK) and follows the same reaction mechanism as the previous syntheses. The obtained dark red product (yield, 95%) didn't crystallize despite our attempts, and maintained the greasy consistency encountered for the previous couplings. No significant differences in the chemical-physical behaviour of the coupling product have been observed if compared to the DB derivates.

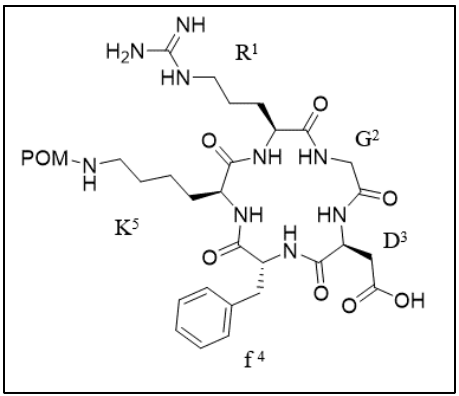

Figure 97. The cyclic peptide c(RGDfK) used in this coupling reaction.

The product has been characterized through ESI-MS(-) analysis in acetonitrile, as it is possible to notice the intense peak at m/z 1075.1 which is due to $[M\text{-}2TBA]^{2-}$ (calculated value m/z 1075.7) and 2152.2 due to $[M\text{-}2TBA+H]^{-}$ (calculated value m/z 2152.0).

The FT-IR (KBr) spectrum is very similar to the ones previously analyzed.

The UV spectrum of the V_6O-c(RGDfK) shows the usual maximum at <190 nm (ε_{190}=211200 cm^{-1}M^{-1}) and shoulder at 211 nm (ε_{211}=164000 cm^{-1}M^{-1}) which resembles the spectrum of the peptide c(RGDfK) alone.

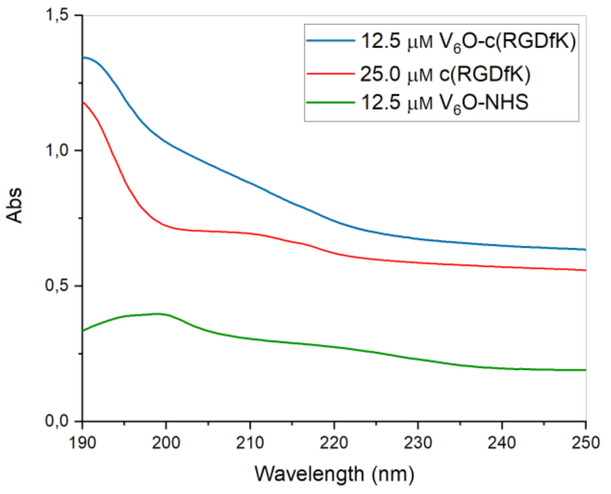

Figure 98. UV-spectra of V_6O-c(RGDfK), V_6OH-NHS and c(RGDfK) with respective concentrations 12.5 μM, 12.5 μM, and 25 μM. The solvent used was a mixture of TFE/H_2O 1:10

The molar ellipticity screening at different TFE/H_2O ratios for the V_6O-c(RGDfK) and c(RGDfK) was performed in the region 190-250 nm. The low solubility of V_6O-c(RGDfK) in water hampers the recording of the corresponding CD and can be the reason for the abnormal trend found at TFE 10% and 20%. The c(RGDfK) instead, show a very low molar ellipticity minimum in water, TFE 10% and TFE 20%.

The minimum for V_6O-c(RGDfK) in pure TFE is located at 207 nm ([θ]=-79633 deg*cm^2*dmol^{-1}) and at 203 nm ([θ]=-29513 deg*cm^2*dmol^{-1}) for the peptide. The elaboration through CDApps was not performed since the peptide structure is by definition cyclic and therefore not as flexible as the peptides in the previous syntheses.

The 2D NMR spectra are similar to the ones of the corresponding $MnMo_6$ POM hybrid, with only minor charges in chemical shifts. A weak interaction between the POM and the peptide may be responsible for a stronger shift of the Arg CH$_\alpha$ signal.

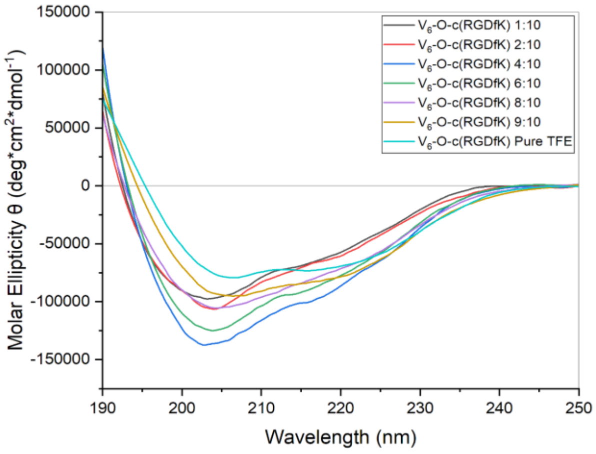

Figure 99. Screening of the behaviour of the molar ellipticity of V_6O-c(RGDfK) at different of TFE/H_2O ratios: 1:10, 2:10, 4:10, 6:10, 8:10, 9:10, pure TFE.

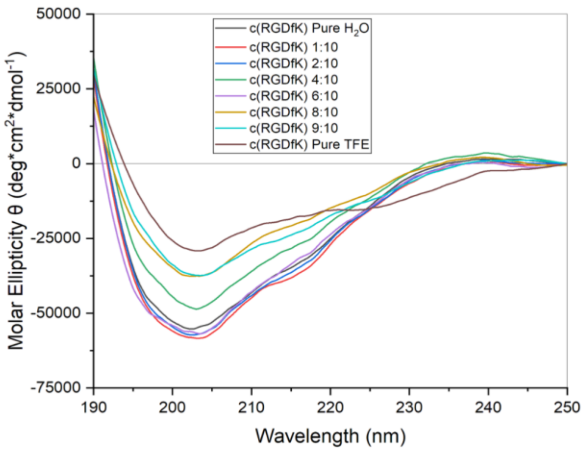

Figure 100. Screening of the behaviour of the molar ellipticity of c(RGDfK) at different of TFE/H_2O ratios: 1:10, 2:10, 4:10, 6:10, 8:10, 9:10, pure TFE.

	V_6O-c(RGDfK)			**c(RGDfK)**	
AA	**NH (ppm)**	**CH_α (ppm)**	**Rest of the chain (ppm)**	**NH (ppm)**	**CH_α (ppm)**
Arg	7.82	2.95	-$CH_{2\gamma}$ 1.32 -$CH_{2\beta}$ 1.11	7.62	4.16
δ-Arg	-	-	-	7.58	-CH_δ 3.09
NH_3^+ Arg	8.23	3.30	/	8.48	3.25 (?)
D-Phe	7.83	4.57	-$CH_{2\beta}$ 2.72 Aromatics not assigned	8.08	4.42
Gly	8.24	-$CH_{2\alpha}$ 4.11	/	8.48	-$CH_{2\alpha}$ 4.05
Asp	8.16	4.39	-$CH_{2\beta}$ (diastereotopic) 2.38, 2.54	8.10	4.64
Lys	8.15	4.12	-$CH_{2\beta}$ (diastereotopic) 1.49, 1.58 -$CH_{2\gamma}$ 1.32 -$CH_{2\delta}$ 1.11	8.09	3.95
NH_3^+ Lys	-	-	-	7.69	-$CH_{2\varepsilon}$ 2.67

Table 3. Chemical shift of each amino acid in the c(RGDfK) alone and linked to the POM. Additionally, the side chains of each amino acid in the hybrid were identified.

The compound also showed a broad ^{51}V NMR signal at -496.2 ppm like the other vanadate hybrids.

Conclusions

This work has spaced from the inorganic world to organic chemistry and biochemistry. Other than a first impact to research, many were the technical skills acquired during my thesis period. $MnMo_6$ and V_6-OH polyoxometalates were successfully synthesized in their activated form. While the molybdates had already been previously synthesized and their study was useful to confirm previous and incomplete results, the vanadates are new compounds. V_6-O-NHS was obtained with a yield of approximately 50% and it was extensively characterized. The coupling reactions between the two NHS-polyoxometalates and L-phenylalanine were successfully performed as a model reaction, and the product was qualitatively characterized through FT-IR, ESI-MS(-), ^1H and ^{51}V NMR (for V_6 POM), CD, UV-Vis and elemental analysis.

The couplings between the two POMs and Demobesin derivatives were performed with a yield generally >70%. In order to understand the behavior of the peptides before and after conjugation, a CD investigation was performed by using a different solvent composition (TFE:H_2O). While the peptides alone remain mainly in a β-strand structure at almost every TFE concentration, when they are grafted on the POM, they display a tendency to evolve into a helicoidal structure as the environment becomes less hydrophilic (TFE:H_2O > 20:80), i.e. when the interactions between the POM and peptide are favored. In the non-aqueous environment used for the 2D ^1H NMR studies, a generally strong shielding effect by both the POMs on the peptide Demobesin-1 was observed, in agreement with a strong impact of the POM on the peptide conformation. In the Mn Anderson POM-DB it was also possible to notice a coupling between Val^5 and Trp^3 which was not observed with V_6O, likely because of the different POM charge. When using the Demobesin-1 with the spacers (DB-βAlaEEEE and DB-Ttds), however, a much lower shift of the signals was observed, speaking in favor of a diminished interaction of the POMs with both types of spacers. The similarity of the spectra, in this case, may suggest that the peptides with the spacers are more available for the interaction with their targets, independently on the spacer and POM used. The only observation was the ROESY cross-coupling signal between His^{12} and Glu^7 in the case of both POMs with βAlaEEEEDB, likely arising from specific interactions along the peptide chain when the negative spacer is added.

The conjugation reaction has also been successfully performed on both POMs by using c(RGDfK). The up-shielding effect of the polyoxometalate was once again noticed; however, some amino acids appeared also down-shielded and this might be due to the particular sort of folding of the peptide on the POM surface, caused also by its rigidity.

Despite all the attempts to obtain crystals of the hybrids, the products precipitated with absorption of DMF, which was easily recognized in all the NMR spectra, highlighting the need of further optimizing the synthetic procedure. In conclusion, this work has successfully contributed in producing more knowledge about the world of POM-peptide conjugates. Further studies will be required, however, to fully understand the nature of the interactions and of self-assembly at both intra- and intermolecular level. To this aim, electron microscopy investigation and theoretical calculations will be useful to depict a model.

All the hybrids in this work will undergo cytotoxicity tests to investigate their impact and selectivity on different types of tumoral cells.

Appendix

SYNTHESIS 1A (TBA)$_4$[α-Mo$_8$O$_{26}$]:

ESI-MS(-)

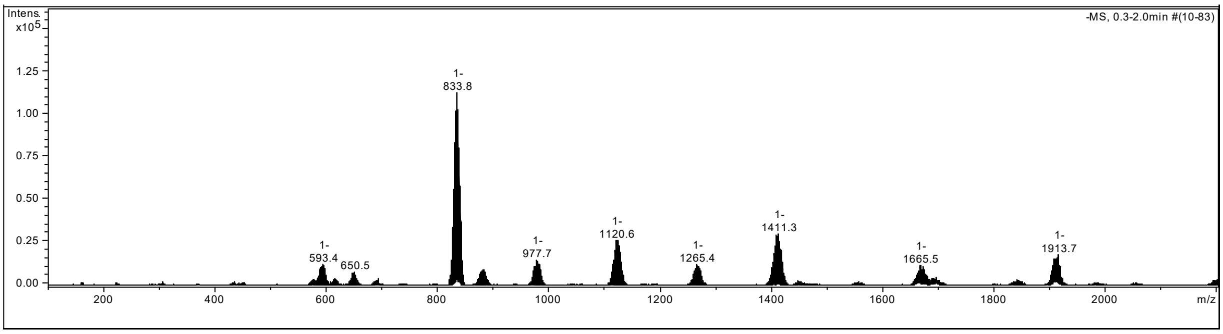

FT-IR:

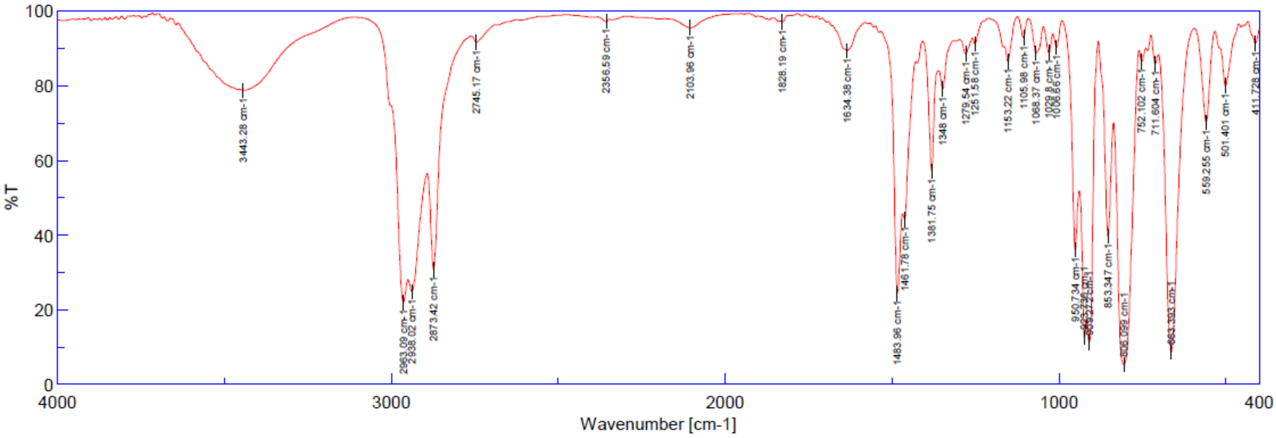

SYNTHESIS 2A [(C$_4$H$_9$)$_4$N]$_3$[MnMo$_6$O$_{18}${(OCH$_2$)$_3$CNH$_2$}$_2$]:

ESI-MS(-)

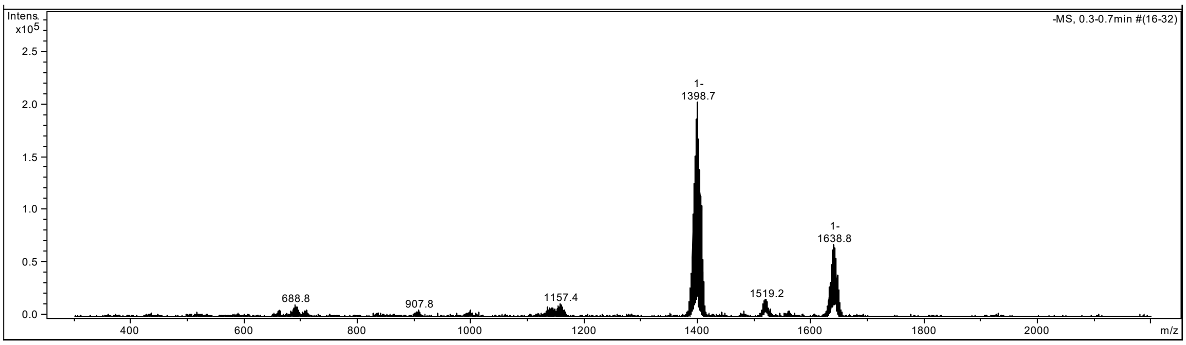

FT-IR:

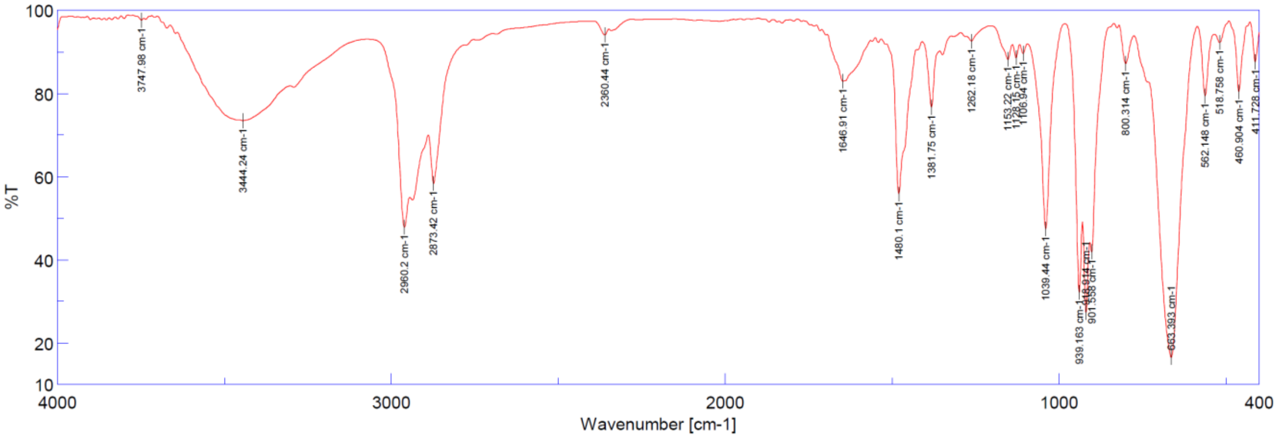

SYNTHESIS 3A $[(C_4H_9)_4N]_3[MnMo_6O_{18}\{(OCH_2)_3CNHCO(CH_2)_2COOH\}_2]$:

ESI-MS(-)

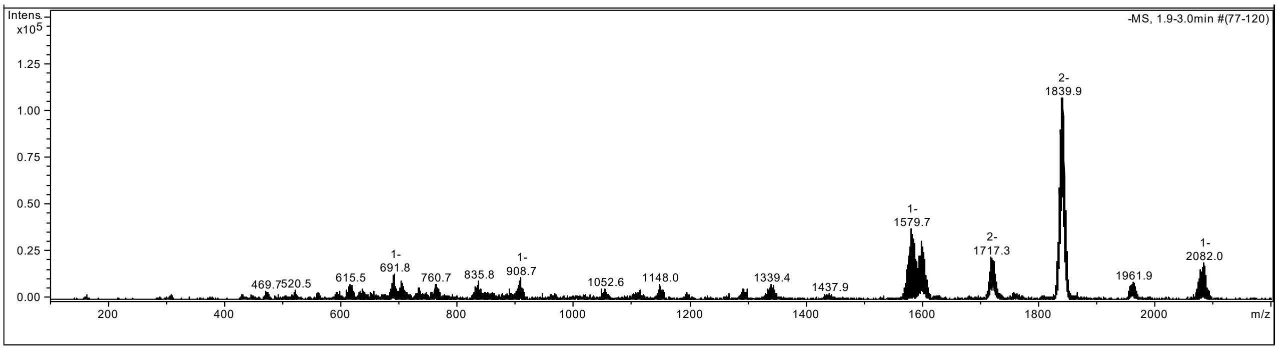

FT-IR:

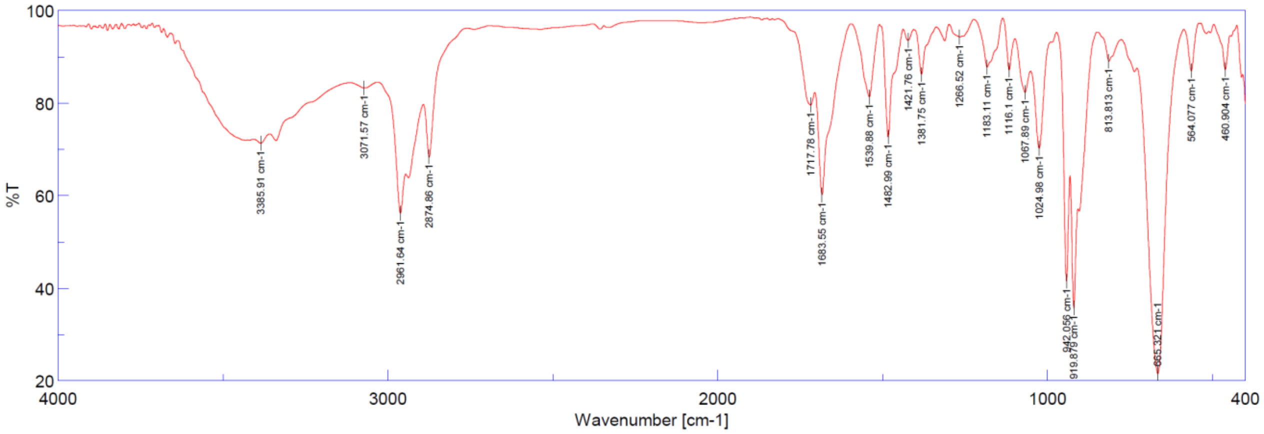

SYNTHESIS 4A

$[(C_4H_9)_4N]_3[MnMo_6O_{18}\{(OCH_2)_3CNHCO(CH_2)_2CO(C_4H_4NO_3)\}_2]$

ESI-MS(-)

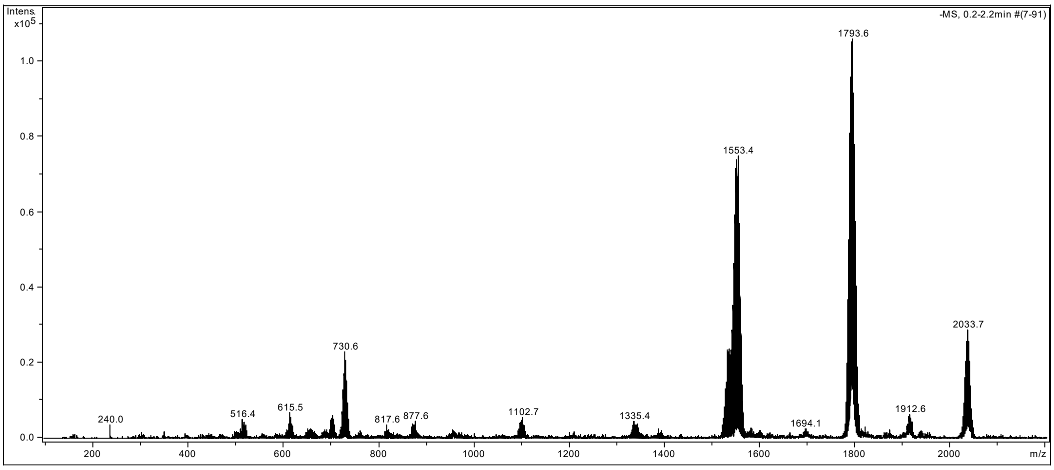

FT-IR:

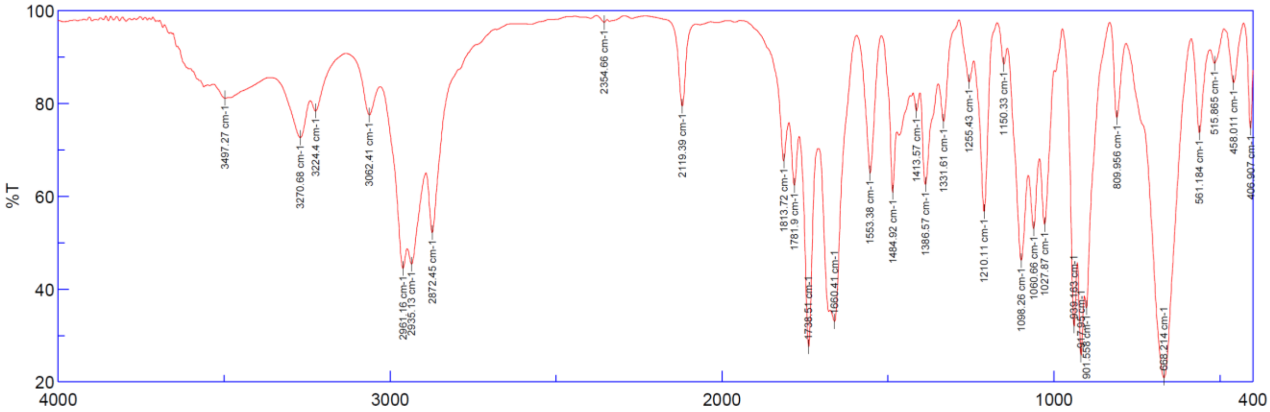

SYNTHESIS 5A $[(C_4H_9)_4N]_3[MnMo_6O_{18}\{(OCH_2)_3CNHCO(CH_2)_2COPhe\}_2]$

ESI-MS(-)

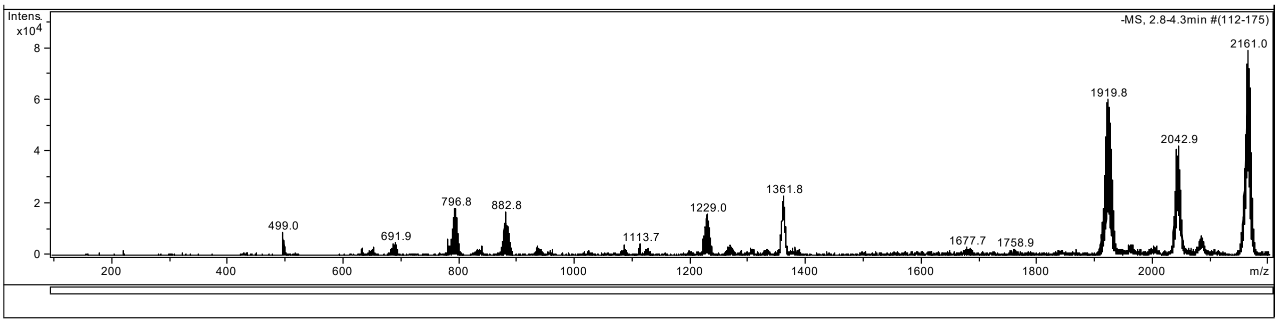

FT-IR:

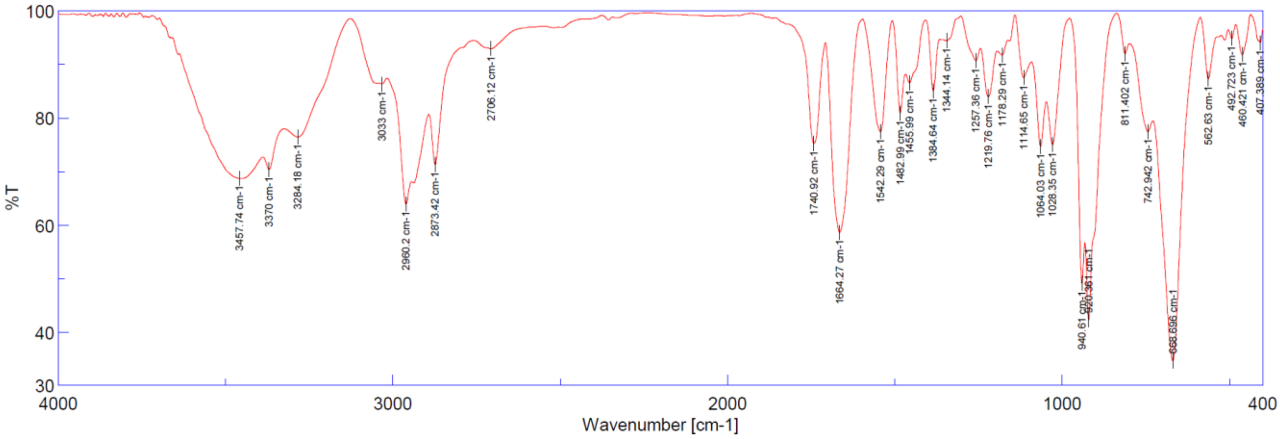

1H NMR (CD_3CN):

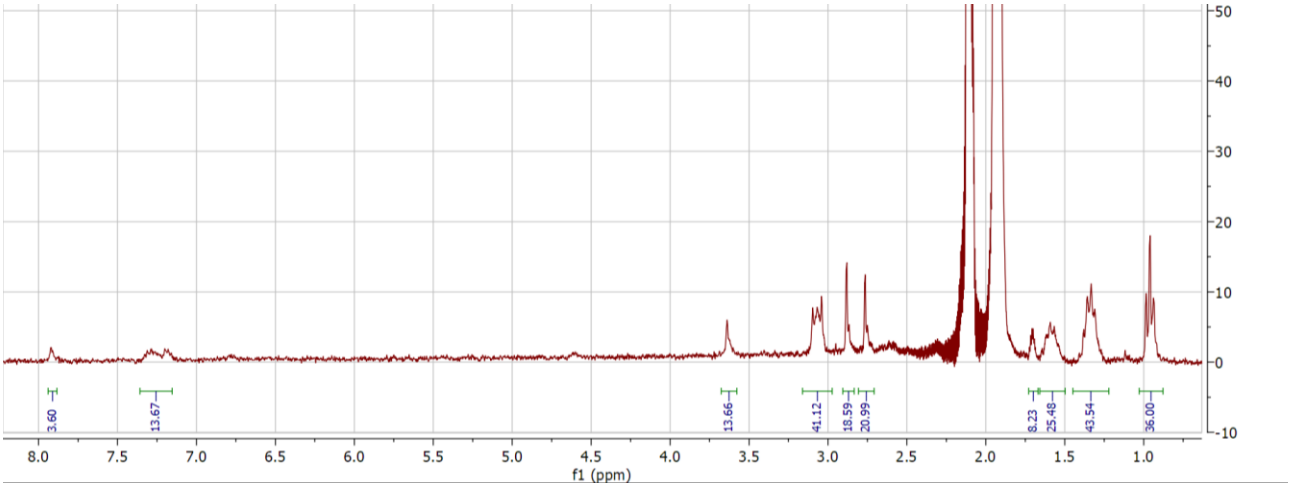

Elemental Analysis:

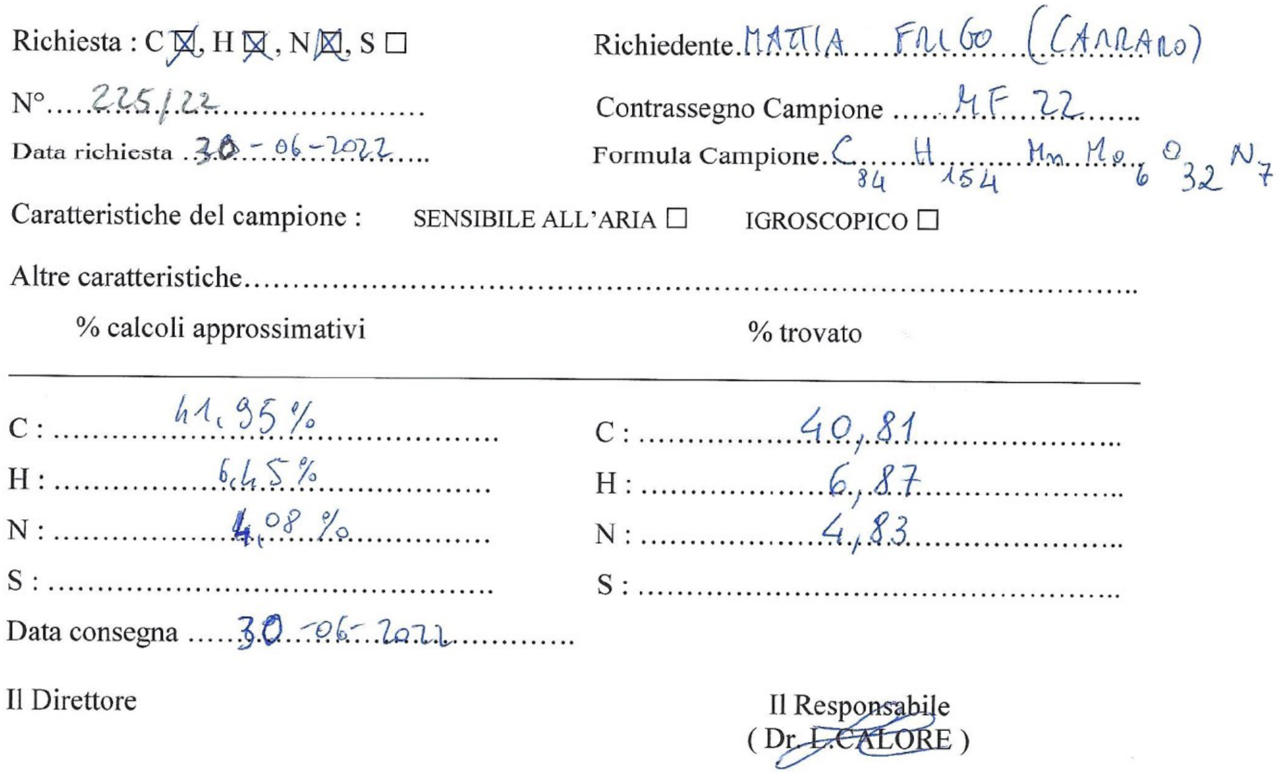

Richiesta : C ☒, H ☒, N ☒, S ☐

Richiedente MATTIA FRIGO (CARRARO)

N° 225/22

Contrassegno Campione MF 22

Data richiesta 30-06-2022

Formula Campione $C_{84}H_{154}MnMo_6O_{32}N_7$

Caratteristiche del campione : SENSIBILE ALL’ARIA ☐ IGROSCOPICO ☐

Altre caratteristiche

% calcoli approssimativi	% trovato
C : 41,95 %	C : 40,81
H : 6,45 %	H : 6,87
N : 4,08 %	N : 4,83
S :	S :

Data consegna 30-06-2022

Il Direttore

Il Responsabile
(Dr. L. CALORE)

SYNTHESIS 6A “MnMO$_6$ POM-DB”

$[(C_4H_9)_4N]_3[MnMo_6O_{18}\{(OCH_2)_3CNHCO(CH_2)_2CO(C_{49}H_{68}N_{13}O_9)\}_2]$

ESI-MS(-)

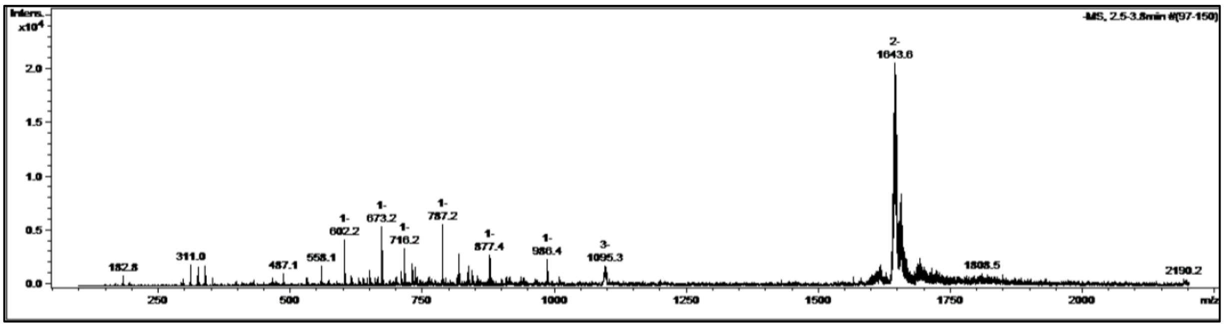

FT-IR:

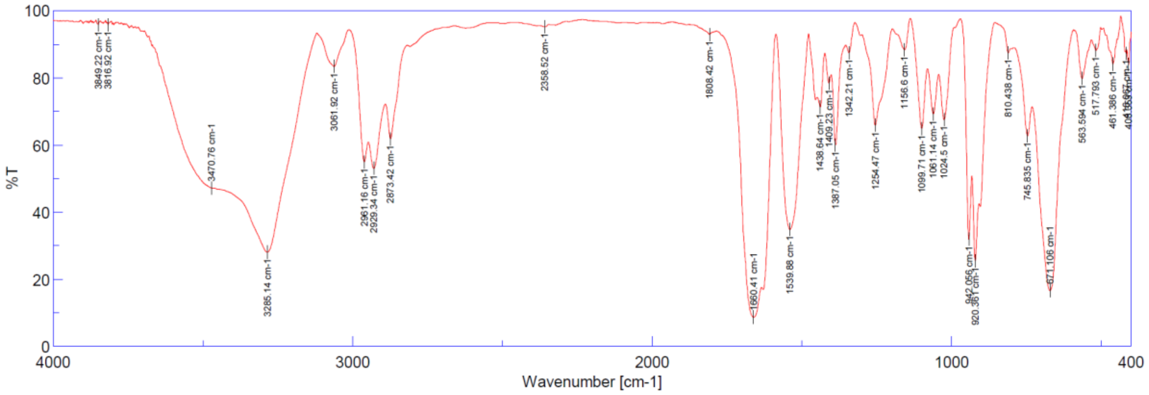

2D ^{1}H NMR (COSY):

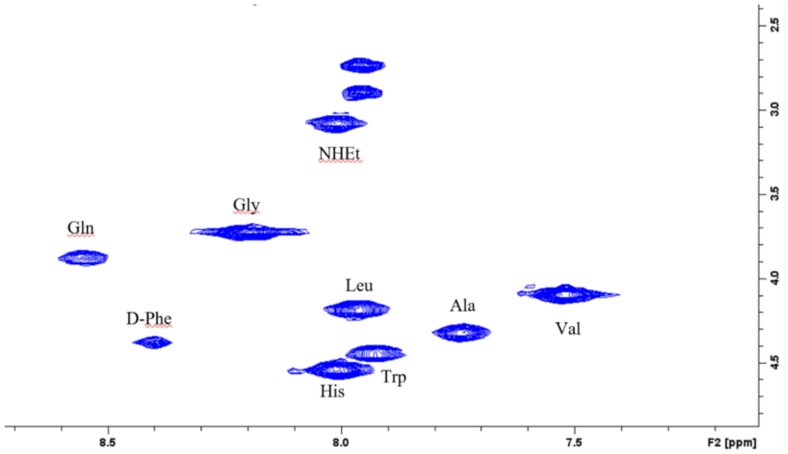

COSY of MnMo₆ POM-DB

2D ^{1}H NMR (ROESY):

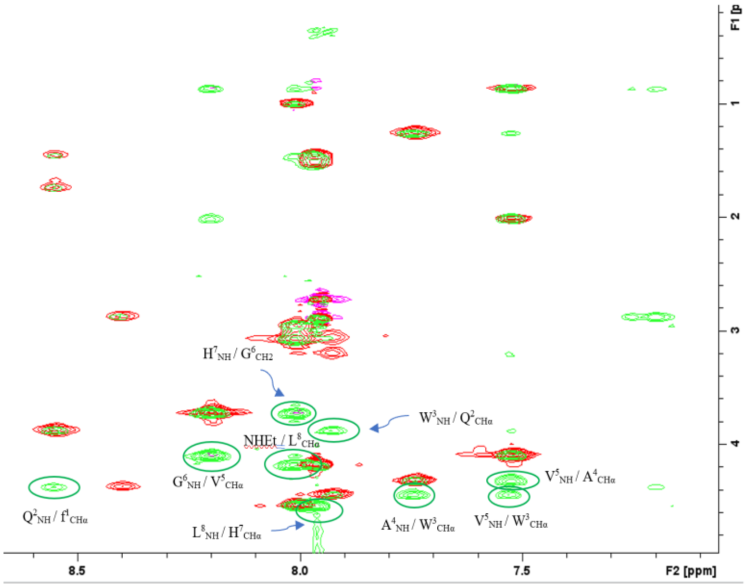

TOCSY and ROESY of MnMo₆ POM-DB

SYNTHESIS 7A - “$MnMo_6$ POM- EEEEβAla-fQWAVGHL-NHEt”

$[(C_4H_9)_4N]_3[MnMo_6O_{18}\{(OCH_2)_3CNHCO(CH_2)_2CO(C_{72}H_{101}N_{18}O_{22})\}_2]$

ESI-MS (-):

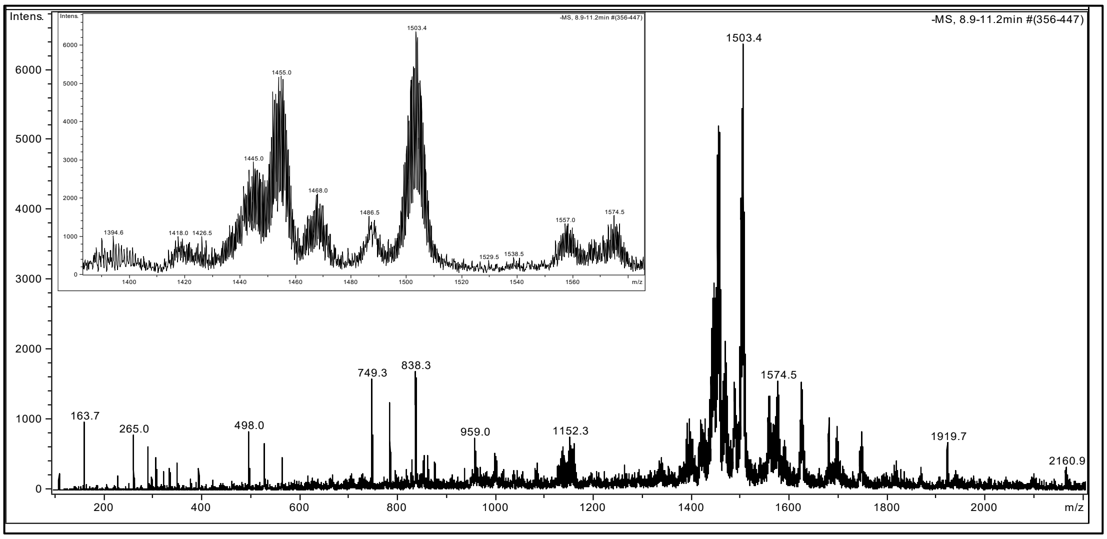

FT-IR:

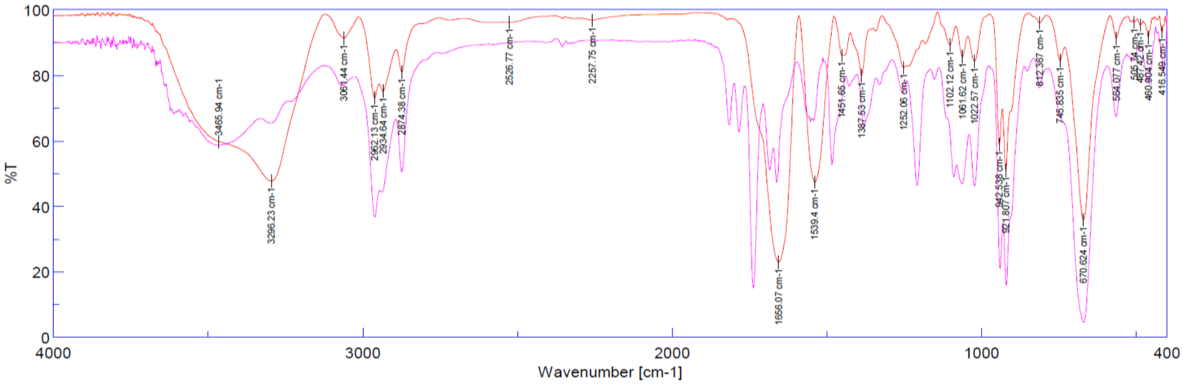

FT-IR spectrum of the reagent POM-NHS (in purple) and the final coupling product (in red).

2D ^{1}H NMR (COSY):

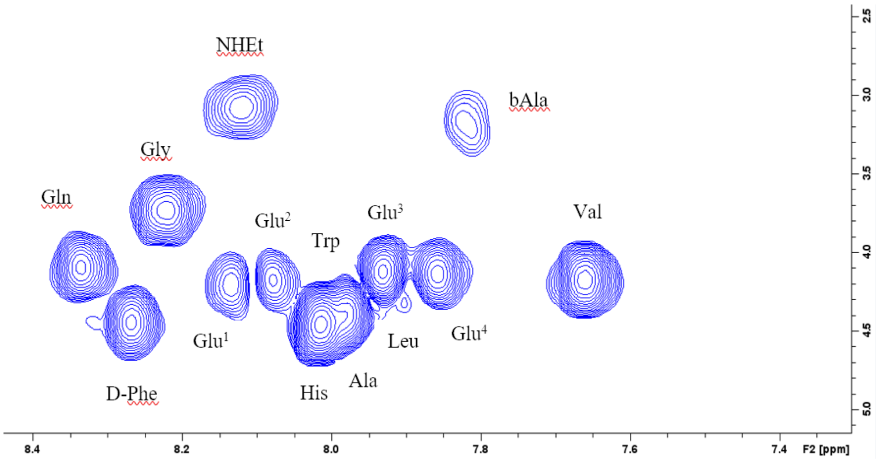

COSY signals for POM-EEEEβAlaDB

2D ^{1}H NMR (TOCSY and ROESY):

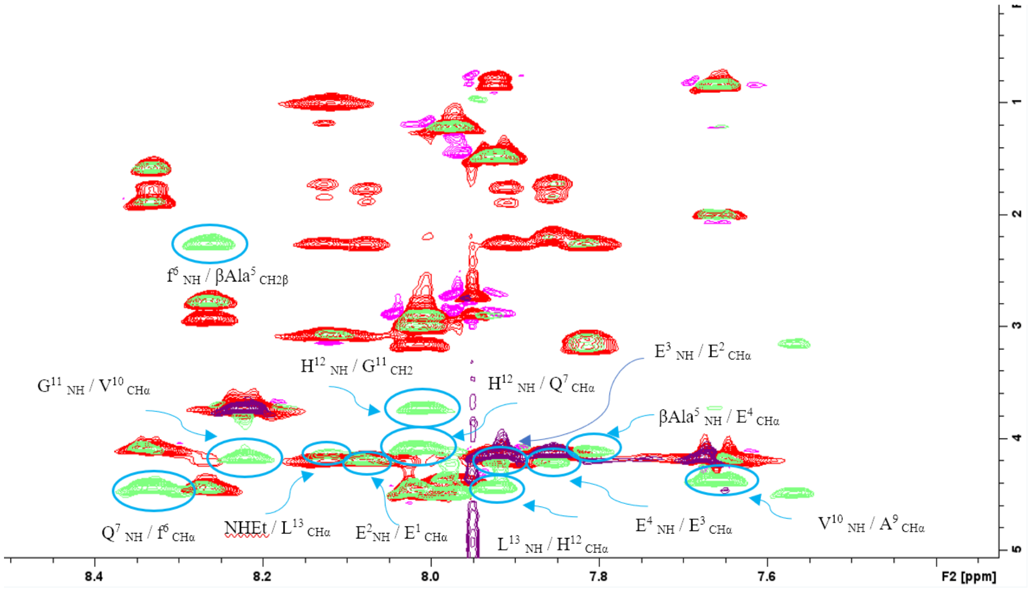

^{1}H ROESY of POM-EEEEβAlaDB (in green) overlapped with TOCSY (in red). It is possible to notice the match between the amino acids His 12 and Gln 7.

SYTHESIS 8A - “MnMo₆ POM-DB-TTDS”

$[(C_4H_9)_4N]_3[MnMo_6O_{18}\{(OCH_2)_3CNHCO(CH_2)_2CO(C_{49}H_{68}N_{13}O_9)\}_2]$

ESI-MS(-):

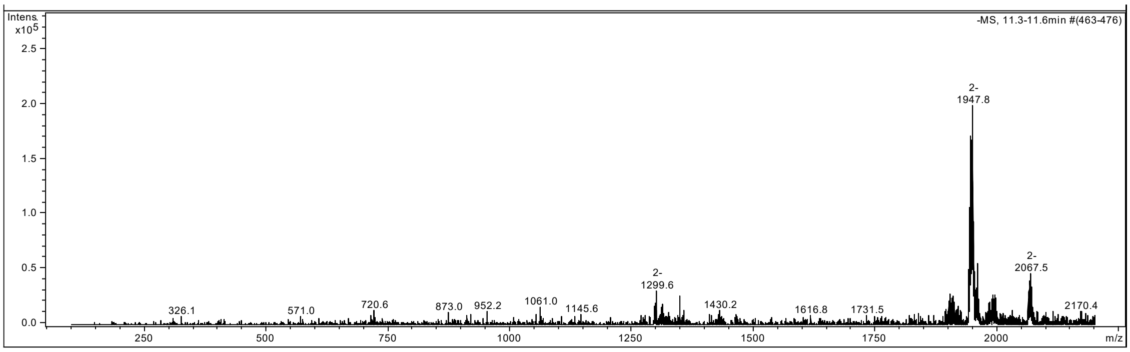

FT-IR:

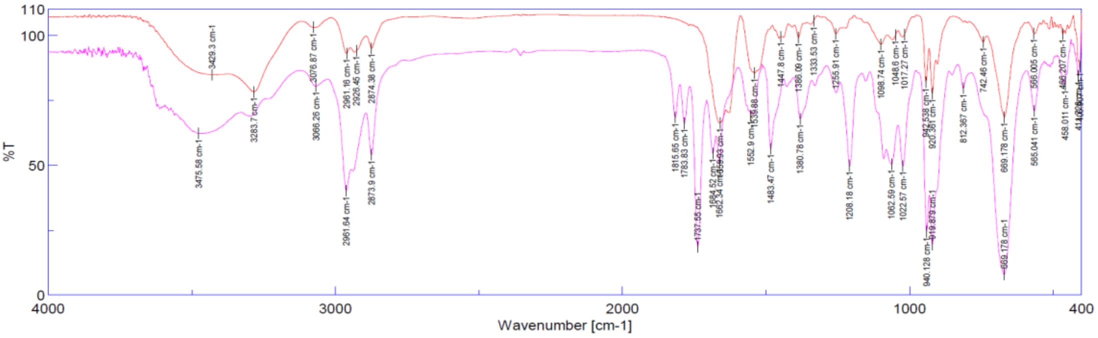

FT-IR spectrum of the reagent POM-NHS (in purple) and the final coupling product MnMo₆-TtdsDB (in red).

2D ^{1}H NMR (COSY):

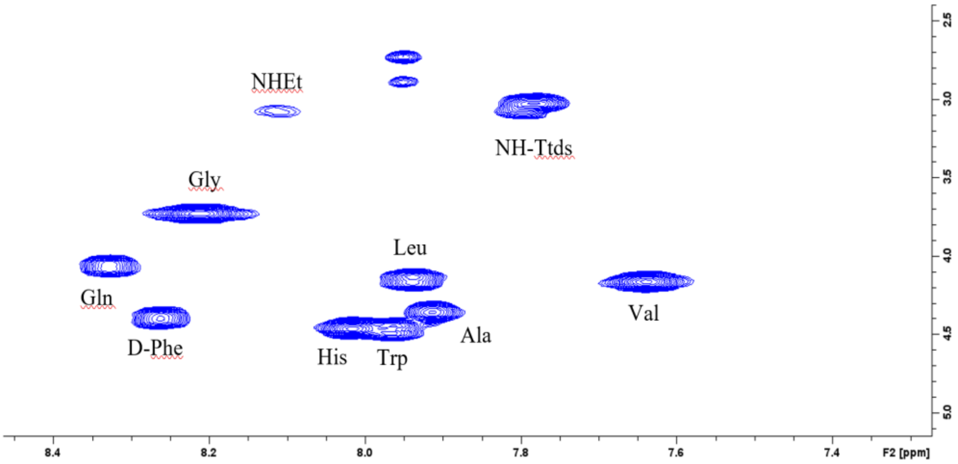

COSY signals for POM-TtdsDB

2D ^{1}H NMR (TCOSY and ROESY):

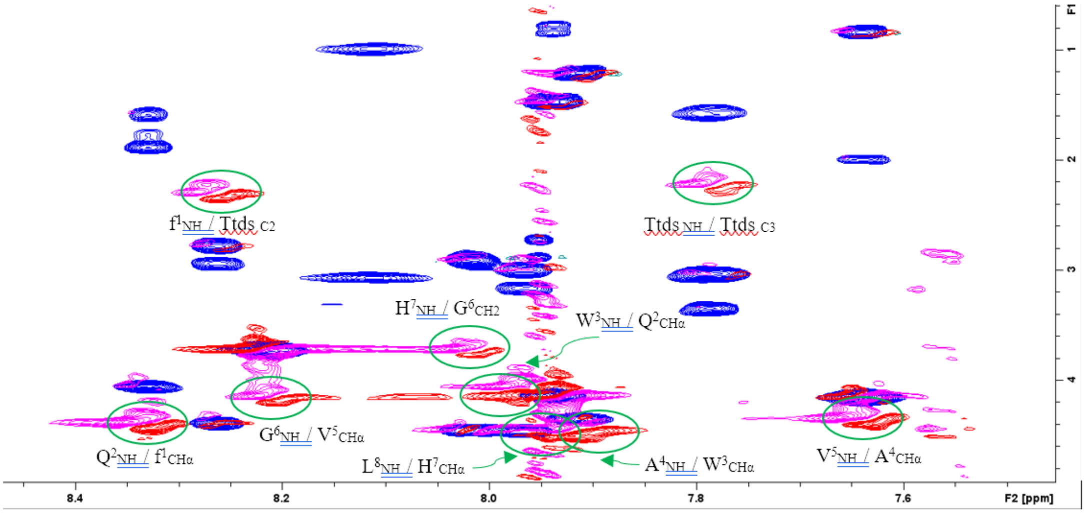

TOCSY and ROESY of POM-TtdsDB

SYNTHESIS 9A:

Synthesis of “MnMo$_6$-RGD”

$[(C_4H_9)_4N]_3[MnMo_6O_{18}\{(OCH_2)_3CNHCO(CH_2)_2CO(C_{27}H_{40}N_9O_7)\}_2]$

ESI-MS(-):

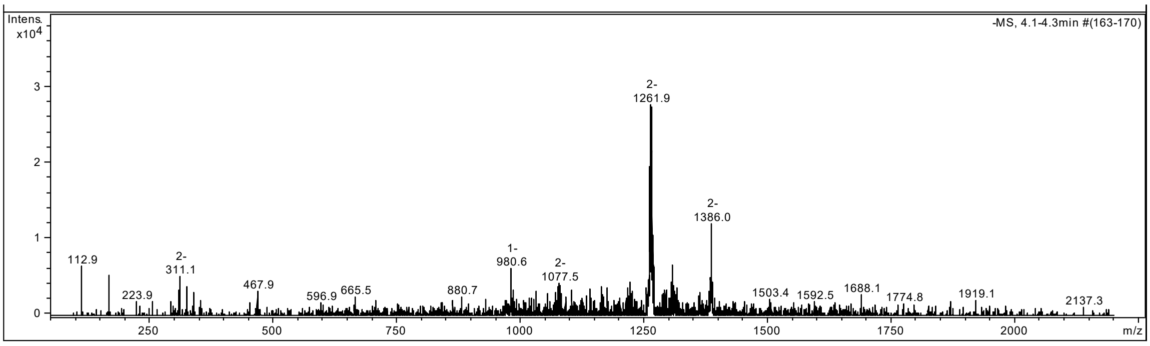

FT-IR:

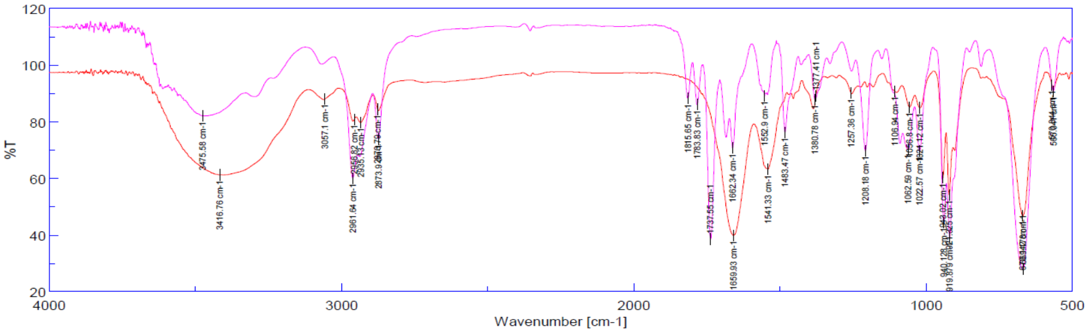

IR spectrum of MnMo₆ POM-NHS and MnMo₆ POM c(RGDfK).

2D ^{1}H NMR (COSY):

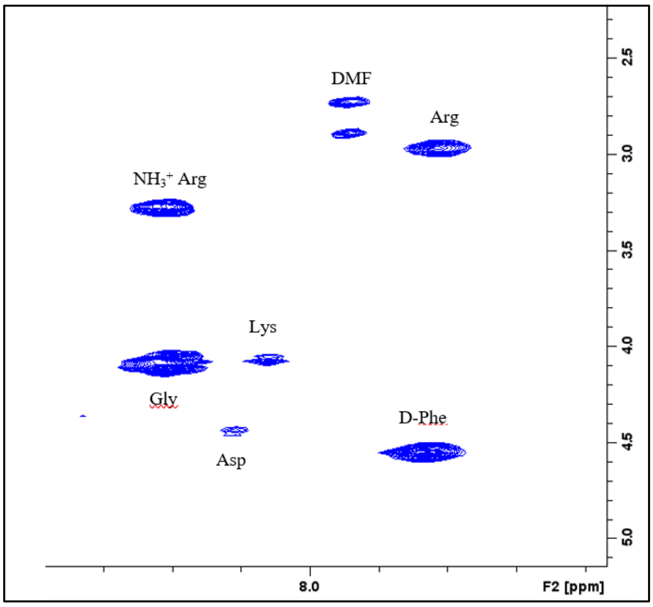

COSY signals for POM-TtdsDB

2D ^{1}H NMR (TOCSY and ROESY):

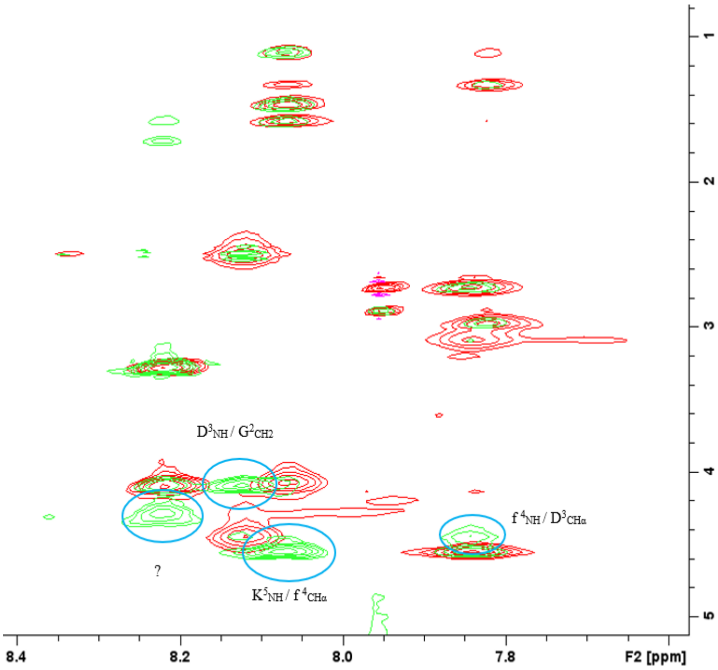

TOCSY and ROESY of POM-c(RGDfK)

SYNTHESIS 2B "V₆-OH" - $[(C_4H_9)_4N]_2[V_6O_{13}\{(OCH_2)_3CCH_2OH\}_2]$

ESI-MS(-)

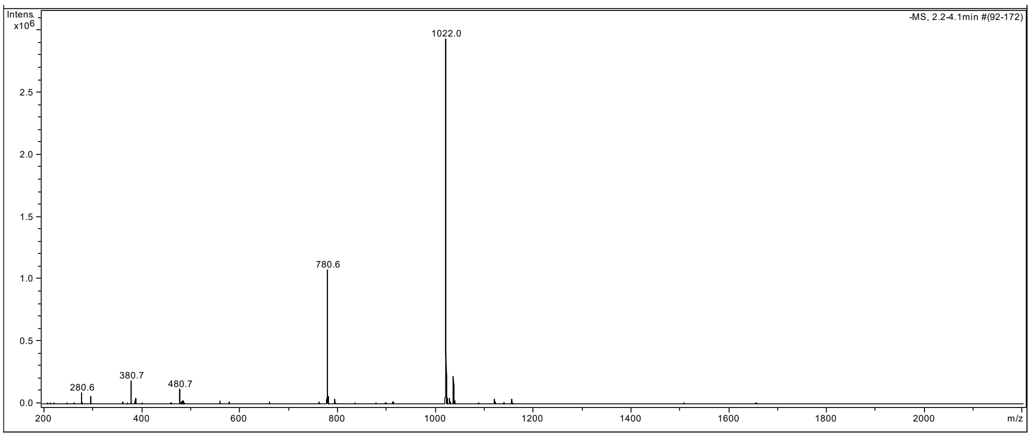

FT-IR:

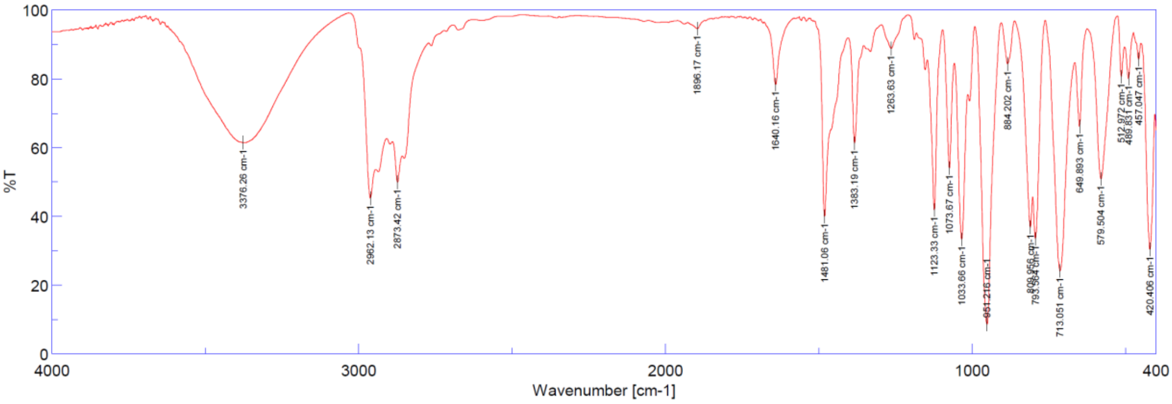

SYNTHESIS 3B "V₆-OH-Succinate"
$[TBA]_2[V_6O_{13}\{(OCH_2)_3CCH_2OOCCH_2CH_2COOH\}_2]$

ESI-MS(-)

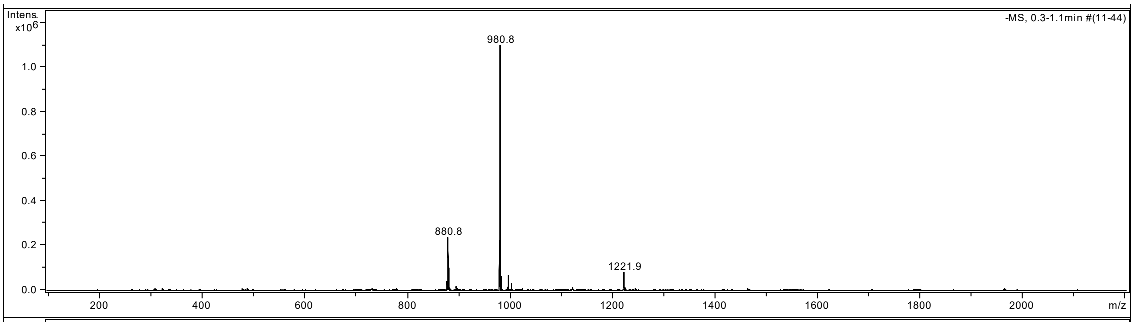

FT-IR:

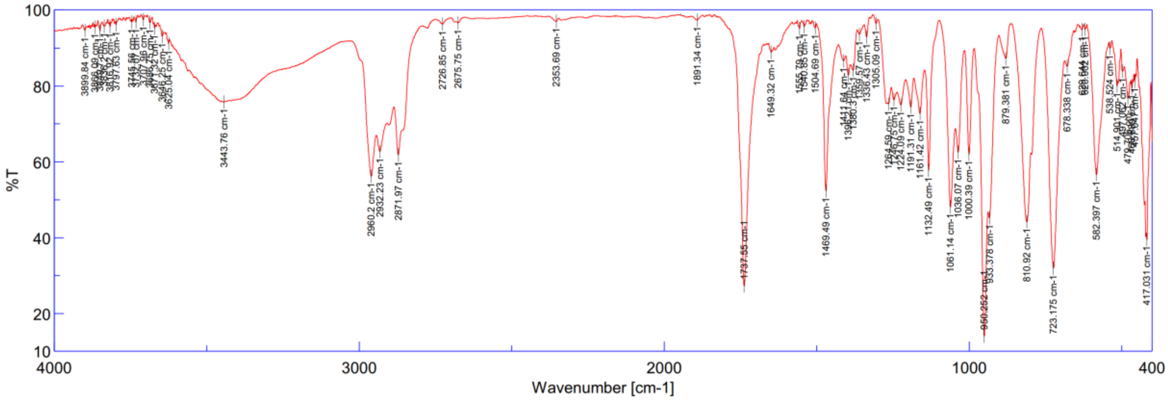

SYNTHESIS 4B “V$_6$-O-NHS” - [TBA]$_2$[V$_6$O$_{13}${(OCH$_2$)$_3$CCH$_2$OOCCH$_2$CH$_2$CO(C$_4$H$_4$NO$_3$)}$_2$]

ESI-MS(-)

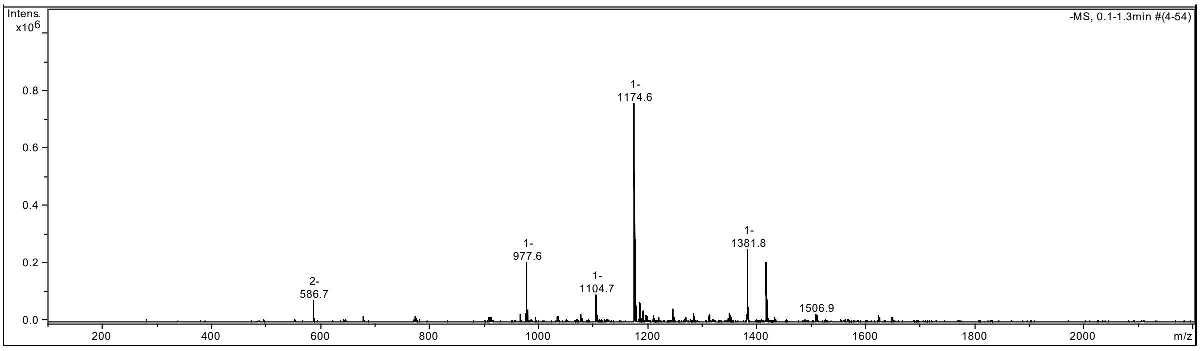

FT-IR:

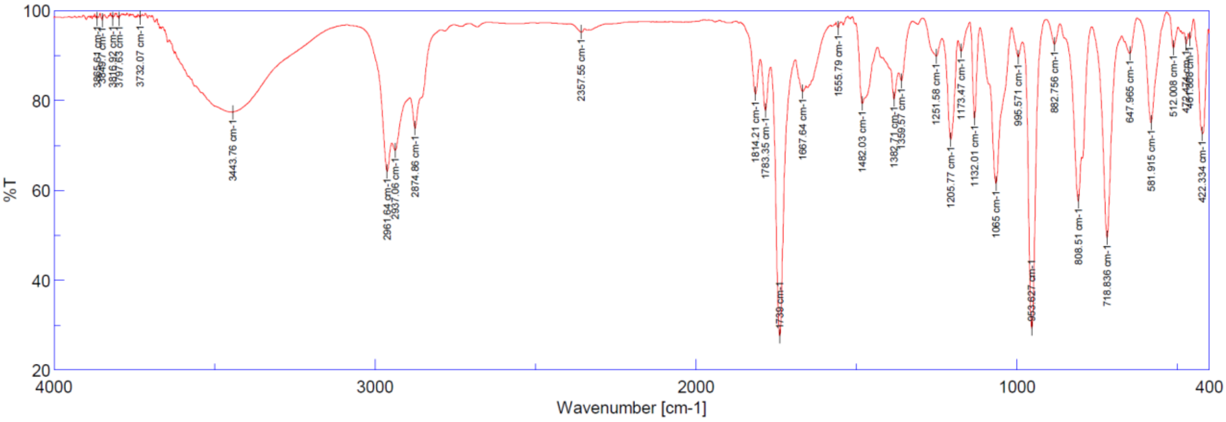

^{1}H NMR 300 (CD_3CN)

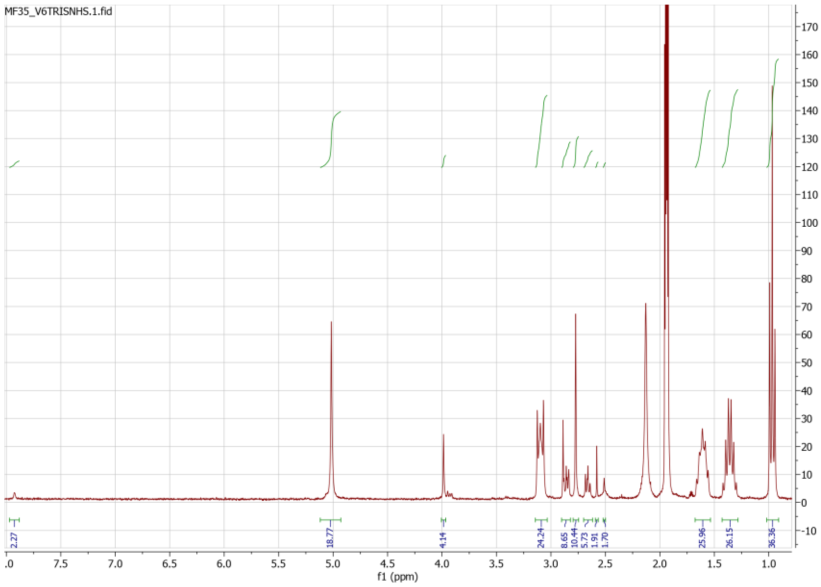

^{51}V NMR 300 (CD_3CN)

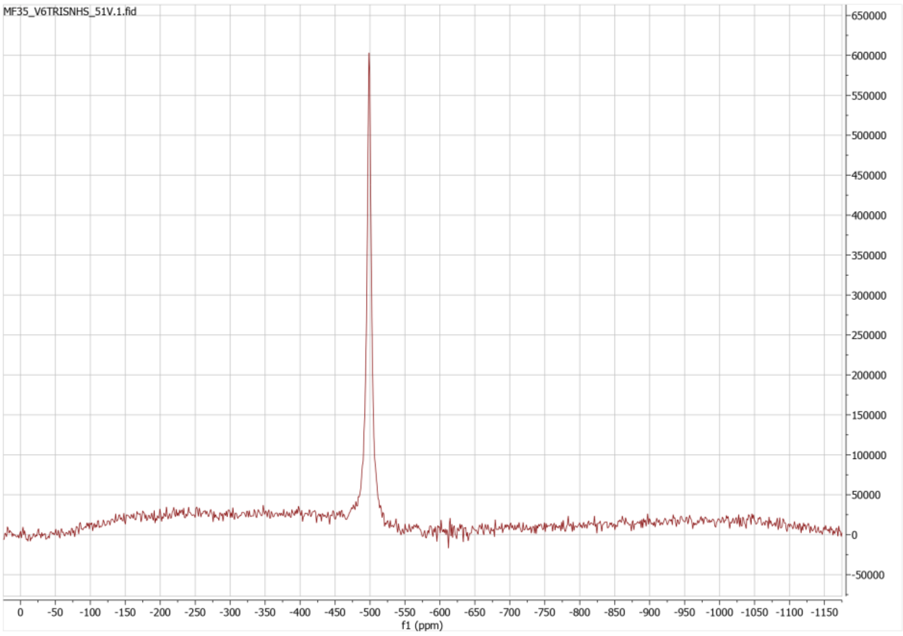

Elemental Analysis:

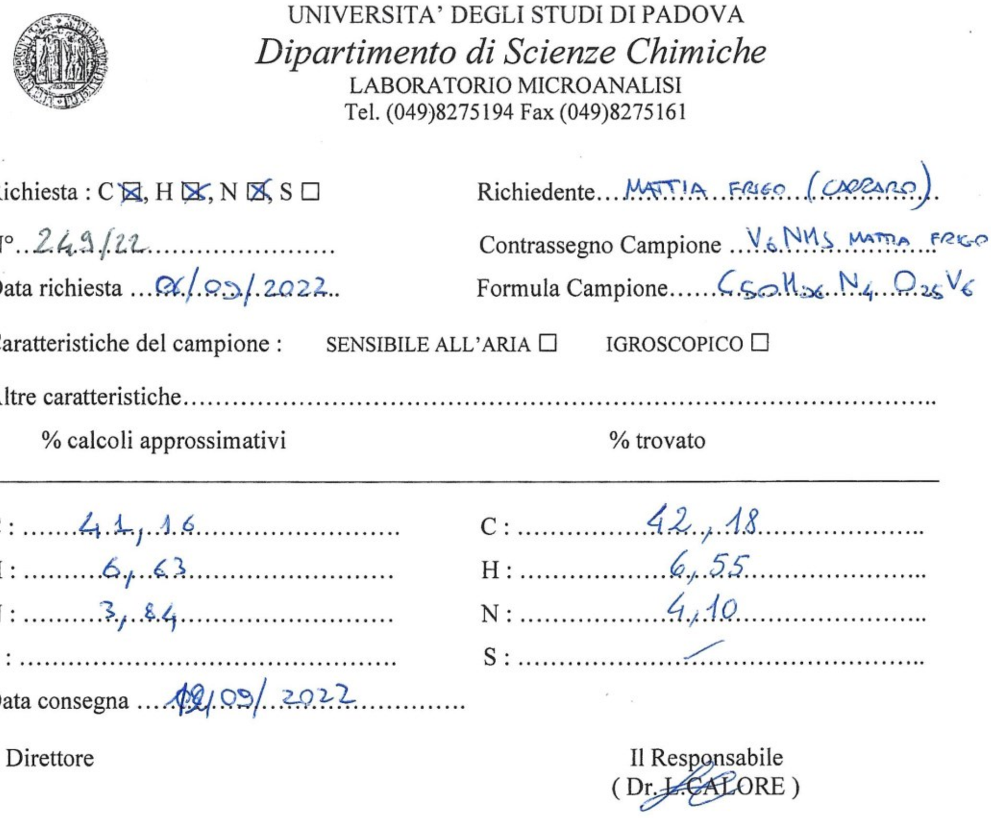

UNIVERSITA' DEGLI STUDI DI PADOVA

Dipartimento di Scienze Chimiche

LABORATORIO MICROANALISI

Tel. (049)8275194 Fax (049)8275161

Richiesta : C ☒, H ☒, N ☒, S ☐ Richiedente MATTIA FRIGO (CARRARO)

N° 249/22 Contrassegno Campione V_6NMS MATTIA FRIGO

Data richiesta 06/09/2022 Formula Campione $C_{50}H_{96}N_4O_{25}V_6$

Caratteristiche del campione : SENSIBILE ALL'ARIA ☐ IGROSCOPICO ☐

Altre caratteristiche…………………

% calcoli approssimativi	% trovato
C : 41,16	C : 42,18
H : 6,63	H : 6,55
N : 3,84	N : 4,10
S :	S : /

Data consegna 12/09/2022

Il Direttore

Il Responsabile

(Dr. L. CALORE)

SYNTHESIS 5B "V_6-O-Phe" -

$(C_4H_9)_4N]_2[V_6O_{13}\{(OCH_2)_3CCH_2OOCCH_2CH_2COPheOMe\}_2]$

ESI-MS (-):

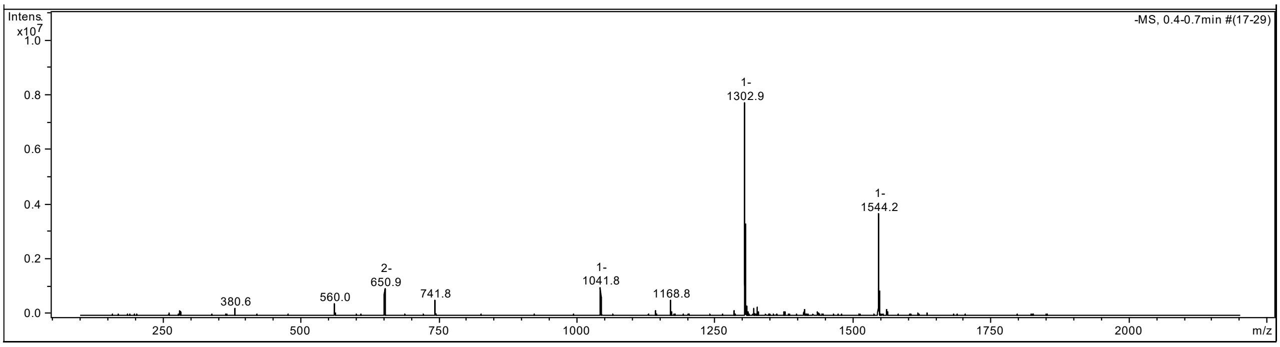

FT-IR:

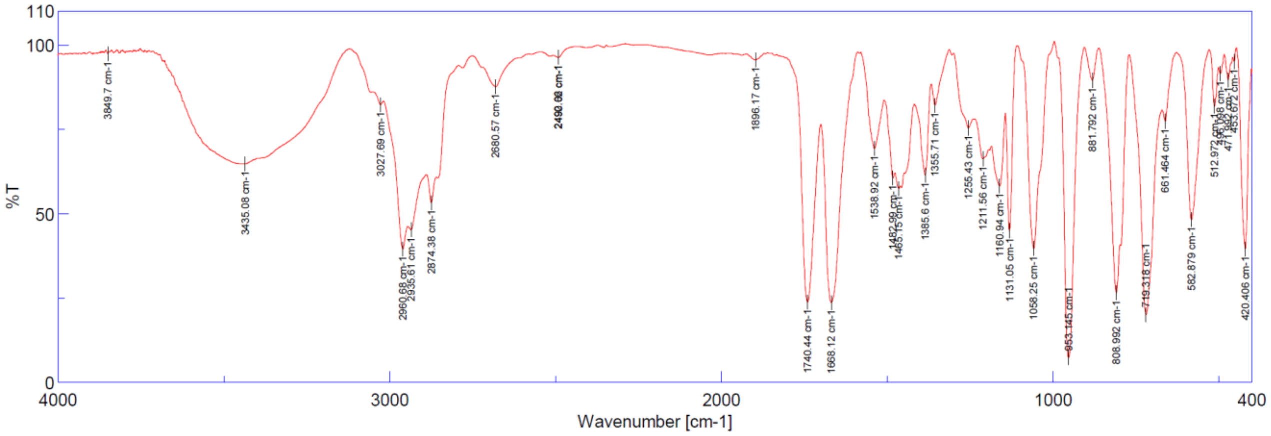

^{1}H NMR 300 (CD$_3$CN):

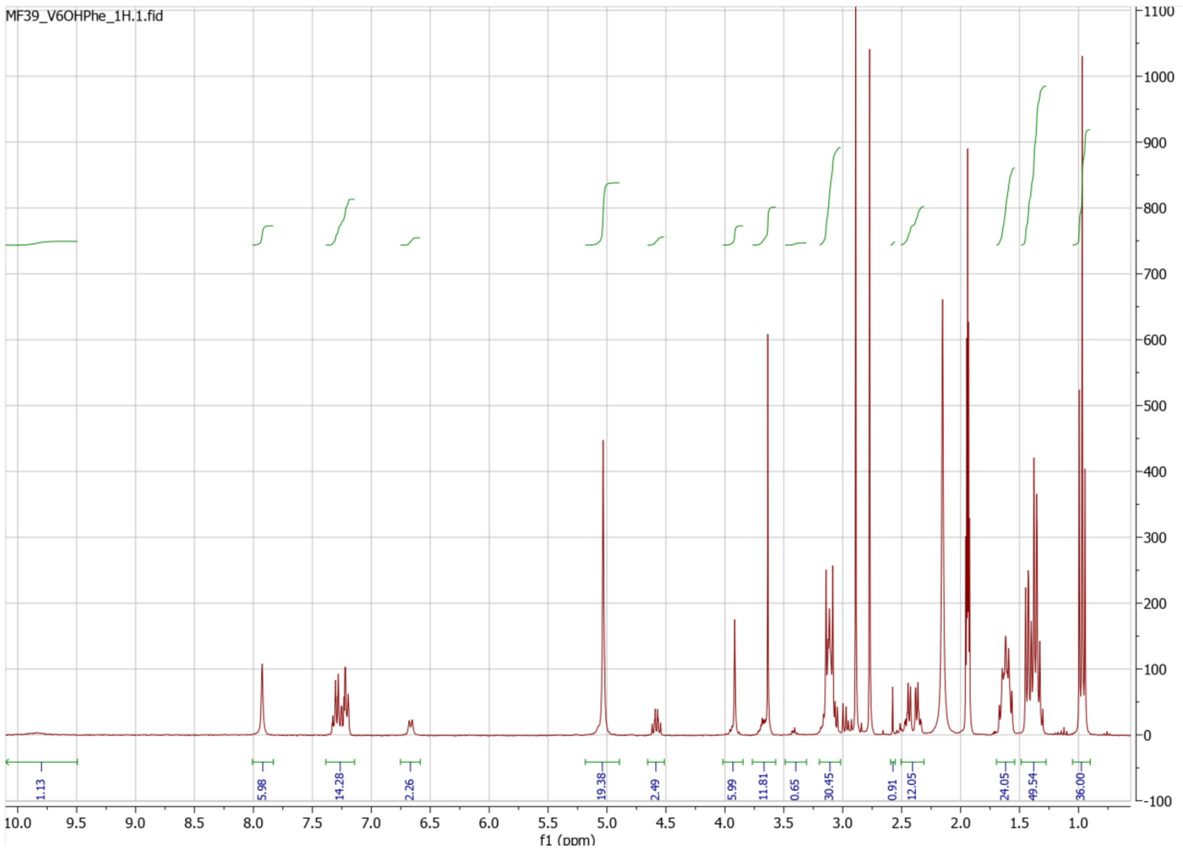

^{51}V NMR 300 (CD_3CN):

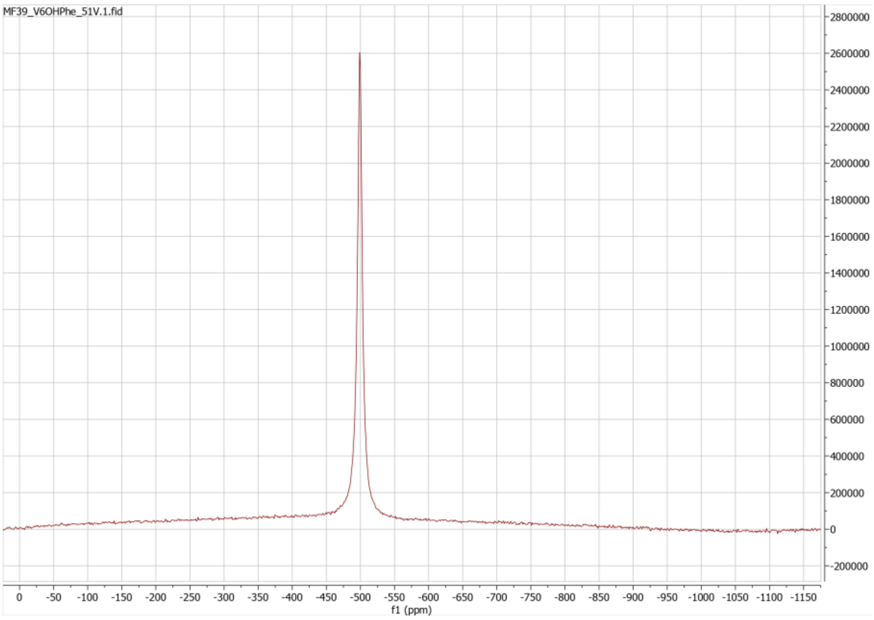

SYNTHESIS 6B:

Synthesis of “V_6-O-DB”

$[(C_4H_9)_4N]_2[V_6O_{13}\{(OCH_2)_3CCH_2OOCCH_2CH_2CO(C_{49}H_{68}N_{13}O_9)\}_2]$

ESI-MS (-):

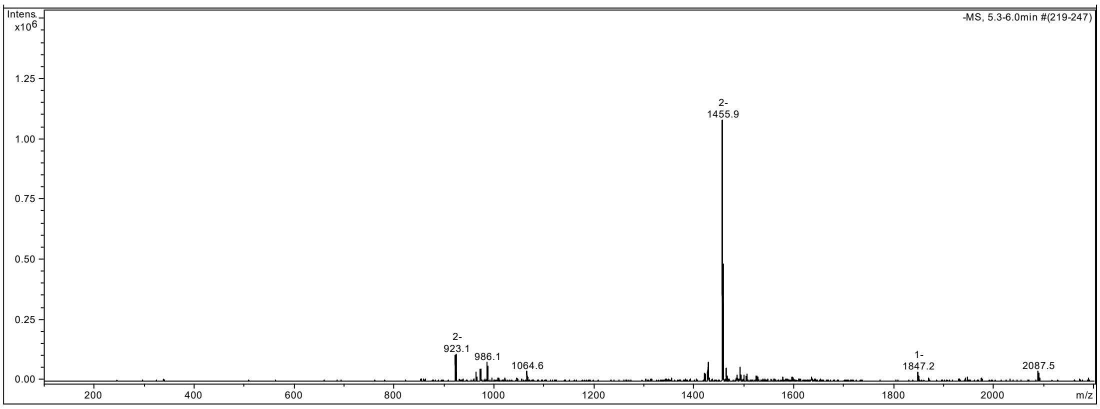

FT-IR(-):

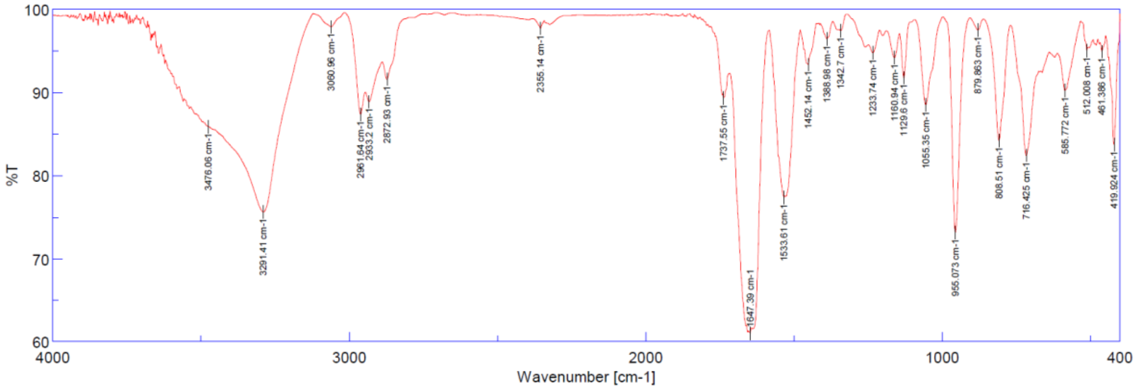

2D ^{1}H NMR (COSY):

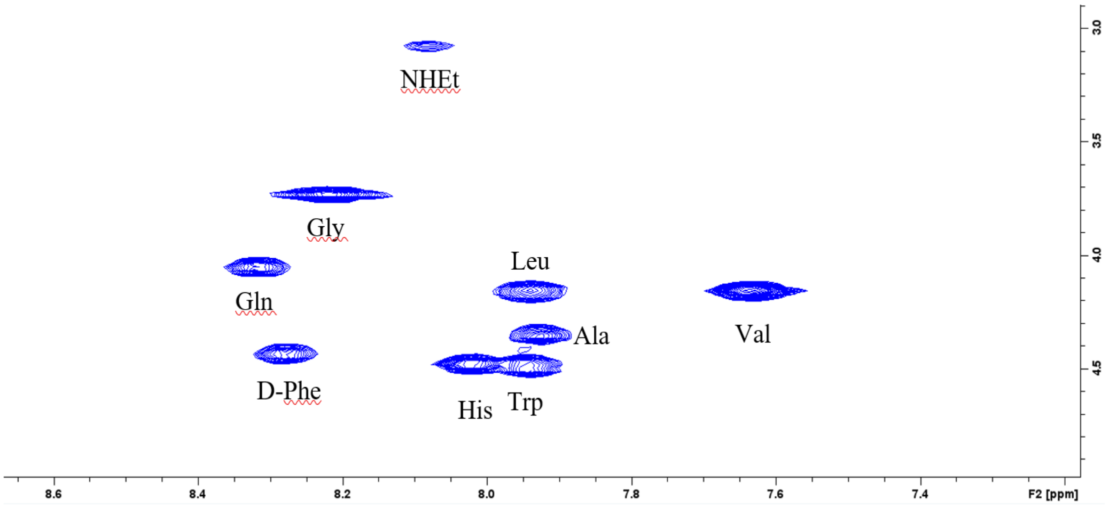

COSY of V_6-O-DB

2D ^{1}H NMR (TOCSY and ROESY)

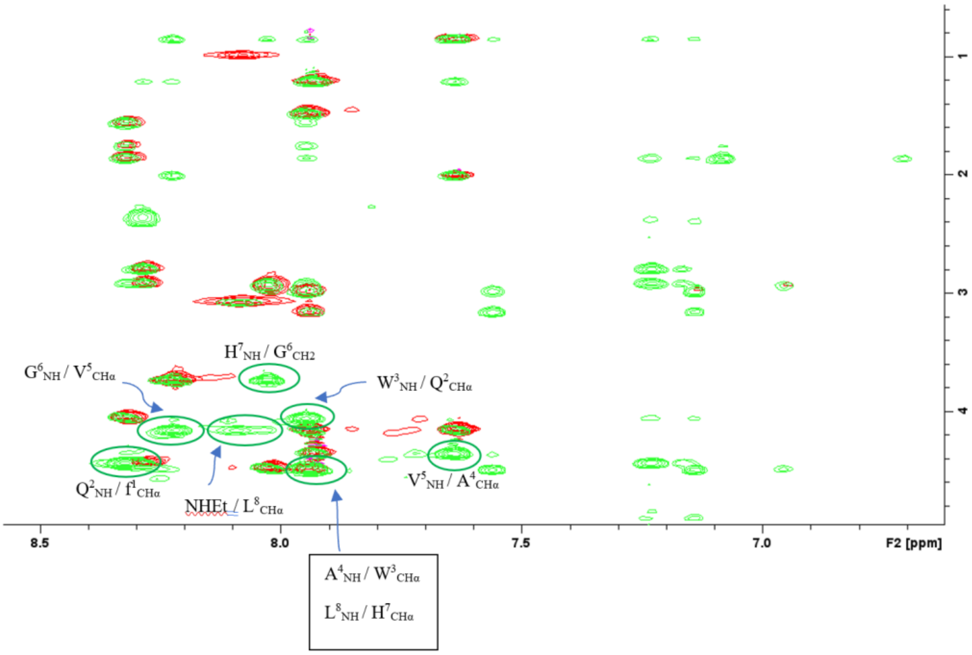

TOCSY and ROESY of V_6-O-DB

SYNTHESIS 7B:

Synthesis of "V_6-O - EEEEβAla-fQWAVGHL-NHEt"

$[(C_4H_9)_4N]_2[V_6O_{13}\{(OCH_2)_3CCH_2OOCCH_2CH_2CO(C_{72}H_{101}N_{18}O_{22})\}_2]$

ESI-MS (-):

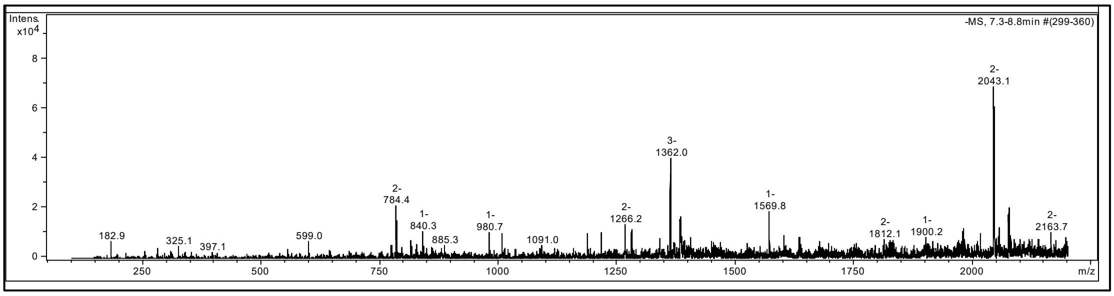

FT-IR:

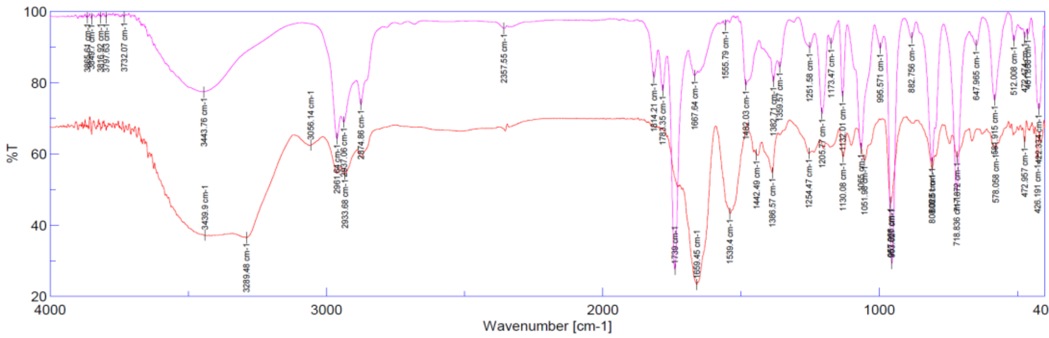

FT-IR spectrum of the reagent V_6-O-NHS (in purple) and the final coupling product V_6-O-EEEEβAlaDB (in red).

2D ^{1}H NMR COSY):

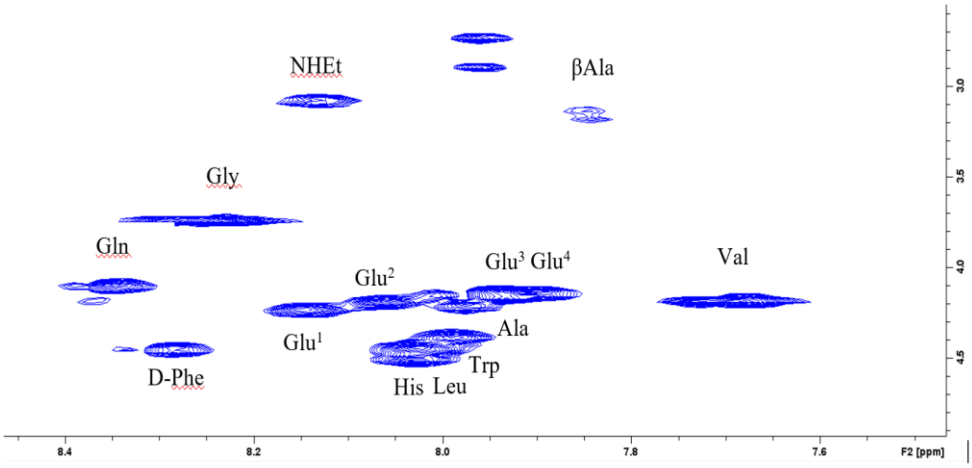

COSY signals for V_6-O-EEEEβAlaDB

2D ^{1}H NMR (TOCSY and ROESY):

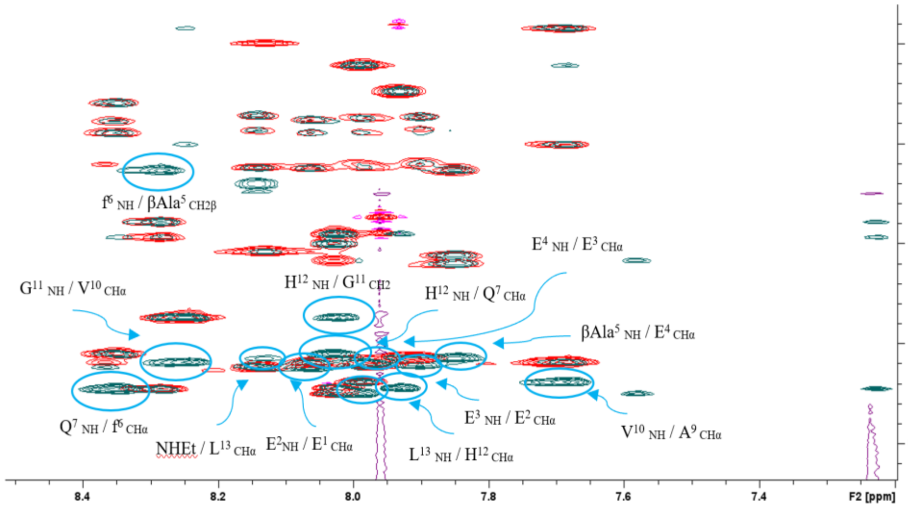

^{1}H ROESY of V_6-O-EEEEβAlaDB (in green) overlapped with TOCSY (in red). It is possible to notice the match between the amino acids His 12 and Gln 7.

SYNTHESIS 8B:

Synthesis of “V_6-O - TtdsDB”

$[(C_4H_9)_4N]_3[V_6O_{13}\{(OCH_2)_3CCH_2OOCCH_2CH_2CO(C_{49}H_{68}N_{13}O_9)\}_2]$

ESI-MS (-):

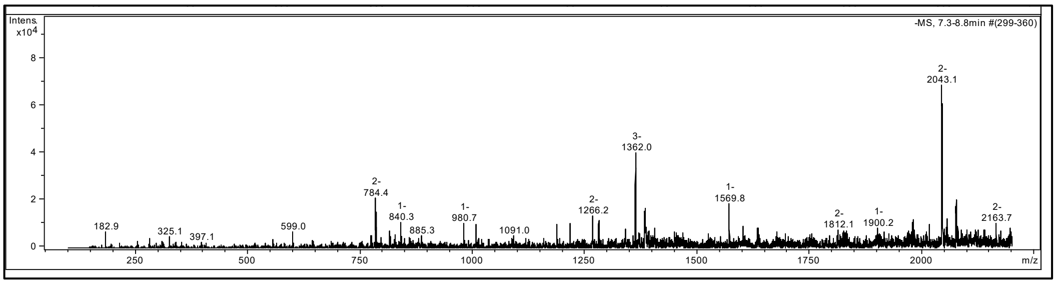

FT-IR:

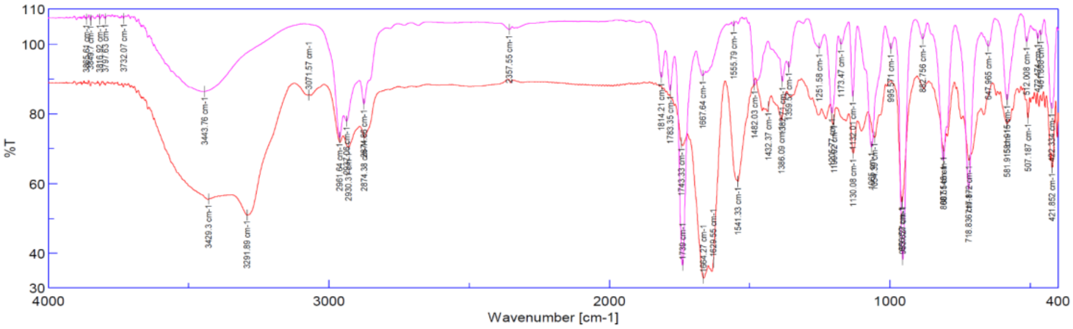

FT-IR spectrum of the reagent V_6-O-NHS (in purple) and the final coupling product V_6-O-TtdsDB (in red).

2D ^{1}H NMR (COSY):

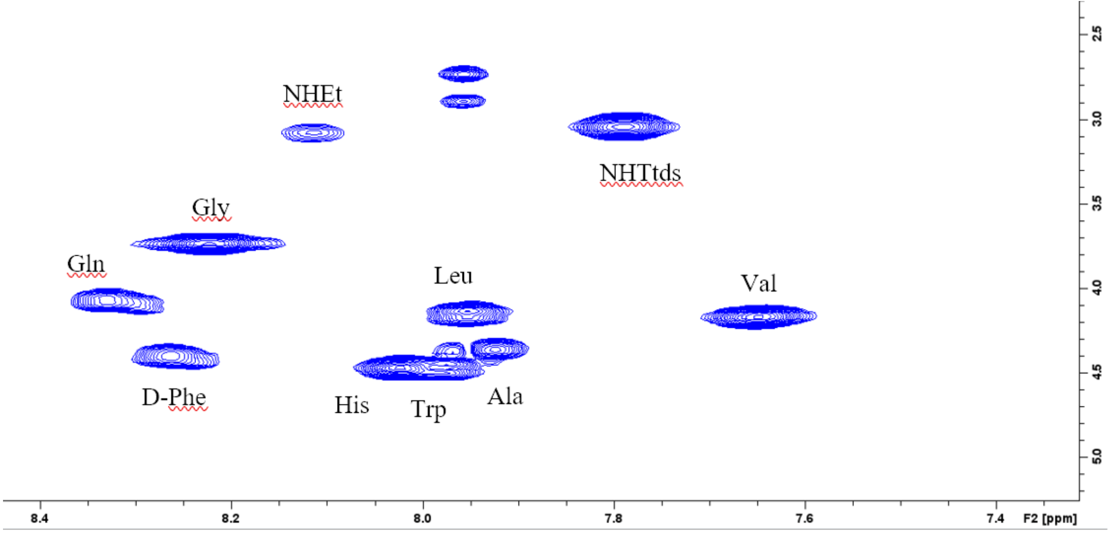

COSY of V_6-O-TtdsDB

2D ^{1}H NMR (TOCSY and ROESY):

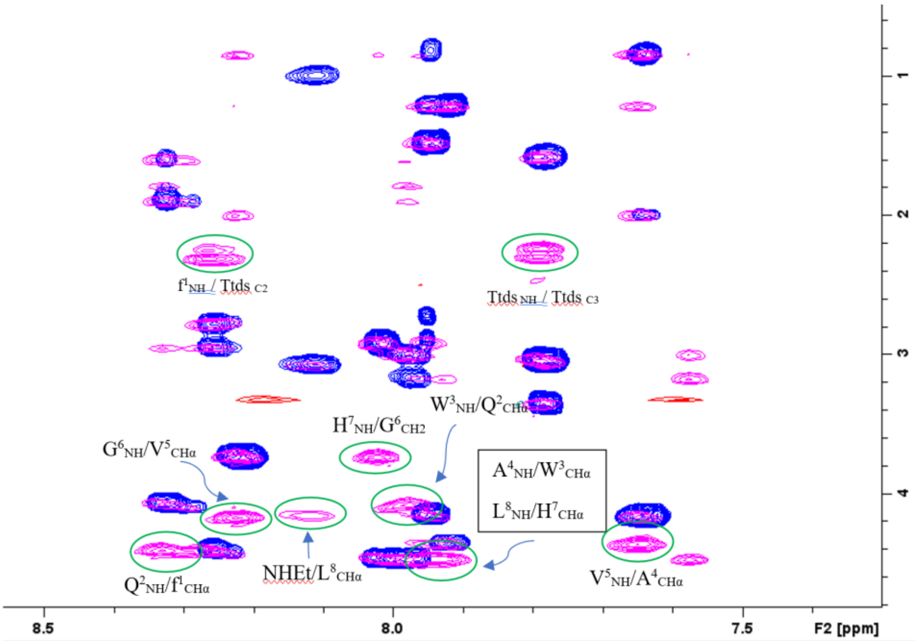

TOCSY and ROESY of V_6-O-TtdsDB

SYNTHESIS 9B:

Synthesis of "V_6-O-RGD"

$[(C_4H_9)_4N]_3[V_6O_{13}\{(OCH_2)_3CCH_2OOCCH_2CH_2CO(C_{27}H_{40}N_9O_7)\}_2]$

ESI-MS(-):

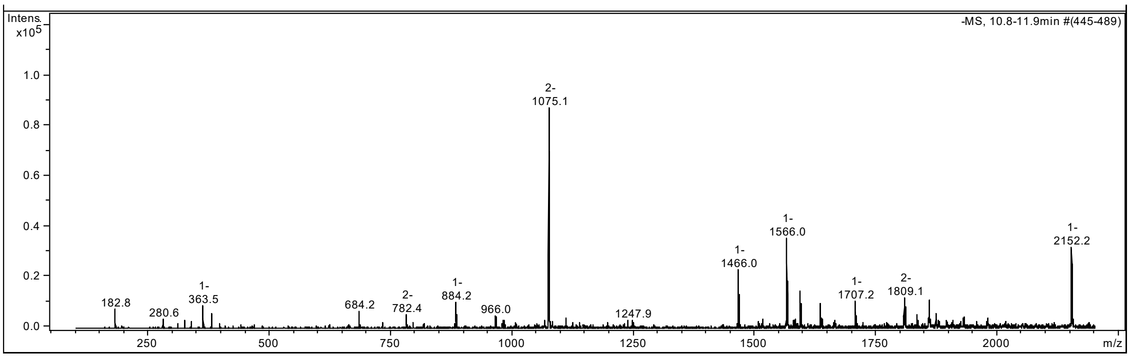

FT-IR:

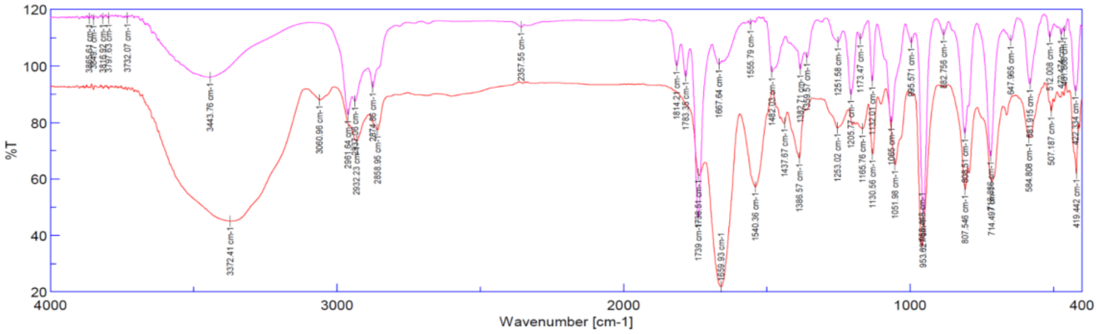

FT-IR spectrum of the reagent V_6-O-NHS (in purple) and the final coupling product V_6-O-c(RGDfK) (in red).

2D ^{1}H NMR (COSY):

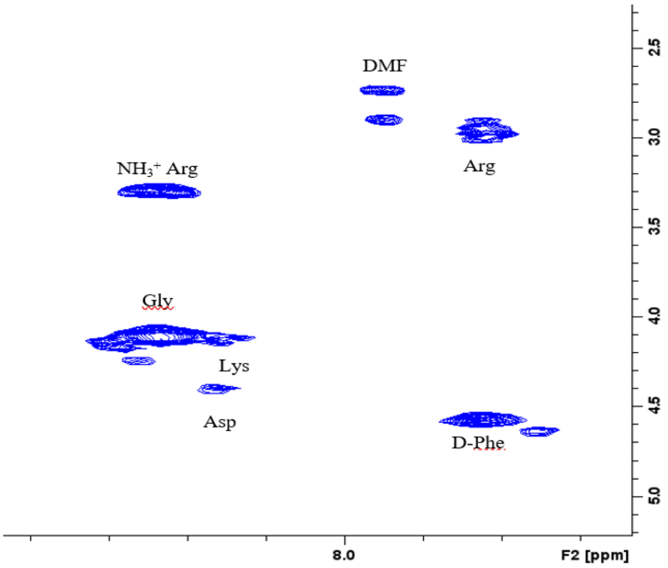

COSY of V_6O-c(RGDfK).

2D ^{1}H NMR (TOCSY and ROESY):

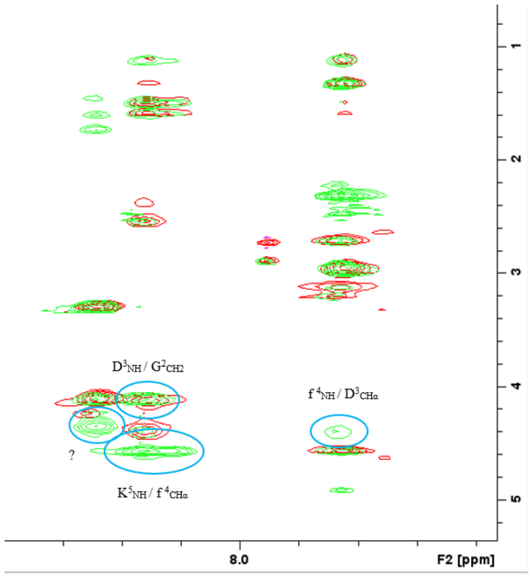

TOCSY and ROESY of V_6O-c(RGDfK)

^{51}V NMR OF ALL HYBRIDS

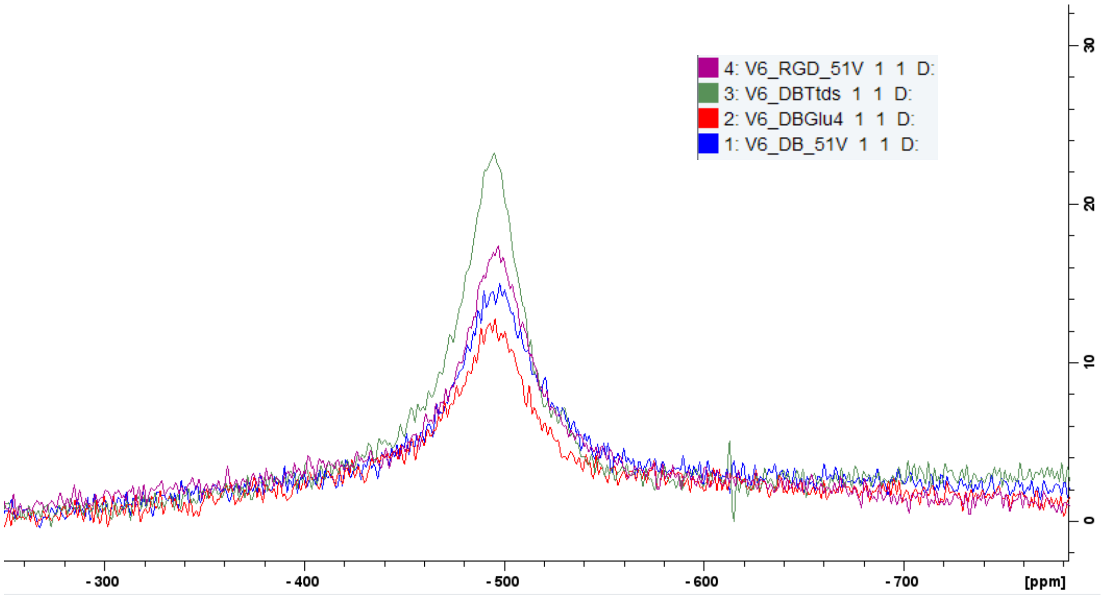

2D NMR of PEPTIDES

2D ^{1}H NMR (TOCSY and ROESY of Demobesin-1 alone):

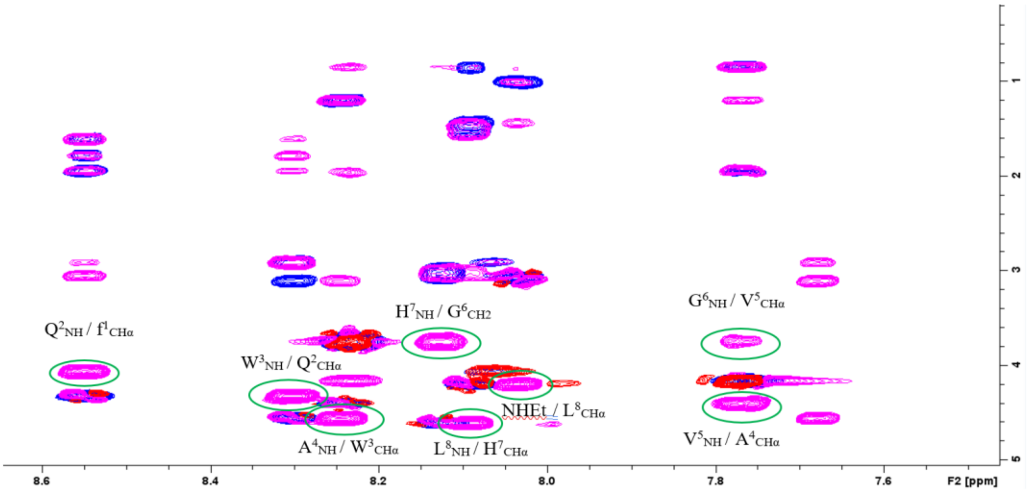

TCOSY and ROESY of Demobesin-1 (DB).

2D ^{1}H NMR (TOCSY and ROESY of DB-βAlaEEEE alone):

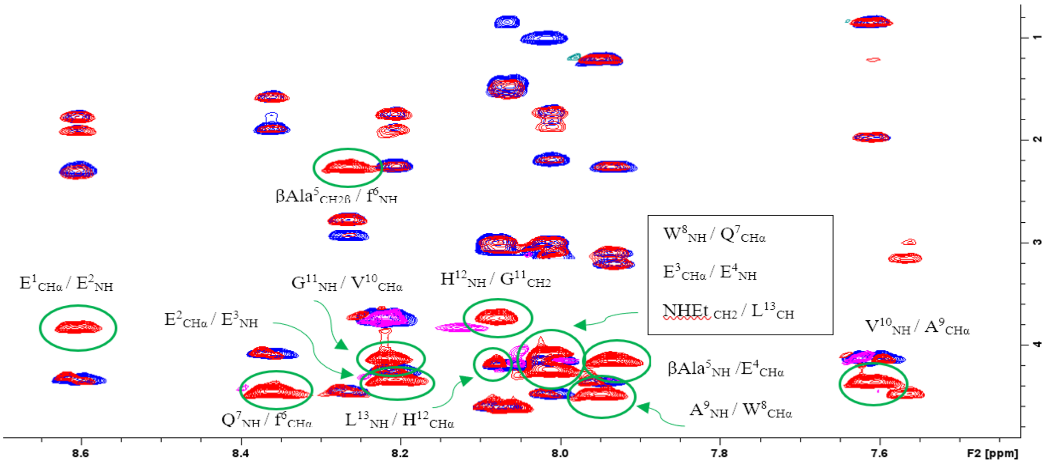

^{1}H ROESY of DB-βAlaEEEE (in red) overlapped with TOCSY (in blue)

2D ^{1}H NMR (TOCSY and ROESY of DB-Ttds alone):

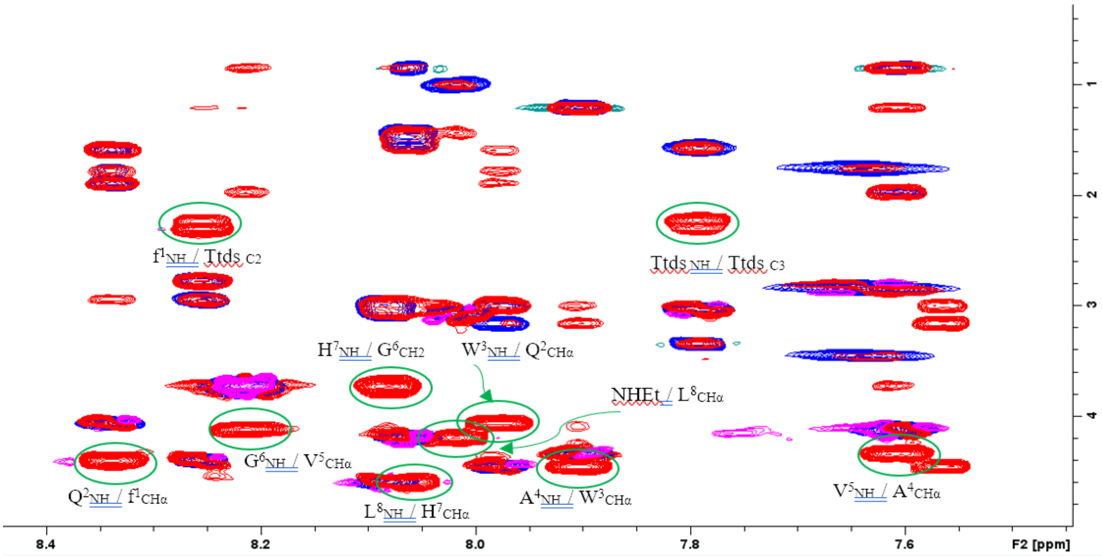

TOCSY and ROESY of DBTtds

2D ^{1}H NMR (TOCSY and ROESY of c(RGDfK)):

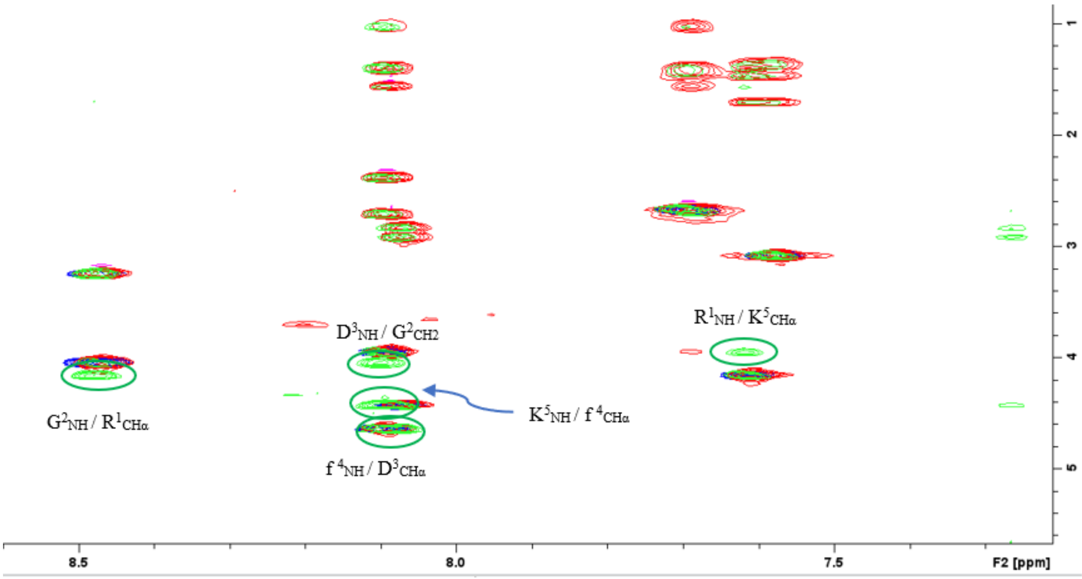

F TOCSY and ROESY of c(RGDfK) alone.

Bibliography

1. Pope MT, Sadakane M, Kortz U. Celebrating Polyoxometalate Chemistry. *Eur J Inorg Chem*. 2019;2019(3-4):340-342. doi:10.1002/EJIC.201801543
2. Berzelius JJ. Beitrag zur näheren Kenntniss des Molybdäns. *Ann Phys*. 1826;82(4):369-392. doi:10.1002/ANDP.18260820402
3. Keggin JF. Structure of the Molecule of 12-Phosphotungstic Acid. *Nature 1933 131:3321*. 1933;131(3321):908-909. doi:10.1038/131908b0
4. Thabet MS, Thabet MS. Anderson Heteropolymolybdates Cluster Loaded on Zeolite Materials: Preparation and Characterization. *Journal of Encapsulation and Adsorption Sciences*. 2019;9(1):1-12. doi:10.4236/JEAS.2019.91001
5. Rhule JT, Hill CL, Judd DA, Schinazi RF. Polyoxometalates in Medicine. Published online 1998. Accessed August 6, 2022. https://pubs.acs.org/sharingguidelines
6. Katsoulis DE. A survey of applications of polyoxometalates. *Chem Rev*. 1998;98(1):359-387. doi:10.1021/CR960398A/ASSET/IMAGES/MEDIUM/CR960398AE00006.GIF
7. Cadot E, Béreau V, Marg B, Halut S, Sécheresse F. Syntheses and characterization of γ-[SiW10M2S2O38]6- (M = Mov, Wv). Two Keggin oxothio heteropolyanions with a metal-metal bond. *Inorg Chem*. 1996;35(11):3099-3106. doi:10.1021/IC951054Q/SUPPL_FILE/IC3099.PDF
8. Bino A, Ardon M, Lee D, Spingler B, Lippard SJ. Synthesis and structure of [Fe13O4F24(OME)12]5-: The first open-shell Keggin ion. *J Am Chem Soc*. 2002;124(17):4578-4579. doi:10.1021/JA025590A/SUPPL_FILE/JA025590A_S1.PDF
9. Errington RJ; WRL; CW; E. Angew. Chem. Int. Ed. *2000, 39, 3884*.
10. Blazevic A, Rompel A. The Anderson–Evans polyoxometalate: From inorganic building blocks via hybrid organic–inorganic structures to tomorrows “Bio-POM.” *Coord Chem Rev*. 2016;307:42-64. doi:10.1016/J.CCR.2015.07.001

11. López X, Maestre JM, Bo C, Poblet JM. Electronic Properties of Polyoxometalates: A DFT Study of α/β-[XM12O40]n- Relative Stability (M = W, Mo and X a Main Group Element). *J Am Chem Soc*. 2001;123(39):9571-9576. doi:10.1021/JA010768Z

12. Azmani K, Besora M, Soriano-López J, et al. Understanding polyoxometalates as water oxidation catalysts through iron vs. cobalt reactivity. *Chem Sci*. 2021;12(25):8755-8766. doi:10.1039/D1SC01016F

13. Yamase T. Polyoxometalates for Molecular Devices: Antitumor Activity and Luminescence. Published online 1994:337-358. doi:10.1007/978-94-011-0920-8_25

14. Pope MT, Varga GM. Heteropoly Blues. I. Reduction Stoichiometries and Reduction Potentials of Some 12-Tungstates. *Inorg Chem*. 1966;5(7):1249-1254. doi:10.1021/IC50041A038/ASSET/IC50041A038.FP.PNG_V03

15. López X, Carbó JJ, Bo C, Poblet JM. Structure, properties and reactivity of polyoxometalates: A theoretical perspective. *Chem Soc Rev*. 2012;41(22):7537-7571. doi:10.1039/C2CS35168D

16. Katsoulis DE. A Survey of Applications of Polyoxometalates. Published online 1998.

17. Aureliano M, Gumerova NI, Sciortino G, Garribba E, Rompel A, Crans DC. Polyoxovanadates with emerging biomedical activities. *Coord Chem Rev*. 2021;447. doi:10.1016/J.CCR.2021.214143

18. Yamase T. Polyoxometalates active against tumors, viruses, and bacteria. *Prog Mol Subcell Biol*. 2013;54:65-116. doi:10.1007/978-3-642-41004-8_4/FIGURES/21

19. Wu L, Liang J. Polyoxometalates and their complexes toward biological application. *Supramolecular Chemistry of Biomimetic Systems*. Published online October 10, 2017:311-354. doi:10.1007/978-981-10-6059-5_13/COVER

20. Yamase T. Polyoxometalates active against tumors, viruses, and bacteria. *Prog Mol Subcell Biol*. 2013;54:65-116. doi:10.1007/978-3-642-41004-8_4/FIGURES/21

21. Shahabadi N, Mahdavi M, Zendehcheshm S. Can polyoxometalates (POMs) prevent of coronavirus 2019-nCoV cell entry? Interaction of POMs with TMPRSS2 and spike receptor domain complexed with ACE2 (ACE2-RBD): Virtual screening approaches. *Inform Med Unlocked*. 2022;29:100902. doi:10.1016/J.IMU.2022.100902

22. Kozhevnikov I v. Catalysis by heteropoly acids and multicomponent polyoxometalates in liquid-phase reactions. *Chem Rev*. 1998;98(1):171-198. doi:10.1021/CR960400Y/ASSET/IMAGES/LARGE/CR960400YF00010.JPEG

23. Misono M. Catalytic chemistry of solid polyoxometalates and their industrial applications. *Molecular Engineering 1993 3:1*. 1993;3(1):193-203. doi:10.1007/BF00999633

24. Minami N; HM; IK; UY. Japanese Patent JP 08113732, 08113731, 08141493. *A2, 1996; Chem Abstr 1996, 125*.

25. Heller A; AP; C. Process for metal deposition for microelectronic interconnections J. C. U.S. 1994.Patent 5292558.

26. Evans HT. The crystal structures of ammonium and potassium molybdotellurates. *J Am Chem Soc*. 1948;70(3):1291-1292. doi:10.1021/JA01183A521/ASSET/JA01183A521.FP.PNG_V03

27. An H, Liu X, Chen H, Han Z, Zhang H, Chen Z. Assembling Anderson-type polyoxometalates with manganese(II) in the presence of pyridylacrylic acid ligands: a 2D layer and two polymorphs. *CrystEngComm*. 2011;13(17):5384-5393. doi:10.1039/C1CE05391D

28. Blazevic A, Al-Sayed E, Roller A, Giester G, Rompel A. Tris-Functionalized Hybrid Anderson Polyoxometalates: Synthesis, Characterization, Hydrolytic Stability and Inversion of Protein Surface Charge. *Chemistry – A European Journal*. 2015;21(12):4762-4771. doi:10.1002/CHEM.201405644

29. Wang SM, Li YW, Feng XJ, Li YG, Wang EB. New synthetic route of polyoxometalate-based hybrids in choline chloride/urea eutectic media. *Inorganica Chim Acta*. 2010;363(7):1556-1560. doi:10.1016/J.ICA.2009.12.012

30. Thabet S, Ayed B, Haddad A. A novel organic–inorganic hybrid with Anderson type polyanions as building blocks: (C6H10N3O2)2Na(H2O)2[Al(OH)6Mo6O18]·6H2O. *Mater Res Bull*. 2012;47(11):3791-3796. doi:10.1016/J.MATERRESBULL.2012.06.018

31. Blazevic A, Rompel A. The Anderson–Evans polyoxometalate: From inorganic building blocks via hybrid organic–inorganic structures to tomorrows "Bio-POM." *Coord Chem Rev*. 2016;307:42-64. doi:10.1016/J.CCR.2015.07.001

32. Blazevic A, Al-Sayed E, Roller A, Giester G, Rompel A. Tris-functionalized hybrid Anderson polyoxometalates: Synthesis, characterization, hydrolytic stability and inversion of protein surface charge. *Chemistry - A European Journal*. 2015;21(12):4762-4771. doi:10.1002/CHEM.201405644

33. Batchelor LJ, Shaw R, Markey SJ, Helliwell M, McInnes EJL. An all-vanadiuni(III) hexametalate lindqvist structure and its chromium and iron analogues. *Chemistry - A European Journal*. 2010;16(19):5554-5557. doi:10.1002/CHEM.201000222

34. HayashiYoshihito, OzawaYoshiki, IsobeKiyoshi. The First "Vanadate Hexamer" Capped by Four Pentamethylcyclopentadienyl-rhodium or -iridium Groups. *http://dx.doi.org/101246/cl1989425*. 2006;18(3):425-428. doi:10.1246/CL.1989.425

35. Anyushin A v., Kondinski A, Parac-Vogt TN. Hybrid polyoxometalates as post-functionalization platforms: from fundamentals to emerging applications. *Chem Soc Rev*. 2020;49(2):382-432. doi:10.1039/C8CS00854J

36. Spillane S, Sharma R, Zavras A, et al. Non-Aqueous Microwave-Assisted Syntheses of Deca- and Hexa-Molybdovanadates. *Angewandte Chemie International Edition*. 2017;56(29):8568-8572. doi:10.1002/ANIE.201608589

37. Nachtigall O, Spandl J. Versatile Organic Chemistry on Vanadium-Based Multi-Electron Reservoirs. *Chemistry – A European Journal*. 2018;24(11):2785-2789. doi:10.1002/CHEM.201800041

38. Nachtigall O, Spandl J. Versatile Organic Chemistry on Vanadium-Based Multi-Electron Reservoirs. *Chemistry – A European Journal*. 2018;24(11):2785-2789. doi:10.1002/CHEM.201800041

39. DANA N, RAFIEI L, ROSTAMI M, HOSSEINI MS, JAVANMARD SH, HARİRİ AA. Anti-Cancer Activity of Biotin-Polyoxomolybdate Bioconjugate. *Eurasian J Med Oncol*. 2020;4(1):42-48. doi:10.14744/EJMO.2020.34747

40. Hong Rim C. Development of quantitative index evaluating anticancer or carcinogenic potential of diet: the anti-cancer food scoring system 1.0. doi:10.4162/nrp.2018.12.1.52

41. Kocarnik JM, Compton K, Dean FE, et al. Cancer Incidence, Mortality, Years of Life Lost, Years Lived With Disability, and Disability-Adjusted Life Years for 29 Cancer Groups From 2010 to 2019: A Systematic Analysis for the Global Burden of Disease Study 2019. *JAMA Oncol*. 2022;8(3):420-444. doi:10.1001/JAMAONCOL.2021.6987

42. IARC Publications Website - World Cancer Report 2014. Accessed August 9, 2022. https://publications.iarc.fr/Non-Series-Publications/World-Cancer-Reports/World-Cancer-Report-2014

43. Croce CM. Oncogenes and Cancer. *https://doi.org/101056/NEJMra072367*. 2008;358(5):502-511. doi:10.1056/NEJMRA072367

44. Knudson AG. Two genetic hits (more or less) to cancer. *Nature Reviews Cancer 2001 1:2*. 2001;1(2):157-162. doi:10.1038/35101031

45. Johnstone RW, Ruefli AA, Lowe SW. Apoptosis: A Link between Cancer Genetics and Chemotherapy. *Cell*. 2002;108(2):153-164. doi:10.1016/S0092-8674(02)00625-6

46. Rampling R, James A, Papanastassiou V. The present and future management of malignant brain tumours: surgery, radiotherapy, chemotherapy. *J Neurol Neurosurg Psychiatry*. 2004;75(suppl 2):ii24-ii30. doi:10.1136/JNNP.2004.040535

47. Pooja D, Gunukula A, Gupta N, Adams DJ, Kulhari H. Bombesin receptors as potential targets for anticancer drug delivery and imaging. *International Journal of Biochemistry and Cell Biology*. 2019;114. doi:10.1016/J.BIOCEL.2019.105567

48. Hansel TT, Kropshofer H, Singer T, Mitchell JA, George AJT. The safety and side effects of monoclonal antibodies. *Nature Reviews Drug Discovery 2010 9:4*. 2010;9(4):325-338. doi:10.1038/nrd3003

49. Kumar RJ, Barqawi A, Crawford ED. Adverse Events Associated with Hormonal Therapy for Prostate Cancer. *Rev Urol*. 2005;7(Suppl 5):S37. Accessed August 18, 2022. /pmc/articles/PMC1477613/

50. Hu X, Wang H, Huang B, et al. A new scheme for rational design and synthesis of polyoxovanadate hybrids with high antitumor activities. *J Inorg Biochem*. 2019;193:130-132. doi:10.1016/J.JINORGBIO.2019.01.013

51. Ogata A, Mitsui S, Yanagie H, et al. A novel anti-tumor agent, polyoxomolybdate induces apoptotic cell death in AsPC-1 human pancreatic cancer cells. *Biomedicine & Pharmacotherapy*. 2005;59(5):240-244. doi:10.1016/J.BIOPHA.2004.11.008

52. Mitsui S, Ogata A, Yanagie H, et al. Antitumor activity of polyoxomolybdate, [NH3Pri]6[Mo7O24] ·3H2O, against, human gastric cancer model. *Biomedicine and Pharmacotherapy*. 2006;60(7):353-358. doi:10.1016/J.BIOPHA.2006.02.009

53. Liu Y, Tian S, Liu S, Wang E. In vitro inhibitory effect of polyoxometalates on human tumor cells. *Transition Metal Chemistry 2005 30:1*. 2005;30(1):113-117. doi:10.1007/S11243-004-3825-1

54. Aloj L, Morelli G. Design, synthesis and preclinical evaluation of radiolabeled peptides for diagnosis and therapy. *Curr Pharm Des*. 2004;10(24):3009-3031. doi:10.2174/1381612043383511

55. Miras HN, Yan J, Long DL, Cronin L. Engineering polyoxometalates with emergent properties. *Chem Soc Rev*. 2012;41(22):7403-7430. doi:10.1039/C2CS35190K

56. Simons TJ. Vanadate — a new tool for biologists. *Nature 1979 281:5730*. 1979;281(5730):337-338. doi:10.1038/281337a0

57. D'Cruz OJ, Dong Y, Uckun FM. Potent dual anti-HIV and spermicidal activities of novel oxovanadium(V) complexes with thiourea non-nucleoside

inhibitors of HIV-1 reverse transcriptase. *Biochem Biophys Res Commun*. 2003;302(2):253-264. doi:10.1016/S0006-291X(03)00161-X

58. Heinemann G, Fichtl B, Vogt W. Pharmacokinetics of vanadium in humans after intravenous administration of a vanadium containing albumin solution. *Br J Clin Pharmacol*. 2003;55(3):241. doi:10.1046/J.1365-2125.2003.01711.X

59. Kanna PS, Mahendrakumar CB, Indira BN, et al. Chemopreventive effects of vanadium toward 1,2-dimethylhydrazine-induced genotoxicity and preneoplastic lesions in rat colon. *Environ Mol Mutagen*. 2004;44(2):113-118. doi:10.1002/EM.20038

60. Aureliano M, Gândara RMC. Decavanadate effects in biological systems. *J Inorg Biochem*. 2005;99(5):979-985. doi:10.1016/J.JINORGBIO.2005.02.024

61. Krstić D, Čolović M, Bošnjaković-Pavlović N, Spasojević-De Bire A. Influence of decavanadate on rat synaptic plasma membrane ATPases activity-Na + /K +-ATPase-Plasma membrane Ca 2+-ATPase-ecto-ATPase. *Gen Physiol Biophys*. 2009;28:302-308. doi:10.4149/gpb_2009_03_302

62. Louati M, Ksiksi R, Elbini-Dhouib I, et al. Synthesis, structure and characterization of a novel decavanadate, Mg(H2O)6(C4N2H7)4V10O28·4H2O, with a potential antitumor activity. *J Mol Struct*. 2021;1242. doi:10.1016/J.MOLSTRUC.2021.130711

63. Xu X, Bošnjaković-Pavlović N, Čolović MB, et al. A combined crystallographic analysis and ab initio calculations to interpret the reactivity of functionalized hexavanadates and their inhibitor potency toward Na+/K+-ATPase. *J Inorg Biochem*. 2016;161:27-36. doi:10.1016/J.JINORGBIO.2016.04.029

64. Krstić D, Čolović M, Bošnjaković-Pavlović N, Bire AS de, Vasić V. Influence of decavanadate on rat synaptic plasma membrane ATPases activity. *Gen Physiol Biophys*. 2009;28(3):302-308. doi:10.4149/GPB_2009_03_302

65. Wang Y, Wang F, Wang D, et al. Synthesis and structure studies of a new hexavanadate-glycine hybrid with high antitumor activities. *J Mol Struct*. 2020;1201:127138. doi:10.1016/J.MOLSTRUC.2019.127138

66. Tomita K, Yamase T, Shishido K. Medical chemistry of polyoxometalates. Part 2. Enzymatic study on binding of heptamolybdate to DNA. *Inorganica Chim Acta*. 1989;157(2):167-169. doi:10.1016/S0020-1693(00)80537-X

67. Yanagie H, Ogata A, Mitsui S, Hisa T, Yamase T, Eriguchi M. Anticancer activity of polyoxomolybdate. *Biomedicine & Pharmacotherapy*. 2006;60(7):349-352. doi:10.1016/J.BIOPHA.2006.06.018

68. Yamase T. Anti-tumor, -viral, and -bacterial activities of polyoxometalates for realizing an inorganic drug. *J Mater Chem*. 2005;15(45):4773-4782. doi:10.1039/B504585A

69. Folkman J. Clinical Applications of Research on Angiogenesis. *https://doi.org/101056/NEJM199512283332608*. 1995;333(26):1757-1763. doi:10.1056/NEJM199512283332608

70. Zheng W, Yang L, Liu Y, et al. Science and Technology of Advanced Materials Mo polyoxometalate nanoparticles inhibit tumor growth and vascular endothelial growth factor induced angiogenesis Mo polyoxometalate nanoparticles inhibit tumor growth and vascular endothelial growth factor induced angiogenesis. Published online 2014. doi:10.1088/1468-6996/15/3/035010

71. Hosseini MS, Javanmard SH, Raei L, Rostami M. Novel Tocopherol Succinate-Polyoxomolybdate Bioconjugate as Potential Anti-Cancer Agent. Published online 2021. doi:10.21203/rs.3.rs-214396/v1

72. Yang HK, Cheng YX, Su MM, et al. Polyoxometalate–biomolecule conjugates: A new approach to create hybrid drugs for cancer therapeutics. *Bioorg Med Chem Lett*. 2013;23(5):1462-1466. doi:10.1016/J.BMCL.2012.12.081

73. Hosseini MS, Javanmard SH, Raei L, Rostami M. Novel Tocopherol Succinate-Polyoxomolybdate Bioconjugate as Potential Anti-Cancer Agent. Published online 2021. doi:10.21203/rs.3.rs-214396/v1

74. Ventura D, Calderan A, Honisch C, et al. Synthesis and biological activity of an Anderson polyoxometalate bis-functionalized with a Bombesin-analog peptide. *Peptide Science*. 2018;110(5):e24047. doi:10.1002/PEP2.24047

75. Marilyn H. Perrin SWS, Journal of Pharmacology and Experimental Therapeutics F 1999 288 (2) 729 734; Comparison of an Agonist, Urocortin, and an Antagonist, Astressin, as Radioligands for Characterization of Corticotropin-Releasing Factor Receptors | Journal of Pharmacology and Experimental Therapeutics. Accessed August 9, 2022. https://jpet.aspetjournals.org/content/288/2/729

76. Hosseini MS. Anticancer Activity of Biotin Polyoxomolybdate Bioconjugate. *Eurasian J Med Oncol*. Published online 2020. doi:10.14744/EJMO.2020.34747

77. Depeint F, Bruce WR, Shangari N, Mehta R, O'Brien PJ. Mitochondrial function and toxicity: Role of the B vitamin family on mitochondrial energy metabolism. *Chem Biol Interact*. 2006;163(1-2):94-112. doi:10.1016/J.CBI.2006.04.014

78. Hu W, Fang L, Hua W, Gou S. Biotin-Pt (IV)-indomethacin hybrid: A targeting anticancer prodrug providing enhanced cancer cellular uptake and reversing cisplatin resistance. *J Inorg Biochem*. 2017;175:47-57. doi:10.1016/J.JINORGBIO.2017.07.002

79. Plazìuk D, Zakrzewski J, Salmain M, et al. Ferrocene-biotin conjugates targeting cancer cells: Synthesis, interaction with avidin, cytotoxic properties and the crystal structure of the complex of avidin with a biotin-linker-ferrocene conjugate. *Organometallics*. 2013;32(20):5774-5783. doi:10.1021/OM4003126/SUPPL_FILE/OM4003126_SI_001.PDF

80. Ruzza P, Marchiani A, Antolini N, Calderan A. Peptide-Receptor Ligands and Multivalent Approach. *Anticancer Agents Med Chem*. 2012;12(5):416-427. doi:10.2174/187152012800617849

81. Reubi JC, Gugger M, Waser B. Co-expressed peptide receptors in breast cancer as a molecular basis for in vivo multireceptor tumour targeting. *Eur J Nucl Med Mol Imaging*. 2002;29(7):855-862. doi:10.1007/S00259-002-0794-5

82. Akizawa H, Arano Y, Uezono T, et al. Renal metabolism of 111In-DTPA-D-Phe1-octreotide in vivo. *Bioconjug Chem*. 1998;9(6):662-670. doi:10.1021/BC9702258

83. GRP gastrin releasing peptide [Homo sapiens (human)] - Gene - NCBI. Accessed August 10, 2022. https://www.ncbi.nlm.nih.gov/gene?Db=gene&Cmd=ShowDetailView&TermToSearch=2922

84. Li F, Jiang H, Shen X, et al. Sneezing reflex is mediated by a peptidergic pathway from nose to brainstem. *Cell*. 2021;184(14):3762. doi:10.1016/J.CELL.2021.05.017

85. Reubi JC, Waser B. Concomitant expression of several peptide receptors in neuroendocrine tumours: molecular basis for in vivo multireceptor tumour targeting. *Eur J Nucl Med Mol Imaging*. 2003;30(5):781-793. doi:10.1007/S00259-003-1184-3

86. Pooja D, Gunukula A, Gupta N, Adams DJ, Kulhari H. Bombesin receptors as potential targets for anticancer drug delivery and imaging. *Int J Biochem Cell Biol*. 2019;114:105567. doi:10.1016/J.BIOCEL.2019.105567

87. Varasteh Z. Digital Comprehensive Summaries of Uppsala Dissertations from the Faculty of Pharmacy 191 Bombesin Antagonists for Targeting Gastrin-Releasing Peptide Receptor-Positive Tumors Design, Synthesis, Preclinical Evaluation and Optimization of Imaging Agents. Published online 2014. Accessed August 19, 2022. http://urn.kb.se/resolve?urn=urn:nbn:se:uu:diva-232123

88. Nock B, Nikolopoulou A, Chiotellis E, et al. [99mTc]Demobesin 1, a novel potent bombesin analogue for GRP receptor-targeted tumour imaging. *European Journal of Nuclear Medicine and Molecular Imaging 2003 30:2*. 2003;30(2):247-258. doi:10.1007/S00259-002-1040-X

89. Ferreira C de A, Fuscaldi LL, Townsend DM, Rubello D, Barros ALB de. Radiolabeled bombesin derivatives for preclinical oncological imaging. *Biomed Pharmacother*. 2017;87:58. doi:10.1016/J.BIOPHA.2016.12.083

90. Plow EF, Haas TA, Zhang L, Loftus J, Smith JW. Ligand Binding to Integrins *. *Journal of Biological Chemistry*. 2000;275(29):21785-21788. doi:10.1074/JBC.R000003200

91. Wang F, Li Y, Shen Y, Wang A, Wang S, Xie T. The Functions and Applications of RGD in Tumor Therapy and Tissue Engineering. *Int J Mol Sci*. 2013;14(7):13447. doi:10.3390/IJMS140713447

92. Bellis SL. Advantages of RGD peptides for directing cell association with biomaterials. *Biomaterials*. 2011;32(18):4205. doi:10.1016/J.BIOMATERIALS.2011.02.029

93. Aureliano M, Gumerova NI, Sciortino G, Garribba E, Rompel A, Crans DC. Polyoxovanadates with emerging biomedical activities. *Coord Chem Rev*. 2021;447. doi:10.1016/J.CCR.2021.214143

94. Guedes G, Wang S, Santos HA, Sousa FL. Polyoxometalate Composites in Cancer Therapy and Diagnostics. *Eur J Inorg Chem*. 2020;2020(22):2121-2132. doi:10.1002/EJIC.202000066

95. Ventura D, Calderan A, Honisch C, et al. Synthesis and biological activity of an Anderson polyoxometalate bis-functionalized with a Bombesin-analog peptide. *Peptide Science*. 2018;110(5). doi:10.1002/PEP2.24047

96. Lin CG, Hutin M, Busche C, Bell NL, Long DL, Cronin L. Elucidating the paramagnetic interactions of an inorganic–organic hybrid radical-functionalized Mn-Anderson cluster. *Dalton Transactions*. 2021;50(7):2350-2353. doi:10.1039/D0DT04149A

97. Vanhaecht S, Jacobs J, van Meervelt L, Parac-Vogt TN. A versatile and highly efficient post-functionalization method for grafting organic molecules onto Anderson-type polyoxometalates. *Dalton Transactions*. 2015;44(44):19059-19062. doi:10.1039/C5DT03559G

98. Nock BA, Charalambidis D, Sallegger W, et al. New Gastrin Releasing Peptide Receptor-Directed [99mTc]Demobesin 1 Mimics: Synthesis and Comparative Evaluation. *J Med Chem*. 2018;61(7):3138-3150. doi:10.1021/ACS.JMEDCHEM.8B00177

99. Cescato R, Maina T, Nock B, et al. Bombesin Receptor Antagonists May Be Preferable to Agonists for Tumor Targeting. *J Nucl Med*. 2008;49:318-326. doi:10.2967/jnumed.107.045054

100. Gugger M, Reubi JC. Gastrin-Releasing Peptide Receptors in Non-Neoplastic and Neoplastic Human Breast. *Am J Pathol*. 1999;155(6):2067. doi:10.1016/S0002-9440(10)65525-3

101. Mondal S, Biswas B, Nandy T, Singh PC. Understanding the Role of Hydrophobic Terminal in the Hydrogen Bond Network of the Aqueous Mixture of 2,2,2-Trifluoroethanol: IR, Molecular Dynamics, Quantum Chemical as Well as Atoms in Molecules Studies. *J Phys Chem B*. 2018;122(25):6616-6626. doi:10.1021/ACS.JPCB.8B04365

102. Li N, Qiu S, Fang Y, Wu J, Li Q. Comparison of Linear vs. Cyclic RGD Pentapeptide Interactions with Integrin αvβ3 by Molecular Dynamics Simulations. *Biology (Basel)*. 2021;10(7). doi:10.3390/BIOLOGY10070688

103. Stan CS, Albu C, Coroaba A, Popa M, Sutiman D. One step synthesis of fluorescent carbon dots through pyrolysis of N -hydroxysuccinimide. *J Mater Chem C Mater*. 2015;3(4):789-795. doi:10.1039/C4TC02382J